

Oxidatively Damaged RNA

Investigating the Impact of Oxidative Stress on a Molecular Level

Dissertation

zur Erlangung des Grades
»Doktor der Naturwissenschaften«
im Promotionsfach Pharmazie

am Fachbereich Chemie, Pharmazie, Geographie und Geowissenschaften
der Johannes Gutenberg-Universität Mainz

Marlies Weber

geboren in Mainz

Mainz, Juni 2024

JOHANNES GUTENBERG
UNIVERSITÄT MAINZ



Dekanin:

[REDACTED]

1. Gutachter:

[REDACTED]

2. Gutachter:

[REDACTED]

Tag der mündlichen Prüfung:

17.07.2024

D77 (Dissertation Mainz)

Die vorliegende Arbeit wurde am Institut für Pharmazeutische und Biomedizinische Wissenschaften der Johannes Gutenberg-Universität in Mainz zur Erlangung des Grades »Doktor der Naturwissenschaften« unter der Betreuung von [REDACTED] angefertigt.

1. Gutachter

[REDACTED]

Fachbereich Chemie, Pharmazie, Geographie und Geowissenschaften
Institut für Pharmazeutische und Biomedizinische Wissenschaften
Johannes Gutenberg-Universität Mainz

2. Gutachterin

[REDACTED]

Fachbereich Chemie, Pharmazie, Geographie und Geowissenschaften
Institut für Pharmazeutische und Biomedizinische Wissenschaften
Johannes Gutenberg-Universität Mainz

Hiermit versichere ich eidesstattlich:

1. Ich habe die jetzt als Dissertation vorgelegte Arbeit selbst angefertigt und alle benutzten Hilfsmittel (Literatur, Apparaturen, Material) in der Arbeit angegeben.
2. Ich habe oder hatte die jetzt als Dissertation vorgelegte Arbeit nicht als Prüfungsarbeit für eine staatliche oder andere wissenschaftliche Prüfung eingereicht.
3. Ich hatte weder die jetzt als Dissertation vorgelegte Arbeit noch Teile davon bei einer anderen Fakultät bzw. einem anderen Fachbereich als Dissertation eingereicht.

Ort, Datum

Unterschrift

DANKSAGUNG

CONTENTS

DANKSAGUNG	V
CONTENTS	VII
1 ABSTRACT	XI
2 AUSZUG	XIII
3 ABBREVIATIONS	XV
4 LIST OF FIGURES	XXI
5 LIST OF TABLES	XXIII
6 INTRODUCTION	1
6.1 Ribonucleic acids: function and structure	1
6.2 RNA modifications	5
6.3 Oxidative stress – its impact on RNA function	9
6.3.1 Oxidative stress – friend or foe?	9
6.3.2 Hypochlorous acid (HOCl)	11
6.3.3 Oxidized nucleosides	12
6.3.4 Abasic sites in nucleic acids resulting from oxidative stress	14
6.4 Detection technologies for RNA modifications and integrity	15
6.4.1 Conventional techniques to investigate RNA integrity	15
6.4.2 LC-MS/MS analysis of RNA nucleosides	16
6.4.3 Mapping of modified ribonucleosides through next-generation sequencing	18
7 MOTIVATION AND OBJECTIVES	21
8 RESULTS AND DISCUSSION	23
8.1 Hypochlorous acid – the oxidizing agent of choice	23
8.1.1 Quantification of free chlorine in HOCl	23
8.1.2 The impact of pH and other compounds on the amount of free chlorine	25
8.2 LC-MS/MS analysis	27
8.2.1 LC-MS/MS method optimization for oxidized nucleosides	27
8.2.2 Detection of ARP-labeled abasic sites via LC-MS/MS	29
8.3 Oxidation of ribonucleosides	33

8.3.1	Pyrimidine oxidation	33
8.3.2	Oxidation of adenosine	38
8.3.3	Guanosine – the most susceptible nucleoside	41
8.3.4	Identification of alternative guanosine oxidation products	43
8.4	The Impact of sequence environment on nucleoside oxidation	47
8.4.1	Oxidation of binary oligoribonucleotides	47
8.4.2	Detection of abasic sites in binary oligoribonucleotides	50
8.5	Oxidation of ribonucleic acids	53
8.5.1	Examining the impact of oxidation on the phosphate backbone of RNA	53
8.5.2	LC-MS/MS quantification of oxidized nucleosides in RNA	56
8.6	Sequencing of oxidized RNA	60
8.6.1	Next-generation sequencing (NGS) method development utilizing synthetic oligonucleotides	60
8.6.2	Investigating the AAS protocol on structurally folded and oxidized IVT-tRNA ^{Asp}	63
9	CONCLUSION AND PERSPECTIVES	67
10	MATERIALS AND METHODS	71
10.1	Materials	71
10.1.1	Chemicals, enzymes and kits	71
10.1.2	Consumables	73
10.1.3	Oligonucleotides	74
10.1.4	Instruments	74
10.1.5	Software	75
10.2	Methods	77
10.2.1	Polymerase Chain Reaction (PCR)	77
10.2.2	<i>In vitro</i> transcription (IVT) of tRNA ^{Asp}	77
10.2.3	Ethanol precipitation	77
10.2.4	Phenol/chloroform extraction	77
10.2.5	Denaturing polyacrylamide gel electrophoresis (PAGE)	78
10.2.6	Preparative denaturing PAGE	78
10.2.7	Quantification of free chlorine in hypochlorous acid (HOCl)	78
10.2.8	Oxidation of ribonucleosides	79
10.2.9	Oxidation of synthetic oligonucleotides and IVT-tRNA ^{Asp}	79
10.2.10	Kinetic UV analysis	79
10.2.11	Preparation of samples before LC-MS/MS analysis	80

10.2.12	Neutral loss scan (NLS) of nucleosides	80
10.2.13	Synthesis of ARP-ribose control	80
10.2.14	LC-MS/MS analysis of ARP-ribose adduct	80
10.2.15	Quantitative LC-MS/MS analysis	81
10.2.16	LC-MS/MS analysis of alternative guanosine oxidation products	82
10.2.17	ARP-labeling	82
10.2.18	³² P-labeling of RNA	83
10.2.19	Next-generation sequencing on an Illumina NextSeq 2000	83
10.2.20	Synthesis of an AP-site containing oligonucleotide	84
10.2.21	Use of artificial intelligence	84
10.2.22	Images and Figures	84
11	APPENDIX	85
12	REFERENCES	97
	CURRICULUM VITAE	109

1 ABSTRACT

RNA plays a pivotal role in gene expression, participating in transcription, translation, and various regulatory processes. Its integrity, structural stability, and functionality are essential for the maintenance of a large number of physiological cellular activities. In this context, damage for example through oxidation or alkylation, can have serious and potentially lethal consequences. However, oxidation reactions are an essential component of aerobic organisms, as their metabolism crucially relies on these reactions. Yet an imbalance towards excessive oxidation leads to long-term damage and is associated with several pathophysiological conditions. Although oxidative damage to DNA has been extensively studied, research on RNA oxidation remains limited.

The objective of this research project was to identify and quantify RNA oxidation products and to assess their structural integrity. A variety of techniques including UV spectroscopy, tandem mass spectrometry, and next-generation sequencing were employed to achieve the most comprehensive results. Additionally, the experiments were conducted at varying levels of complexity, namely on nucleosides, synthetic oligonucleotides in binary and native compositions containing all four nucleotides, and *in vitro* transcribed tRNA.

Oxidation was performed using hypochlorous acid, an oxidizing agent that is involved in the immune response and capable of generating reactive oxygen species. First, the effects of oxidations on nucleosides were analyzed using LC-MS/MS. By identifying and quantifying the corresponding oxidation products, differing reactivities of the individual nucleosides were determined. Uridine exhibited the least alteration, whereas cytidine and adenosine demonstrated comparable levels of oxidation. Guanosine demonstrated the greatest sensitivity as evidenced by the substantial number of oxidation products formed. Furthermore, guanosine was preferentially oxidized in RNA, thereby conferring a scavenging function. Adenosine was found to potentially form dimers, which were not the focus of this study.

Additionally, abasic sites were detected, with a particular prevalence at purine residues. The analysis employed fluorescent labeling and LC-MS/MS to investigate the extent of this damage. Moreover, a next-generation sequencing protocol, developed in collaboration with the ██████████ laboratory in Nancy, France, was employed to map oxidized sites within RNA sequences. The protocol was evaluated by comparing synthetic oligonucleotides with identical sequences containing either guanosine, 8-oxoguanosine, or an abasic site. The application of this protocol to oxidized IVT-tRNA^{Asp} revealed that guanosines exhibited structure-dependent reactivities, with the highest impact observed on guanosine sites located in loops.

The impact of oxidation on RNA at the molecular level were found to be highly dynamic and complex. There are numerous questions regarding the complete identification and quantification of oxidation products including abasic sites and their potential downstream reactions. Nevertheless, a comprehensive understanding of these oxidation processes and their effects is of pivotal importance, given their involvement in a multitude of biological processes and their association with a vast array of pathophysiological conditions.

2 AUSZUG

RNA spielt eine zentrale Rolle im Prozess der Genexpression, wobei sie an der Transkription, der Translation sowie verschiedenen Regulierungsprozessen beteiligt ist. Ihre Integrität, strukturelle Stabilität und Funktionalität sind hierbei von essentieller Bedeutung für die Aufrechterhaltung einer Vielzahl an physiologischen Zellvorgängen. In diesem Zusammenhang kann eine Schädigung, beispielsweise durch Oxidation oder Alkylierung, gravierende und potentiell letale Folgen haben. Oxidationsreaktionen jedoch bilden einen essentiellen Bestandteil aerober Organismen, da ihre Energiegewinnung auf eben jenen Reaktionen beruht. Ein Ungleichgewicht jedoch in Richtung übermäßiger Oxidation führt langfristig zu Schäden und ist assoziiert mit vielerlei pathophysiologischen Zuständen. Obgleich die oxidative Schädigung der DNA in den vergangenen Jahren Gegenstand intensiver Forschungsarbeiten war, sind entsprechende Untersuchungen zu oxidativ geschädigter RNA noch begrenzt.

Das Ziel dieser Forschungsarbeit bestand in der Identifizierung und Quantifizierung gebildeter Oxidationsprodukten in RNA sowie die Analyse der Integrität. Hierbei wurde mittels verschiedener Methoden wie UV-Spektroskopie, Tandem-Massenspektrometrie (LC-MS/MS) und Next-Generation Sequencing ein möglichst umfangreiches Ergebnis erzielt. Neben den Methoden, wurden auch die Experimente auf unterschiedlich komplexer Ebene durchgeführt, beginnend mit den Einzelbestandteilen der RNA, den Nucleosiden, sowie binäre Oligonucleotide, native Oligonucleotide, die aus den vier Hauptnucleotiden synthetisiert wurden und *in vitro* transkribierte tRNA.

Die Oxidationen wurden hierbei mittels hypochloriger Säure durchgeführt, welche *in vivo* an der Immunreaktion beteiligt ist und zur Bildung reaktiver Sauerstoffspezies führt. Zu Beginn wurden die Effekte von Oxidationen auf Nucleoside mittels LC-MS/MS analysiert. Durch Identifizierung und partieller Quantifizierung entsprechender Oxidationsprodukte, konnten unterschiedliche Reaktivitäten der einzelnen Nucleoside bestimmt werden. Uridin erwies sich hierbei als das unreaktivste Nucleosid, gefolgt von Cytidin und Adenosin, die eine vergleichbare Reaktivität zeigten. Guanosin zeigte die größte Empfindlichkeit gegenüber Oxidationsreaktionen ersichtlich an der Vielzahl gebildeter Oxidationsprodukte. Darüber hinaus wurde festgestellt, dass Guanosin auch bevorzugt in RNA oxidiert wird und aufgrund dessen eine Art Schutzfunktion gegenüber den anderen Nucleosiden bildet. Adenosin zeigte eine potentielle Dimerbildung, deren Aufklärung jedoch nicht im Fokus dieser Dissertation stand.

Des Weiteren wurden abasische Stellen detektiert, insbesondere an Purinresten und mittels Fluoreszenzmarkierung und LC-MS/MS-Analyse analysiert. Darüber hinaus wurde eine Next-Generation Sequencing (NGS) Methode in Zusammenarbeit mit dem Labor von ██████████ in Nancy, Frankreich entwickelt, welche die Detektion und Lokalisation oxidierten Guanosins in RNA ermöglicht. Die Methode wurde mittels Vergleiches synthetischer Oligonucleotide evaluiert, die sich an einer definierten Position in der Sequenz durch den Einbau von entweder Guanosin, 8-Oxoguanosin (oxo⁸G) oder einer abasischen Stelle unterschieden. Die Anwendung des Protokolls auf oxidierte IVT-tRNA zeigte, dass Guanosin strukturabhängige Reaktivitäten aufwies, wobei die höchsten Reaktivitäten an Positionen detektiert wurden, die nicht in Watson-Crick Basenpaarungen beteiligt waren.

Die Effekte von Oxidation auf RNA auf molekularer Ebene erwiesen sich als äußerst dynamisch und komplex. Eine Vielzahl an Fragen bleibt bestehen bezüglich der vollständigen Identifizierung und Quantifizierung gebildeter Oxidationsprodukte, einschließlich abasischer Stellen sowie deren potenziellen Folgereaktionen.

Das Verständnis dieser Oxidationsprozesse und deren Auswirkungen ist jedoch von großer Bedeutung, da sie an einer Vielzahl von biologischen Prozessen beteiligt sind und in Zusammenhang mit zahlreichen pathophysiologischen Zuständen stehen.

3 ABBREVIATIONS

$(\text{NH}_4)_2\text{S}_2\text{O}_3$	ammonium thiosulfate
$(\text{NH}_4)_2\text{SO}_4$	ammonium sulfate
$\bullet\text{O}_2^-$	superoxide radical anion
$^1\text{O}_2$	singlet oxygen
5'-P _i	5'-phosphate
A	adenosine
aa	amino acid
AAS	AlkAniline-Sequencing
ac ⁴ C	N ⁴ -acetylcytidine
ACN	acetonitrile
AMP	adenosine monophosphate
AP	apyrimidinic/apurinic site
APE1	apurinic/apyrimidinic endonuclease 1
ARP	aldehyde-reactive probe
ATP	adenosine triphosphate
BSA	bovine serum albumin
C	cytidine
CAT	catalase
CC	collision cell
cDNA	complementary DNA
CID	collision-induced dissociation
Cl ₂	chlorine
Cl ⁵ C	5-chlorocytidine
Cl ⁵ U	5-chlorouridine
Cl ⁸ A	8-chloroadenosine
Cl ⁸ G	8-chloroguanosine
CMP	cytidine monophosphate
CTP	cytidine triphosphate
D	dihydrouridine
DAD	diode array detector
ddNTPs	dideoxynucleotide triphosphate
dMRM	dynamic multiple reaction monitoring
DMS	dimethyl sulfate

Abbreviations

DNA	deoxyribonucleic acid
dNTP	deoxynucleoside triphosphate
DPD	<i>N,N</i> -diethyl-1,4-phenylenediamine
dsDNA	double-stranded DNA
DTT	dithiothreitol
E°	standard redox potential
EDTA	ethylenediaminetetraacetic acid
EM	electron multiplier
ESI	electrospray ionization
FTO	fat mass and obesity-associated protein
G	guanosine
Gm	2'- <i>O</i> -methylguanosine
GMP	guanosine monophosphate
GSH	glutathione
GTP	guanosine triphosphate
H ₂ O	water
H ₂ O ₂	hydrogen peroxide
H ₂ SO ₄	sulfuric acid
HED	high-energy dynode
HEPES	4-(2-hydroxyethyl)-1-piperazineethanesulfonic acid
HO ⁻	hydroxyl anion
HO [•]	hydroxyl radical
ho ⁵ C	5-hydroxycytidine
ho ⁵ U	5-hydroxyuridine
HOCl	hypochlorous acid
HOX	hypohalous acid
HPLC	high performance liquid chromatography
HRMS	high-resolution mass spectrometry
I	inosine
I ₂	iodine
IP	immunoprecipitation
IVT	<i>in vitro</i> transcription
IVT-tRNA ^{Asp}	<i>in vitro</i> transcribed tRNA-aspartate
K ₂ SO ₄	potassium sulfate
KHCO ₃	potassium bicarbonate
KI	potassium iodide
KIO ₃	potassium iodate

LC-MS/MS	liquid chromatography-tandem mass spectrometry
LOD	limit of detection
LOQ	limit of quantification
<i>m/z</i>	mass-to-charge ratio
m ¹ G	1-methylguanosine
m ^{2,2} G	<i>N</i> 2, <i>N</i> 2-dimethylguanosine
m ² G	<i>N</i> 2-methylguanosine
m ³ C	3-methylcytidine
m ⁵ C	5-methylcytidine
m ⁶ A	<i>N</i> 6-methyladenosine
m ⁶ Am	<i>N</i> 6,2'-dimethyladenosine
m ⁷ G	7-methylguanosine
mchm ⁵ U	5-(carboxyhydroxymethyl)uridine methyl ester
METTL14	methyltransferase-like 14
METTL3	methyltransferase-like 3
MgCl ₂	magnesium chloride
miRNA	micro RNA
MPG	Human methylpurine DNA glycosylase
MPO	myeloperoxidase
MQ	ultrapure water
MRM	multiple reaction monitoring
mRNA	messenger RNA
MS	mass spectrometry
Na ₂ HPO ₄	disodium hydrogen phosphate
Na ₂ S ₂ O ₃	sodium thiosulfate
NADP ⁺	nicotinamide adenine dinucleotide phosphate
NADPH	reduced form of nicotinamide adenine dinucleotide phosphate
NaOH	sodium hydroxide
NDP	nucleoside diphosphate
NGS	next-generation sequencing
NH ₄ HCO ₃	ammonium bicarbonate
NH ₄ OAc	ammonium acetate
NLS	neutral loss scan
Nm	2'- <i>O</i> -methylated nucleoside
NMP	nucleoside diphosphate
NMR	nuclear magnetic resonance
NormGcount	normalized G count

Abbreviations

NTP	nucleoside triphosphate
O ₂	molecular oxygen
O ₃	ozone
ONOO ⁻	peroxynitrite
oxo ⁸ A	8-oxoadenosine
oxo ⁸ G	8-oxoguanosine
PAGE	polyacrylamide gel electrophoresis
PCR	polymerase chain reaction
PET	peptide exit tunnel
PNK	polynucleotide kinase
PNPase	polynucleotide phosphorylase
PS	pentostatin
PTC	peptidyl transferase center
Q	queuosine
Q1	quadrupole 1
Q2	quadrupole 2
QQQ	triple quadrupole
r2Ih	5-carboxamido-5-formamido-2-iminohydantoin
rDiz	diiminoimidazole
rGh	guanidinohydantoin
rIa	iminoallantoin
rIz	imidazolone
RNA	ribonucleic acid
RNS	reactive nitrogen species
ROS	reactive oxygen species
RP	ribosomal protein
RP-18	reversed phase C18
rRNA	ribosomal RNA
rSp	spiroiminodihydantoin
RT	reverse transcription
rZ	oxazolone
<i>S. c.</i>	<i>Saccharomyces cerevisiae</i>
SARS-Cov-2	severe acute respiratory syndrome coronavirus type 2
SD	standard deviation
siRNA	small interfering RNA
snRNA	small nuclear RNA
SOD	superoxide dismutase

ssDNA	single-stranded DNA
TBE	tris/borate/ethylenediaminetetraacetic acid
TEMED	<i>N,N,N',N'</i> -tetramethylethylenediamine
tRNA	transfer RNA
U	uridine
UMP	uridine monophosphate
UTP	uridine triphosphate
UTR	untranslated region
UV	ultraviolet
Ψ	pseudouridine
YTHDF1	YTH <i>N</i> 6-methyladenosine RNA binding protein F1

4 LIST OF FIGURES

Figure 1. Structural composition of RNA and its building blocks.	2
Figure 2. RNA synthesis and function in a eukaryotic cell.	3
Figure 3. Structural and functional features of mRNA, tRNA and rRNA.	4
Figure 4. Examples of modified nucleosides in RNA.	7
Figure 5. Exogenous and endogenous sources of oxidative stress and their intracellular impact.	10
Figure 6. Oxidized nucleosides correlated with oxidative stress and cellular damage.	13
Figure 7. Mechanism for cross-link formation of oxidized adenosines.	14
Figure 8. HPLC-MS/MS methodology employed for nucleoside analysis.	16
Figure 9. General NGS process via sequencing-by-synthesis.	19
Figure 10. AlkAniline reaction scheme from Helm <i>et al.</i> 2021. ¹²¹	20
Figure 11. Quantification procedure of Cl ₂ in HOCl using the DPD method.	24
Figure 12. Influences of pH and selected compounds on detected Cl ₂ amounts.	25
Figure 13. Optimization of HPLC-MS/MS method for oxidized nucleosides.	28
Figure 14. LC-MS/MS method evaluation of the ARP-ribose product.	31
Figure 15. Oxidation on uridine revealed only minor changes analyzed via UV and LC-MS.	34
Figure 16. Cytidine oxidation results in the quantitative formation of 5-chlorocytidine (Cl ⁵ C).	36
Figure 17. UV and LC-MS results of oxidized adenosine.	39
Figure 18. Cross-link formation between oxo ⁸ A and A induced by oxidation.	40
Figure 19. Guanosine nucleoside oxidation exhibited high reactivity resulting in a variety of products.	42
Figure 20. Oxidation products of guanosine (light pink) generated upon two-electron (e ⁻) (top) and four-electron (bottom) oxidation reactions.	44
Figure 21. Identification of alternative guanosine (G) oxidation products using ¹² C-, ¹³ C- and ¹⁵ N-guanosine.	45
Figure 22. Binary oligonucleotides (GU, CU, and AU combinations) show distinct behaviors upon oxidation.	47
Figure 23. Quantification of oxidation products in binary oligonucleotides revealed similar sensitivities towards oxidation as detected in nucleosides.	49
Figure 24. Detection of abasic sites using an aldehyde-reactive probe in binary oligonucleotides.	51

- Figure 25. Visualization of RNA integrity by gel electrophoresis using ^{32}P - and ARP-labeling. 54
- Figure 26. LC-MS/MS quantification of oxidized nucleosides derived from IVT-tRNA^{Asp} and an unmodified oligonucleotide. 57
- Figure 27. Schematic illustration of the AlkAniline-Sequencing protocol exemplified for guanosine (G), oxo⁸G and an abasic (AP) site. 61
- Figure 28. Comparing signals resulting from the AlkAniline-sequencing protocol comparing alkaline and magnesium fragmentation on three oligonucleotides including either G, oxo⁸G, and an abasic (AP) site at position 16. 63
- Figure 29. AAS was performed on folded *in vitro* transcribed tRNA^{Asp} revealing prominent signals exclusively at G residues. 64

5 LIST OF TABLES

Table 1. Chemicals, enzymes and kits used for conducting experiments described in this PhD thesis.	71
Table 2. Consumables used for conducting experiments described in this PhD thesis.	73
Table 3. Oligonucleotides used during this PhD thesis.	74
Table 4. Instruments used for conducting experiments described in this PhD thesis.	74
Table 5. Software used during this PhD thesis.	75
Table 6. LC-MS/MS parameters for modified nucleosides measured in dMRM mode.	82
Table 7. Mass transitions of ^{12}C , ^{13}C , and ^{15}N isotopes for alternative guanosine oxidation products.	82

6 INTRODUCTION

6.1 Ribonucleic acids: function and structure

Ribonucleic acids (RNA) play a central role in biological systems. According to the central dogma of molecular biology, RNA serves as an intermediate between nuclear deoxyribonucleic acids (DNA), which stores genomic information, and functional proteins. However, RNA's role is more intricate than merely transferring genetic sequences from DNA to the cytosol for translation. It encompasses the coding and decoding of genetic information, protein synthesis, and various roles in the regulation of gene expression.¹⁻³

The execution of these diverse functions relies on the structure of RNA as a polymer. Each building block consists of a ribose sugar with an additional hydroxyl group at the 2'-carbon compared to DNA. A phosphate group is attached at the 5'-carbon and a nucleobase is linked via an *N*-glycosidic bond to C1'. The four main nucleobases in RNA are uracil, cytosine, adenine, and guanine, which are nitrogen-containing heterocycles, as shown in Figure 1A. Uracil, unique to RNA, and cytosine are pyrimidines, whereas adenine and guanine are purines (Figure 1B). Figure 1C illustrates the structural differences among nucleobases, nucleosides, and nucleotides. Nucleosides consist of a ribose moiety attached to the nucleobase, whereas nucleotides additionally include one or more phosphate groups at the 5'-OH of the ribose.⁴⁻⁶ Moreover, nucleotides can exist as mono-, di-, and triphosphates also referred to as nucleoside mono-, di- or triphosphates (NMP, NDP, or NTP). In the context of RNA, nucleosides are commonly indicated with the following nomenclature: uridine (U), cytidine (C), adenosine (A), and guanosine (G).

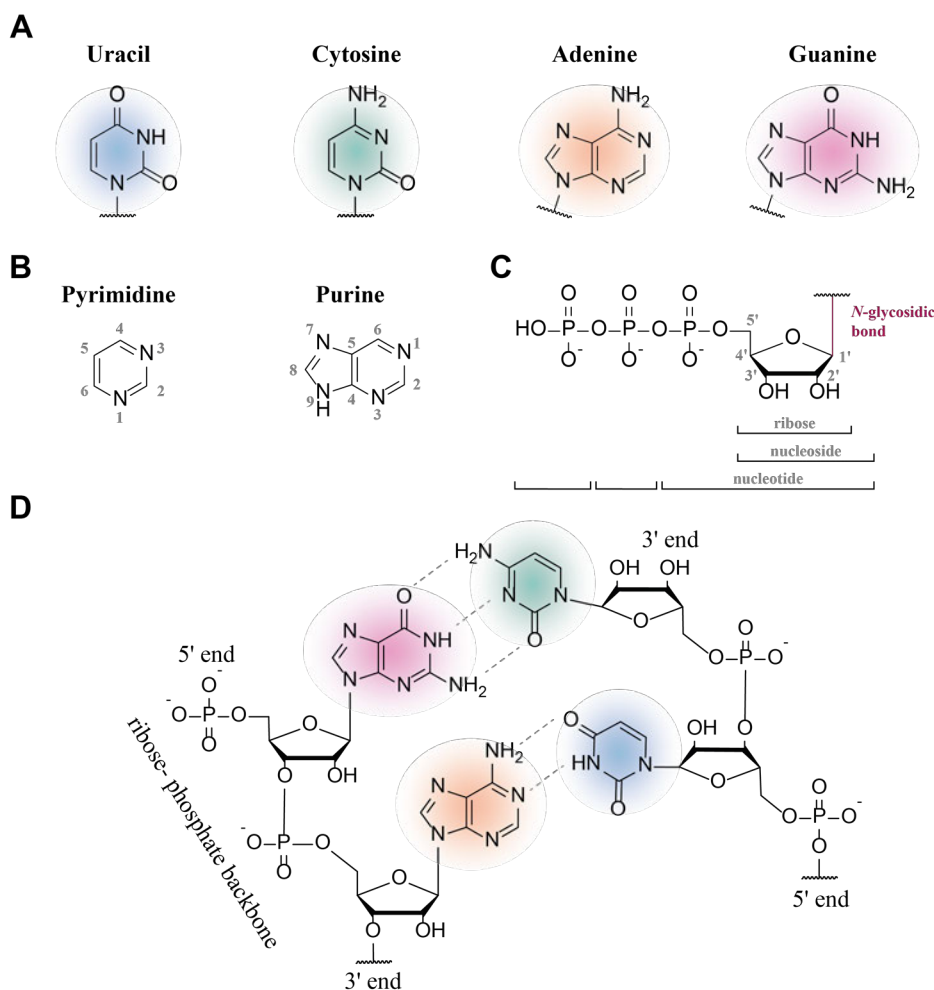


Figure 1. Structural composition of RNA and its building blocks.

A The nucleobases in RNA are uracil (blue), cytosine (green), adenine (orange), and guanine (pink). **B** Pyrimidine and purine heterocycles displayed with their conventional atom numbering. **C** Structure of nucleosides and nucleotides highlighting the ribose moiety and the phosphate groups attached to the 5'-OH of the ribose. **D** The primary structure of RNA is defined by the sequence of nucleotides within the RNA chain oriented from the 5'- to the 3'- end of the ribose-phosphate backbone. Secondary structures form via base pairing according to Watson-Crick interactions, with guanosine (pink) pairing with cytidine (green) and adenosine (orange) pairing with uridine (blue). Figure adapted from Zhou *et al.*⁷

Figure 1D shows the molecular structure of an RNA chain, consisting of a ribose-phosphate backbone with nucleobases attached to the ribose in a specific sequence. This sequence referred to as primary structure, can form secondary structures upon hydrogen bonding according to Watson-Crick base pairing.^{5,6,8} In RNA, Watson-Crick base pairs form between guanosine (pink) and cytidine (green), as well as adenosine (orange) and uridine (blue). Inter- and intramolecular base pairing leads to secondary structures such as hairpins, loops, and stems.⁹⁻¹²

A proper three-dimensional RNA folding, defined as a tertiary structure is essential for the specific function of RNAs. Catalytic activities, protein binding, and other recognition mechanisms depend on the integrity of the intended structure.¹³ Moreover, structural changes are important for activity regulation, allowing RNAs to switch between inactive and active states. This is particularly important in the dynamic environment of living organisms in all kingdoms of life.^{4,10,11,14-17}

In eukaryotic cells, RNA is synthesized during transcription in the nucleus, where DNA serves as a template for the complementary RNA molecule (step 1). In the vast majority of cases, this primary RNA transcript is initially premature and requires further processing (step 2) before being transported from the nucleus to the cytosol (step 3). After translocation, RNA structure and function are further fine-tuned by enzymatic addition of post-transcriptional modifications (step 4) resulting in specific modification patterns that regulate RNA activity and function, or act as markers for recognition by specific proteins, thereby initiating downstream processes such as degradation or translation.^{4,9,14-16,18}

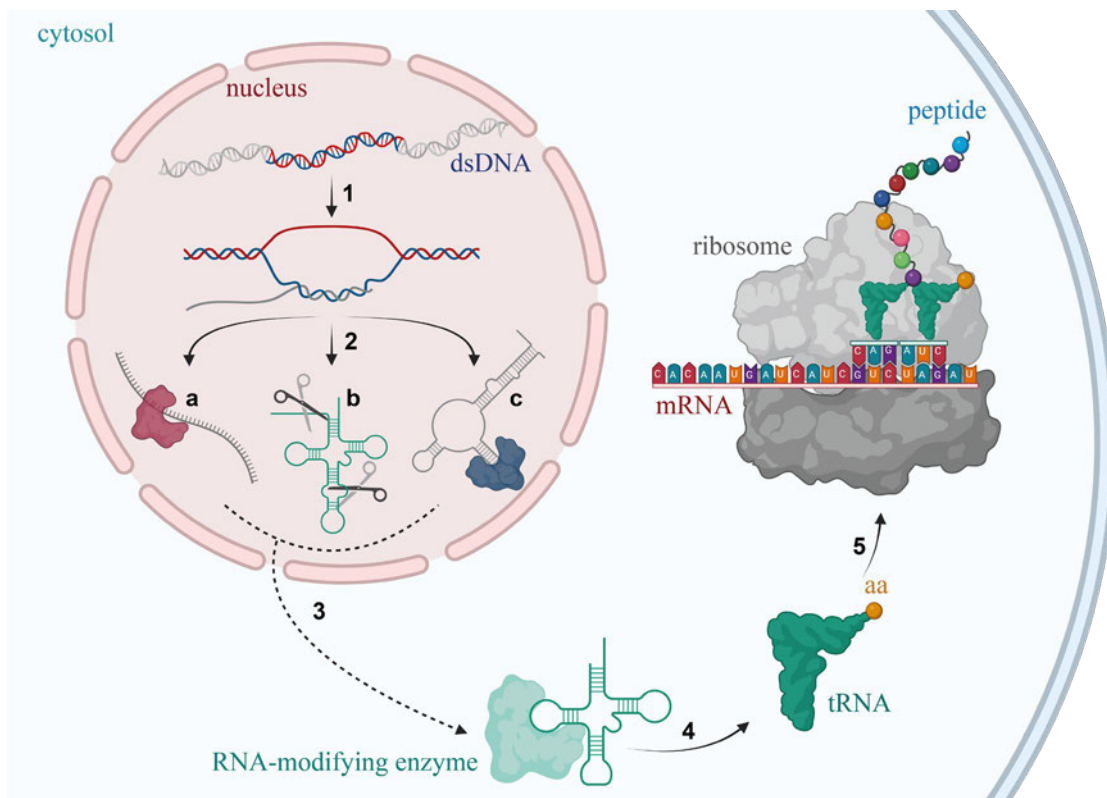


Figure 2. RNA synthesis and function in a eukaryotic cell.

Double-stranded DNA (dsDNA) serves as a template for RNA synthesis. The gene of interest (highlighted in red and blue) is transcribed into RNA (step 1) in the nucleus. The primary RNA transcript, whether messenger RNA (mRNA, a), transfer RNA (tRNA, b) or ribosomal RNA (rRNA, c), is initially immature and undergoes several maturation steps within the nucleus (step 2), such as splicing, and is afterwards translocated to the cytosol (step 3). RNA modifications on nucleosides are another crucial maturation step, introduced by RNA-modifying enzymes that are dynamically regulated and responsive to various stimuli. Only mature RNAs (step 4), which are properly folded, stable and functional, can perform their designated roles. One of their most important function is translating genetic information from mRNAs into proteins by transferring amino acids (aa) from tRNAs to the growing peptide chain in the peptidyl transfer center of ribosomes (step 5). Created with BioRender.com (2024).

RNA is classified into several species based on their function. The three major RNA species involved in protein synthesis are messenger RNA (mRNA), transfer RNA (tRNA), and ribosomal RNA (rRNA).^{10,11,14-16,19} These three major RNA species – mRNA, rRNA and tRNA, are indispensable for protein synthesis during translation. In this process, a specific gene transcribed as mRNA is translated into a protein based on the mRNA sequence. Ribosomes facilitate this process by guiding tRNAs to the decoding center where the mRNA is bound. When the anticodon of the tRNA correctly base pairs with the codon in the mRNA sequence, the ribosome catalyzes the transfer of the amino acid attached to the tRNA to the growing peptide chain.

Figure 3 illustrates the major structural features of eukaryotic mRNA, tRNA and rRNA. Messenger RNA which functions as a template for protein synthesis can be divided into five sections: The 5'-end features a 7-methylguanosine (m^7G) modified cap structure (dark yellow), linked via a 5'-5' triphosphate bridge to the mRNA transcript as well as the 5'-untranslated region (5'-UTR in light yellow) which is crucial in regulating translation processes. The downstream coding sequence (shown in pink) begins with the start codon AUG and ends with either UAG, UGA, or UAA. The 3'-end of mRNAs consists of a 3'-UTR, followed by the poly(A) tail.^{4,16,18,20,21} Transfer RNAs are characterized by their distinctive cloverleaf structure, which folds into an L-shaped tertiary structure (Figure 3B). The upper end of the cloverleaf features the acceptor stem (in blue), carrying the amino acid at the 3'-end. The opposing anticodon loop (in red) comprises the anticodon sequence from position 34 to 36, which is complementary to the mRNA codon. The mRNA codon defines the amino acid during translation and consists of a nucleobase triplet.³ The left arm of the cloverleaf comprises the D stem-loop (in light pink), interacting with the T Ψ C loop (in green), fundamental for the L-shaped tertiary structure. Besides, tRNA contains a variable loop of varying length, resulting in a total length of cytosolic tRNA between 76 to 93 nucleotides.^{4,11,15}

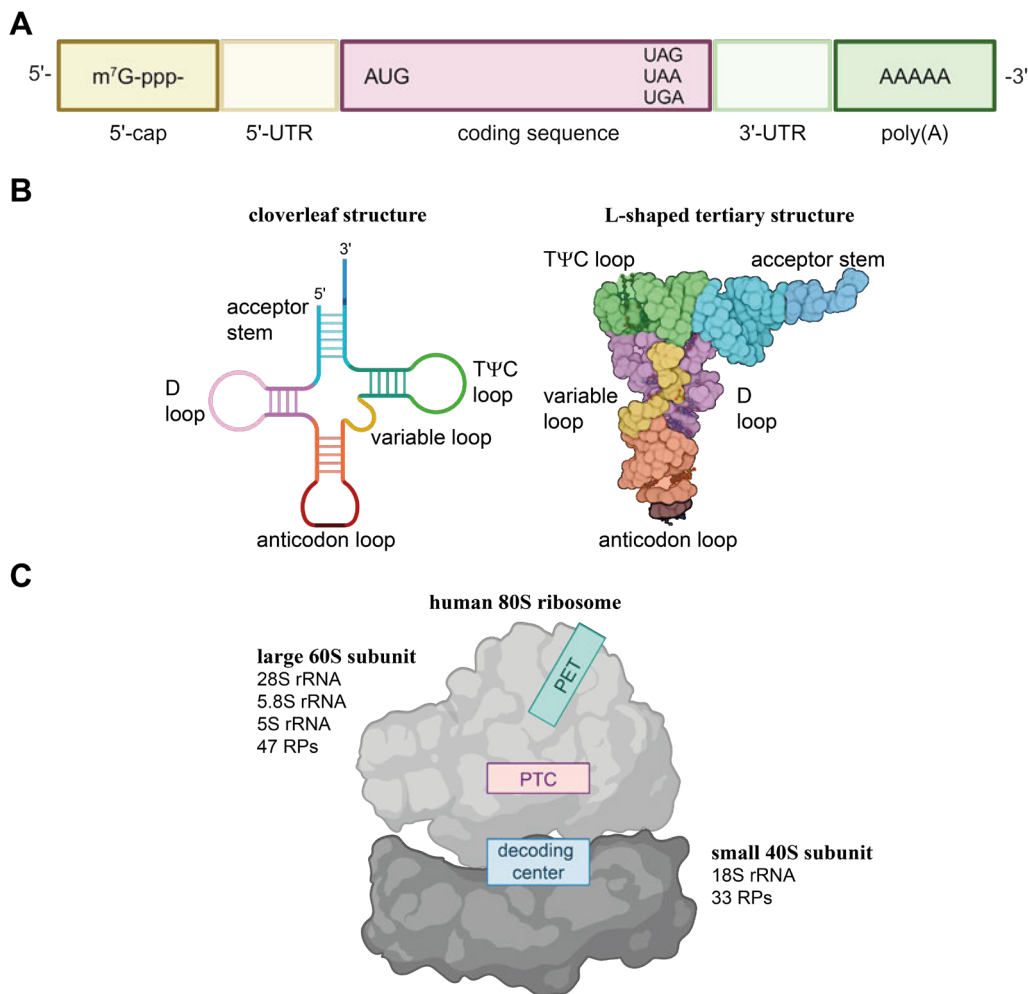


Figure 3. Structural and functional features of mRNA, tRNA and rRNA.

A Eukaryotic mRNA is structurally divided into five sections: the 5'-end features a 7-methylguanosine (m^7G) cap followed by the 5'-untranslated region (UTR), the coding sequence including the start codon AUG and one of the three stop codons

(UAG, UGA or UAA). Downstream of the coding region is the 3'-UTR, and the 3'-end terminates with a poly(A) tail. **B** The highly structured tRNA molecule adopts a cloverleaf configuration in its secondary structure (left). The acceptor stem (blue) holds the corresponding amino acid and is at the opposite of the anticodon stem-loop (red). The variable loop (yellow) is located in between the acceptor stem and the TΨC-loop. The TΨC-loop (green) interacts with the D-loop (pink) to form the L-shaped tertiary structure (right) which is essential for tRNA function. Figure adapted from Schimmel *et al.*¹⁷ **C** The human 80S ribosome is a dimer formed by the large 60S subunit and the small 40S subunit including four ribosomal RNAs and several ribosomal proteins. The large 60S subunit consists of the 28S rRNA, 5.8S rRNA, and 5S rRNA, which interact with 47 ribosomal proteins (RPs). The peptidyl transferase center (PTC, in pink) and the peptide exit tunnel (PET, in green) are located in the large subunit. The small 40S subunit comprises the 18S rRNA and 33 RPs, forming the decoding center (in blue). Created with Biorender.com (2024).

Ribosomal RNAs constitute up to 80% of total cellular RNA and play a pivotal role in forming the ribosome in complex with numerous ribosomal proteins (RPs). Figure 3C illustrates the prominent structure of the ribosome as a complex of a large and a small subunit. The large 60S subunit is formed by the 28S, the 5.8S, and the 5S rRNAs, along with 47 RPs, collectively forming the peptidyl transferase center (PTC, in pink) and the peptide exit tunnel (PET, in green). The small 40S subunit is a complex of the 18S rRNA and 33 RPs, which bind the mRNA and form the decoding center (blue).^{10,14,19} Besides these RNA species, several others are known such as micro RNA (miRNA), small interfering RNA (siRNA), and small nuclear RNA (snRNA) that are involved in various processes such as gene expression regulation, gene silencing, mRNA splicing, and others.¹²

6.2 RNA modifications

Accomplishing the diverse tasks and achieving proper tertiary structures is not trivial, particularly given the limited variety of the four main nucleosides in RNA. To enhance the chemical and structural properties of these nucleosides, the addition or adaptation of various chemical groups has evolved as a key mechanism. The majority of modifications are introduced post-transcriptionally, either in the nucleus or in the cytosol. However, for selected cases co-transcriptional incorporation has been discussed.²² These modifications serve as regulators of RNA maturation, as enzyme recognition sites, and play a pivotal role in gene expression regulation, splicing, degradation, and signaling pathways. Furthermore, RNA modifications are essential for stabilizing tertiary structures, which is crucial for maintaining functional integrity.^{10,11,14-16,20,23}

Since the first discovery in 1951, more than 170 modified nucleosides have been identified. These modifications range from simple methylations to the addition of complete amino acids or multi-step, enzymatically catalyzed additions of large side chains.^{4,11,14,15,24} By attaching functional groups, the molecular properties of nucleosides, particularly if interfering with the Watson-Crick base pairing capabilities, can be significantly altered. Changes in the interface can influence molecular interactions, such as those between tRNA and mRNA during anticodon-codon recognition, and can induce structural changes, shifting the RNA between active and inactive states. These effects are crucial for regulating gene expression, specific signaling pathways, and the cell's response to external stimuli. The study of RNA modifications and their role in regulating cellular function is known as epitranscriptomics. This field encompasses chemical alterations on nucleoside that are not encoded by the DNA sequence, focusing on modifications induced at the RNA level. Representative RNA modifications include

6-methyladenosine (m^6A), which is involved in mRNA maturation, transcription regulation, and cancer.^{16,25-28} Pseudouridine (Ψ), a common modification in tRNAs and rRNAs, is essential for structural stability;^{14-16,29} and 2'-*O*-methylations (Nm), which play roles in immune response regulation via receptor recognition and directly affect ribose confirmation, which is crucial for RNA helix stabilization.^{11,15,23,30}

RNA modifications are present across all RNA species, although their distribution varies. One common and well-studied modification in mRNA is m^6A (Figure 4A), found in most eukaryotes and distributed throughout the entire sequence. m^6A recruits splicing factors that regulate the inclusion or exclusion of specific exons, thereby facilitating alternative splicing in the nucleus. Additionally, the nuclear export of mRNA transcripts into the cytoplasm relies on m^6A , which subsequently initiates and enhances translation. m^6A also plays a role in mRNA degradation, acting as a marker for proteins involved in RNA decay. This modification exemplifies the dynamic regulation of RNA modifications throughout their lifecycle. The writer protein complex, primarily METTL3/METTL14, introduces the methyl group in the nucleus. Reader proteins, such as YTHDF1, recognize this modification, bind the corresponding transcript, and initiate downstream processes including m^6A -dependent translation. Eraser proteins, like FTO, remove the modification, thus regulating the aforementioned processes.^{4,16,26} Beyond m^6A , there are other modifications on mRNA such as Ψ , 1-methyladenosine (m^1A), inosine (I), 5-methylcytidine (m^5C), *N*4-acetylcytidine (ac^4C), 7-methylguanosine (m^7G), 2'-*O*-methylated nucleosides and *N*6,2'-*O*-dimethyladenosine (m^6Am).^{4,20} A substantial proportion of these modifications also occur on eukaryotic tRNA, which contains up to 25% modified nucleosides.¹⁸ The high quantity of modifications in tRNA can be partly attributed to its function and structure. The L-shaped tertiary structure of all tRNAs is essential for their recognition by the ribosome and the translation process. Simultaneously, tRNAs must be unique to ensure precise codon recognition, reading frame maintenance, and correct aminoacylation. These dual functionalities necessitate precise adjustments, achieved through nucleoside modifications.^{4,11,15,18}

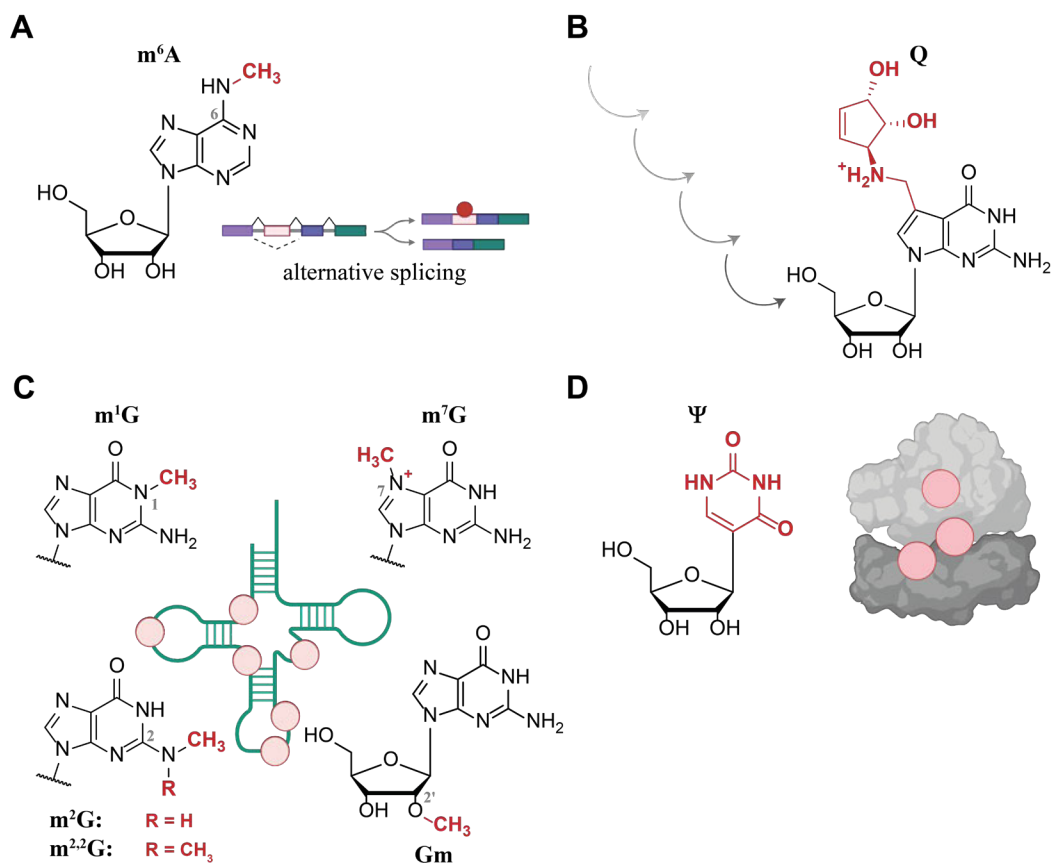


Figure 4. Examples of modified nucleosides in RNA.

A 6-methyladenosine (m^6A) is present in mRNA and involved in processes such as alternative splicing and mRNA maturation. **B** Queuosine (Q) is an example of a complex modification that is introduced by several enzymatically catalyzed reactions. **C** Methylated guanosine nucleosides present at several positions in tRNA: 1-methylguanosine (m^1G), *N*2-methylguanosine (m^2G), *N*2,*N*2-dimethylguanosine ($m^{2,2}G$), 2'-*O*-methylguanosine (Gm), and 7-methylguanosine (m^7G). **D** Pseudouridine (Ψ) is characterized by its C-C glycosidic bond and its capacity to enhance structural stability as in the ribosome. Created with Biorender.com (2024).

This also explains the high diversity of modifications present in tRNA, which include complex structural features such as queuosine (Q, shown in Figure 4B). Q is located at position 34 in the anticodon of tRNAs, also known as the wobble position, which hosts many extraordinary modifications. This position is crucial for codon recognition and reading frame maintenance, in addition to modified nucleosides at position 37. Like mRNA, the tRNA modification pattern is dynamically regulated, allowing adaptations to environmental stresses and metabolic changes. Q is enzymatically induced through multi-step synthesis involving several enzymes, starting from guanosine. Guanosine itself exists in various modified forms displayed in Figure 4C, such as 1-methylguanosine (m^1G), *N*2-methylguanosine (m^2G), *N*2,*N*2-dimethylguanosine ($m^{2,2}G$), 2'-*O*-methylguanosine (Gm), and 7-methylguanosine (m^7G). Comparing these modification patterns highlights the different effects depending on the position of the introduced modification, such as a methyl group. The most significant changes occur when modifications disrupt hydrogen bonding on the Watson-Crick face, as seen with m^1G , m^2G , or $m^{2,2}G$, directly affecting secondary structures.^{15,18} m^7G adds a positive charge to the nucleoside, significantly impacting interactions with neighboring nucleosides and influencing mRNA translation.³¹ This partly explains the involvement of m^7G deficiencies in diseases such as cancer.^{15,31,32} m^1G is also associated with neurological disorders

indicating its impact on pathophysiological conditions.^{4,15} Gm primarily affects tRNA structure, playing a role in codon recognition and translation efficiency.²³ 2'-*O*-modifications are also prevalent in rRNA, contributing to the ribosome's structure and predominantly clustering at functionally important sites such as the decoding center, the tRNA binding site, the peptidyltransferase center, and the intersubunit interface. Methylation at these sites suggests its involvement in enhancing interactions among participating RNAs and proteins.^{14,23} Another rRNA-associated modification is pseudouridine (Ψ , see Figure 4D), the first modified nucleoside to be discovered in 1951 and the most abundant RNA modification.²⁹ Structurally, Ψ is an isomer of uridine that changes from an N1 linkage to the ribose to a C5-glycosidic bond. It is found in all domains of life within nearly all RNA classes. Although its function is not fully elucidated, it is known that Ψ stabilizes tertiary structures by enhancing base stacking interactions and Watson-Crick base pairing properties. Consequently, its high abundance in rRNA contributes to structural stability and enhances inter- and intramolecular nucleotide interactions.^{4,14,29,33}

6.3 Oxidative stress – its impact on RNA function

The preceding chapter on modified nucleosides and their effects on RNA structure and function provides insight into the potential impacts of damaged nucleosides. Just as intentional modifications influence RNA properties, unintended modifications can similarly affect RNA. One significant source of unintentional nucleoside modification is oxidative stress.

6.3.1 Oxidative stress – friend or foe?

Oxidative stress is defined as an imbalance between oxidizing and reducing agents in living organisms.³⁴⁻³⁶ While a certain level of oxidants is crucial for aerobic organisms, an imbalance favoring elevated oxidants disrupts proper cellular function.^{34,37,38} Increased levels of oxidizing agents arise from both endogenous and exogenous sources. Exogenous sources of oxidative stress include UV photooxidation, ozone, γ -irradiation, chemicals, and environmental toxins.^{37,38} In contrast, endogenous oxidative stress arises from physiological processes including the mitochondrial respiratory chain, NADPH oxidases, peroxisomes, and other redox-active molecules such as oxygenases.^{34-36,39}

Figure 5 provides an overview of oxidative stress, delineating both exogenous (Figure 5A) and endogenous (Figure 5B) sources that result in the generation of reactive oxygen species (ROS). ROS are highly reactive molecules that impact various biomolecules including proteins, lipids, DNA, and RNA.³⁴⁻³⁶ Figure 5C illustrates the target sites of ROS on rRNA, mRNA, and tRNA. The main sites of oxidation primarily affect the ribonucleobase leading to notable changes in their functionality. RNA function relies on Watson-Crick base pairing which involves the formation of hydrogen bonds between nucleotides as previously described in Chapter 6.1. These interactions are of critical importance for any RNA, due to their determined structure and, consequently, its function as outlined in Chapter 6.2 on RNA modifications. Key processes affected include codon recognition, ribosome assembly, and the provision of tRNA and mRNA binding sites as well as tRNA aminoacylation. Errors in any of these processes have profound consequences for cellular function.^{35,37,38,40-44}

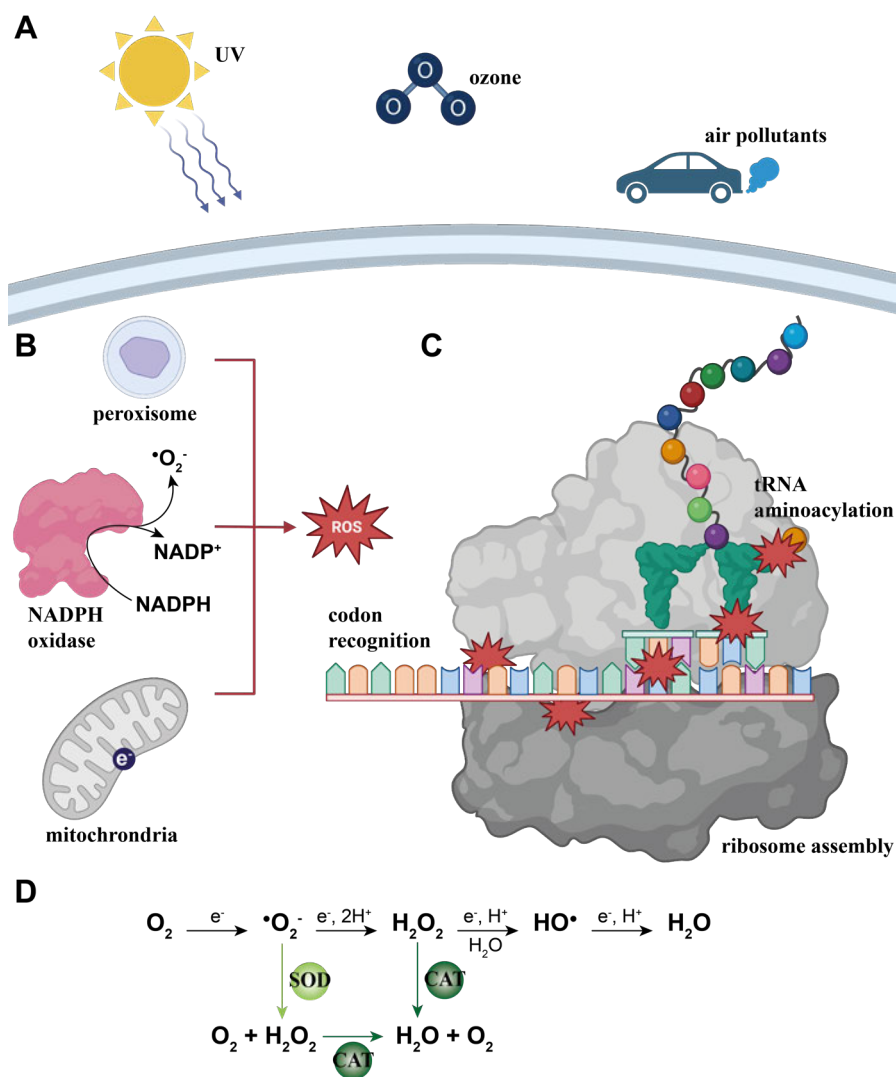


Figure 5. Exogenous and endogenous sources of oxidative stress and their intracellular impact.

A UV irradiation, ozone, and air pollutants represent significant exogenous sources of oxidative stress. **B** Intracellularly, peroxisomes, NADPH oxidases, and mitochondria are the primary source of reactive oxygen species (ROS). **C** Oxidatively damaged RNA interferes with processes such as codon recognition, tRNA aminoacylation, and ribosome assembly. **D** Reduction of oxygen (O_2) to reactive oxygen species (ROS): superoxide radical anion ($\cdot\text{O}_2^-$), hydrogen peroxide (H_2O_2), and hydroxyl radical ($\text{HO}\cdot$). The final reduced state is water (H_2O). Two enzymes are primarily involved in the detoxification of ROS: superoxide dismutase (SOD), which acts on $\cdot\text{O}_2^-$, and catalase (CAT), which reduces H_2O_2 to H_2O . Created with Biorender.com (2024).

At the molecular level, oxidative stress is manifested through ROS. These ROS include the superoxide radical anion $\cdot\text{O}_2^-$, hydrogen peroxide H_2O_2 , hydroxyl radicals $\text{HO}\cdot$, singlet oxygen $^1\text{O}_2$, and ozone O_3 , some depicted in Figure 5D. The primary source of superoxide radical anions $\cdot\text{O}_2^-$, hydrogen peroxide H_2O_2 and hydroxyl radicals $\text{HO}\cdot$ is a direct electron transfer to molecular oxygen.³⁵ The superoxide radical anions $\cdot\text{O}_2^-$ is primarily generated in mitochondria via electron transfer during cellular respiration and through NADPH oxidases.^{34-36,39} Hydrogen peroxide H_2O_2 is formed by the dismutation of superoxide radical anions $\cdot\text{O}_2^-$ catalyzed by the enzyme superoxide dismutase (SOD, see Figure 5D). Although hydrogen peroxide H_2O_2 is less reactive than superoxide radical anions $\cdot\text{O}_2^-$, its prolonged half-life and the ability to diffuse through cell membranes increase the potential for damage. H_2O_2 is a substrate for several antioxidant enzymes, including

catalase (CAT, shown in Figure 5D), which detoxifies it into water H_2O and molecular oxygen O_2 . However, hydrogen peroxide H_2O_2 also initiates the Fenton reaction, generating hydroxyl anions OH^- and hydroxyl radicals HO^\bullet in the presence of metal cations such as Fe^{2+} . The hydroxyl radical HO^\bullet is particularly potent, capable of rapidly attacking nearby molecules such as lipids, nucleic acids, or proteins.^{34,36}

To combat elevated oxidant levels, cells employ antioxidant enzymes, such as SOD and CAT, as well as non-enzymatic antioxidants, including glutathione (GSH), NADPH, and vitamin C.^{34,36} However, the capacity of these antioxidant defense systems is limited. Long-term exposure to high levels of oxidants can overwhelm the cell's repair mechanisms leading to cellular damage and the onset of pathophysiological diseases. In such scenarios, the equilibrium shifts progressively towards ROS. This leads to the deterioration of biomolecules including proteins, lipids, DNA, and RNA, as well as the activation of several signaling pathways.^{34,37,38,42,45,46} A number of diseases are associated with elevated levels of oxidative stress including cancer, neurodegenerative and cardiovascular diseases, diabetes, inflammation, and at advanced ages.^{34,37,40,44,47-51}

In addition to ROS, oxidative stress involves reactive nitrogen species (RNS),^{34,36} hypohalous acid (HOX),^{34,46,52} and direct electron transfer.^{34,53} RNS and HOX are derived from the initial generation of superoxide radical anions $\bullet\text{O}_2^-$ and hydrogen peroxide H_2O_2 . Their damaging potentials in the form of peroxynitrite (ONOO^-), and HOX are even greater than that of primary ROS.^{52,54}

6.3.2 Hypochlorous acid (HOCl)

The innate immune system employs hypochlorous acid (HOCl), a potent HOX, to combat pathogens during immune response.^{46,52} Neutrophils and macrophages, two types of immune cells, express the enzyme myeloperoxidase (MPO) which catalyzes the oxidation of chloride ions Cl^- by hydrogen peroxide H_2O_2 resulting in the formation of HOCl.^{52,54} HOCl, a weak acid ($\text{pK}_a = 7.46$) exists in near equimolar concentrations with its deprotonated form, OCl^- , under physiological conditions. The redox potential of HOCl ($E^\circ = 1.48 \text{ V}$) is higher than that of OCl^- ($E^\circ = 0.9 \text{ V}$), enhancing its damaging potential as it is also able to freely diffuse through cell membranes.^{46,52} In cellular environments HOCl generates several secondary oxidants depending on local conditions, but chlorination and oxygenation are two major mechanisms. Hydroxyl radicals HO^\bullet are produced in Fenton-like reactions and the presence of superoxide radical anions $\bullet\text{O}_2^-$ which can also catalyze the formation of singlet oxygen $^1\text{O}_2$. Under low pH, HOCl forms Cl_2 , if Cl^- is present and UV exposure photolyzes HOCl into chlorine Cl^\bullet and hydroxyl radicals HO^\bullet .⁴⁶ HOCl primarily affects biomolecules through chlorination of amines, oxidation of sulfur-containing compounds as in amino acids and unsaturated hydrocarbons such as fatty acids. Nucleic acids and nucleotides are either chlorinated or oxygenated at their nitrogen-containing heterocycles. Investigations of RNA oxidation by HOCl includes *in vitro*⁵⁵⁻⁵⁷ and *in cellulo*⁵⁷⁻⁶⁰ studies on nucleosides^{56,61,62} and RNA. Typically analyzed products include chlorinated and oxygenated compounds such as 5-chlorocytidine (Cl^5C), 8-chloroadenosine (Cl^8A), and -guanosine (Cl^8G) as well as 8-oxoadenosine (oxo^8A) and -guanosine (oxo^8G) and the corresponding 5-hydroxypyrimidines (ho^5C and ho^5U).^{46,52,63-65} The abundance of these products is highly dependent on reaction conditions and their presence can lead to several downstream effects such as alterations

in transcription and translation^{37,59,66} and also promotes inflammatory diseases^{35,63} which was particularly investigated for Cl⁸A.^{57,60,67}

Additionally, the sodium salt of HOCl is widely used as a chemical disinfectant in freshwater processing^{46,52} due to its antiviral and antibacterial properties including activity against SARS-CoV-2.⁶⁸

6.3.3 Oxidized nucleosides

The susceptibility of nucleosides to oxidative stress is attributed to the reactivity of the nitrogen and oxygen atoms within the nucleobase.⁴⁰ Direct oxidation of nucleosides by ROS results in the formation of numerous oxidation products, some of which are illustrated in Figure 6. This chapter is limited to oxidized nucleosides reported in RNA unless otherwise stated. However, due to the structural similarity between DNA and RNA, it is likely that oxidation products found in DNA also occur in RNA.

Guanosine is the nucleoside most susceptible to oxidative stress due to its lowest redox potential among the four main nucleosides. The redox potential of guanosine E^0 (G) is 1.29 V, which is less than that of adenosine E^0 (A) = 1.42 V, cytidine E^0 (C) = 1.6 V and uridine E^0 (U) = 1.72 V.⁶⁹ Oxidation typically occurs at the C8 position of the purine heterocycle, leading to the formation of 8-oxoguanosine (oxo⁸G). This oxidized nucleoside was the first to be linked to oxidative stress and has since become a biomarker for elevated oxidative stress levels *in vivo*.^{37,38,44,45,47,50} Alternatively, oxidation at the C5 position results in ring opening and the formation of oxazolone (rZ), diiminoimidazole (rDiz), 5-carboxamido-5-formamido-2-iminohydantoin (r2Ih) and imidazolone (rIz) as shown in Figure 6.^{61,70} The redox potential of oxo⁸G is even lower than that of guanosine (E^0 (oxo⁸G) = 0.6 V)⁷¹ which leads to the formation of secondary oxidation products such as guanidinohydantoin (rGh) and spiroiminodihydantoin (rSp).^{61,70} The formation and stability of these compounds are highly dependent on a number of factors including the specific oxidant used, pH levels, oxidant concentration, and the presence of other substances such as reducing agents. This variability makes it challenging to draw definitive conclusions about their physiological relevance. The majority of these studies to date have focused on DNA, primarily investigating oxidation at nucleoside level.⁷²

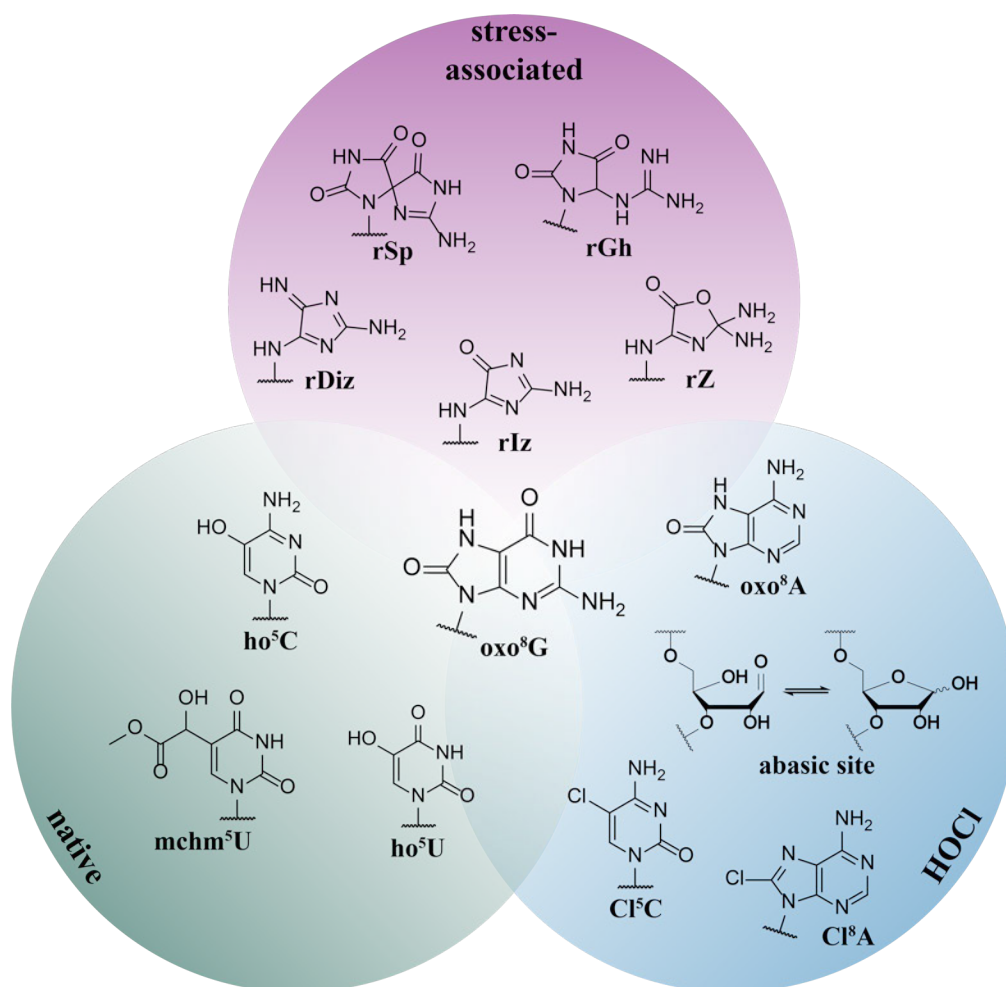


Figure 6. Oxidized nucleosides correlated with oxidative stress and cellular damage.

Important oxidation products derived from guanosine are 8-oxoguanosine (oxo⁸G), guanidinothymine (rGh), spiroiminodihydrothymine (rSp), diiminoimidazole (rDiz), imidazolone (rIz) and oxazolone (rZ), which are related to elevated levels of ROS. Other oxidized nucleosides include 8-oxoadenosine (oxo⁸A), 5-hydroxycytidine (ho⁵C), and the corresponding chlorinated derivatives (Cl⁸A) and (Cl⁵C). Abasic sites completely lack the nucleobase and display a prevalent oxidative lesion. Naturally occurring oxidized nucleosides are ho⁵C and uridine modifications such as 5-(carboxyhydroxymethyl)uridine methyl ester (mchm⁵U).

As observed with guanosine, oxidation at the C8 position of adenosine results in the formation of 8-oxoadenosine (oxo⁸A), which can undergo further oxidation reactions. Oxidation of oxo⁸A gives rise to an iminoquinone structure, which is highly sensitive towards nucleophilic attacks leading to C-C crosslinks as shown in Figure 7.⁶²

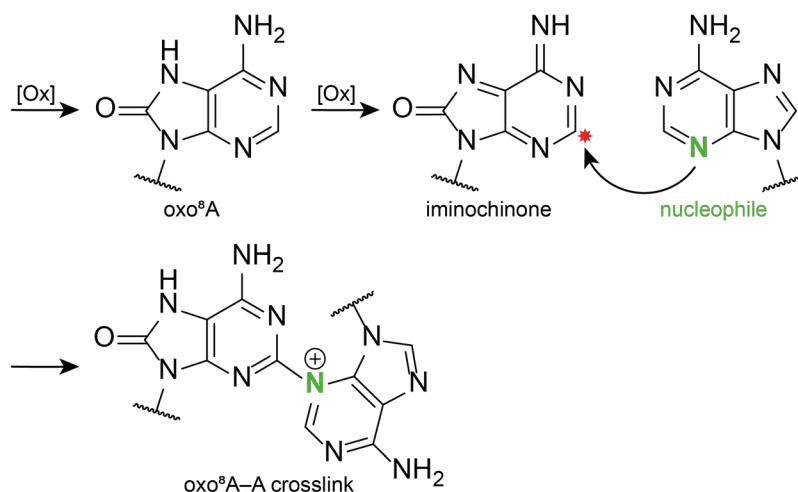


Figure 7. Mechanism for cross-link formation of oxidized adenosines.

Oxidation of adenosine results in the formation of oxo⁸A, which is susceptible to further oxidation generating an iminoquinone structure. This structure is highly reactive towards nucleophiles and capable of forming C-C crosslinks. Figure adapted from Nilov *et al.*⁶²

Minor oxidation products found in ribonucleosides include ring-opened structures derived from oxo⁸A such as formamidopyrimidines and derivatives thereof.^{37,62} 8-chloroadenosine has been reported in the context of the immune response and myeloperoxidase-derived HOCl^{57,60,67} as described in Chapter 6.3.2. Oxidation products of cytidine and uridine in RNA are 5-hydroxypyrimidines,^{42,65,73} while 5-chloropyrimidines have been identified in the context of HOCl oxidation,^{52,56,57} though detailed studies are lacking. In contrast, the occurrence of oxidation products in DNA is documented with greater frequency. Applied oxidants include hydroxyl radicals, γ -radiation⁷⁴⁻⁷⁷ and *in vivo* oxidized lesions.⁷⁸

The existing literature on oxidized nucleosides in RNA remains incomplete, with knowledge derived from diverse research fields, ranging from chemistry-based *in vitro* studies on nucleosides to clinical studies involving patient-derived samples. Consequently, the aforementioned summary must be critically analyzed before being utilized as the basis for experiments conducted during this PhD thesis.

6.3.4 Abasic sites in nucleic acids resulting from oxidative stress

Abasic sites, also known as apurinic/aprimidinic (AP) sites, are lesions found in nucleic acids resulting from oxidative stress among other causes.^{42,45,79} Hydrolysis at the anomeric carbon of the ribose releases either the nucleobase or its oxidized derivative creating an abasic site (see Figure 6). These sites are more frequently found at purine nucleosides due to the increased instability of the *N*-glycosidic bond, particularly following base modification or damage that leads to electron withdrawal. Abasic sites exist in equilibrium between a closed-ring hemiacetal and an open-ring aldehyde form. The aldehyde form is highly reactive towards nucleophiles, including amines and thiols, which are commonly found in cellular environments. Crosslinks between RNA and proteins can potentially form at abasic sites leading to the activation of stress response or cell death signaling pathways. If the crosslink occurs between the mRNA and the

ribosome, translation is stalled and the mRNA is degraded.^{79,80} In rRNA, abasic sites activate a proinflammatory signaling pathway resulting in either cell repair or apoptosis, a response known as the ribotoxic stress response.^{81,82} Beyond their recognition as damaged sites, abasic mRNAs also play a regulatory role during transcription if present in R-loops. These R-loops, formed by the single-stranded DNA template and the mRNA, are stabilized due to the presence of abasic sites in RNA, causing the polymerase to pause and thereby regulating gene transcription.^{79,83}

The reactivity of the aldehyde moiety in abasic sites can also be exploited for detection using aldehyde-reactive probes (ARPs). ARPs, typically hydroxylamine derivatives functionalized with a fluorescent dye or biotin, form a Schiff base upon reacting with the aldehyde.^{79,84,85} Following base removal, strand scission is facilitated in both RNA⁸⁶ and DNA via a β -elimination reaction, which can be induced by aniline in RNA and piperidine in DNA.^{87,88} This detection method has been successfully applied to both RNA and DNA.^{83,89} Additionally, several transcriptome-wide methods have employed the reactivity of abasic sites for mapping purposes in DNA⁹⁰⁻⁹⁴ although similar applications in RNA are yet to be developed.

6.4 Detection technologies for RNA modifications and integrity

The high variety of RNA modifications from a structural, chemical, and functional point of view, has led to the development of a wide field of detection technologies. These technologies primarily focus on one of these aspects. Two principal techniques are mass spectrometry (MS) and next-generation sequencing (NGS). While mass spectrometry enables the identification and quantification of the underlying nucleoside, sequencing methods allow the localization of modified residues within an RNA sequence. However, the sequence context is lost in the classical mass spectrometric approach, while only limited information about the underlying residue is achieved during sequencing.^{18,95-97} Consequently, the investigation of the epitranscriptome remains elusive unless multiple technologies are employed in parallel.

6.4.1 Conventional techniques to investigate RNA integrity

RNA is naturally susceptible to degradation due to its sensitivity to hydrolysis or oxidation. This is particularly relevant when considering the effects of oxidative stress, where regular checks on the integrity and quality of the RNA are essential for investigating its impact. Two conventional techniques are UV spectroscopy and polyacrylamide gel electrophoresis (PAGE). Both approaches rely on the presence of nucleobases, which either act as absorbing chromophores or serve as interaction partners for gel staining purposes. UV spectroscopy is a commonly employed technique in laboratory settings to quantify nucleic acids. This is achieved by measuring the absorbance at 260 nm, which provides indications of alterations in the nucleobase or contamination with salts or proteins. Alterations in the nucleobase are observed upon oxidation, as the addition of oxygen atoms or ring-opening changes the chromophoric

system and therefore alters the absorbance. These effects can be detected in kinetic set-ups allowing for the analysis of the reaction progress.⁹⁸⁻¹⁰⁰

PAGE separates RNA molecules according to their size, thus determining RNA integrity and visualizing potential degradation processes.¹⁰¹ Conventional staining techniques employ the intercalation of fluorescent dyes, such as GelRed,¹⁰² between stacked nucleobases. Alterations on the nucleobases potentially interfere with dye intercalation. In particular, abasic sites are incapable of any dye interactions, thereby completely inhibiting the staining and visualization process.^{55,102}

The combination of both methods provides a rapid and straightforward initial approach to investigating the impact of oxidative stress on RNA. It allows for the observation of expected reactions at the nucleobase, which may include the formation of abasic sites as well as damage to the phosphate backbone.

6.4.2 LC-MS/MS analysis of RNA nucleosides

Liquid chromatography coupled with mass spectrometry (LC-MS/MS) represents a highly sensitive and accurate method for the analysis of RNA modifications. This technique allows for the quantification of nucleoside amounts in femtomole ranges and the detection of hitherto unidentified nucleosides.^{103,104} One common approach for investigating RNA modifications via LC-MS/MS involves analyzing mononucleosides following enzymatic digestion. Initially, RNA is hydrolyzed into nucleotides using an endonuclease, such as nuclease P1, and a phosphodiesterase. This is followed by further hydrolysis into nucleosides by an alkaline phosphatase.^{95,105}

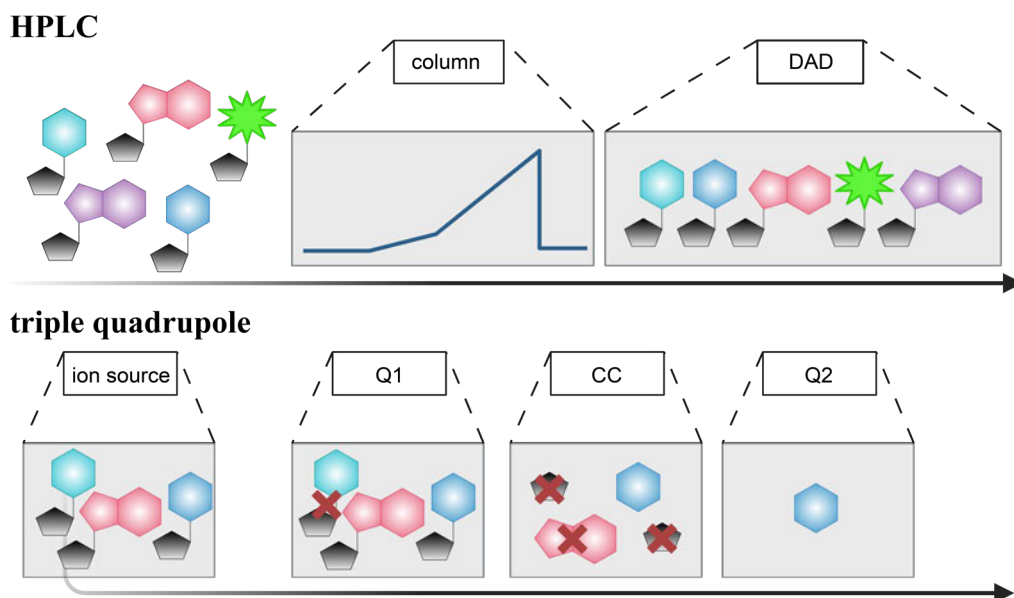


Figure 8. HPLC-MS/MS methodology employed for nucleoside analysis.

Digested nucleosides are separated on an RP-18 HPLC column using a binary gradient. Detection is performed via a diode array detector (DAD), which allows for parallel measurement at several wavelengths. The separated nucleosides are then subjected to the triple quadrupole (QQQ) mass spectrometer. First, nucleosides are ionized via electrospray ionization (ESI) and then transferred to the QQQ-MS, consisting of quadrupole 1 (Q1), the collision cell (CC), and quadrupole 2 (Q2). Selected ions with chosen mass-to-charge ratios are allowed to pass through Q1 before being fragmented in the CC. A

second selection step of the resulting fragments is performed in Q2, ensuring that only defined product ions reach the final detection via a high-energy dynode (HED) and an electron multiplier (EM). Created with Biorender.com (2024).

Figure 8 depicts the procedure of nucleoside analysis on an HPLC system with a triple quadrupole mass spectrometer (QQQ-MS). In the initial stage of the procedure, the digested nucleosides are subjected to HPLC separation on an RP-18 column and a binary mobile phase. The RP-18 column represents a hydrophobic stationary phase and the mobile phase typically consists of an aqueous buffer and an organic solvent.⁹⁵ A common composition of the mobile phase for nucleoside analysis is ammonium acetate with a buffer range of pH 4.75 ± 1 and pH 9.25 ± 1 ¹⁰⁶ and acetonitrile as the organic solvent. Essential parameters for chromatographic separation include the eluents, the ion strength, the pH, the applied gradient, the column temperature, and the flow rate.^{107,108} The examination of these parameters is of critical importance in enhancing the chromatographic performance of nucleosides. Following HPLC, the separated nucleosides are subjected to detection by a diode array detector (DAD), which allows for the simultaneous measurement of several wavelengths. Subsequently, the eluate enters the QQQ-MS system, which comprises the ion source, the ion optics including the capillary and the octopole, followed by the first quadrupole (Q1), the collision cell (CC), and the second quadrupole (Q2) before being detected via a high-energy dynode (HED) and an electron multiplier (EM). The analyte is ionized via electrospray ionization (ESI) and the surrounding liquid is evaporated during acceleration before the positively charged analytes (precursor ions) reach Q1. Q1 and Q2 are sequential mass filters that can be configured to permit only specific mass-to-charge ratios (m/z) to pass. Between Q1 and Q2 fragmentation is performed in the CC by collision between the precursor ions and an inert collision gas such as nitrogen. This process is designated as collision-induced dissociation (CID), and the resulting fragments are referred to as product ions.¹⁰⁹ The QQQ-MS offers a variety of analytical options, contingent upon the settings of Q1, CC, and Q2 in addition to the final detection.¹¹⁰ One such option is the MS2 scan, which detects precursor ions without any induced fragmentation. This allows for the identification of the m/z of unknown ions. The product ion scan employs defined m/z of known precursors and analyzes the full m/z range for the resulting product ions after fragmentation. The combination of both scan modes results in the identification of mass transitions for specific compounds applying defined MS settings. Prior knowledge of the mass transition is a prerequisite for performing analysis in the highly sensitive multiple reaction monitoring (MRM) mode, which is used for quantification purposes. This detection mode only detects specific mass transitions which are defined by the exact m/z of precursor ions in Q1 and their corresponding product ions in Q2. To further enhance the MS' sensitivity, a retention time window can be specified for every compound, which is then termed the dynamic MRM (dMRM) mode.^{103,104,110} An alternative approach is the implementation of a neutral loss scan (NLS), which scans for all compounds experiencing a mass loss of a distinct m/z . Ribonucleosides typically fragment at the *N*-glycosidic bond into a positively charged nucleobase and a neutral ribose molecule. This scan mode is employed when the objective is to detect ribonucleosides with unknown molecular masses.^{110,111}

In addition to the identification and detection of ribonucleosides, absolute quantification can be performed using LC-MS/MS, particularly in dMRM mode due to its high sensitivity.^{103,104} Calibration curves of external standards are utilized for linear regression, which is then used for the calculation of the absolute amount of the corresponding nucleoside. The limits of detection (LOD) of RNA modifications exhibit a wide range, spanning from the single-digit femtomole range to 10 fmol. This variability

is influenced by instrumental, sample, and physicochemical parameters including ionization and fragmentation efficiencies.^{104,112} The quantification of highly abundant nucleosides including uridine, cytidine, guanosine, and adenosine is typically conducted based on their UV signal. Additionally, their mass transitions are excluded from MS detection to prevent MS system saturation.^{103,104}

A comprehensive understanding of the underlying technology and the optimization of parameters for measurements is essential for the successful application of this technique. If the requisite conditions are met, LC-MS/MS analysis represents a highly sensitive methodology for the detection and quantification of RNA nucleosides and modifications.

6.4.3 Mapping of modified ribonucleosides through next-generation sequencing

Next-generation sequencing (NGS) is a widely used method for detecting and localizing RNA modifications within an RNA sequence. It is derived from Sanger sequencing which is based on the synthesis of truncated DNA fragments by stochastic incorporation of dideoxynucleotide triphosphates (ddNTPs) lacking the 3'-OH necessary for subsequent strand synthesis.¹¹³ The resulting truncated DNA fragments are analyzed by gel electrophoresis to separate them by size. The four ddNTPs are used in separate reaction mixtures resulting in four different truncation products at either T, G, A or C sites. Comparison of the resulting truncated DNA fragments on the gel allows identification of the respective nucleobase within the sequence.¹¹³⁻¹¹⁵ Modern NGS techniques (e.g. Illumina) use fluorescence detection during the synthesis of a complementary DNA strand to identify nucleic acid sequences. The DNA is immobilized on a surface and functionalized dNTPs, which are fluorescent and reversibly removable from the synthesized strand, are used to synthesize the complementary strand residue by residue. Fluorescence detection is performed after each cycle and the detected color, which is unique for each dNTP, indicates the corresponding residue.

Figure 9 illustrates the sequencing procedure of RNA via standard NGS. In the first step, the RNA must be prepared through a process known as library preparation. Library preparation (Figure 9A) involves the ligation of adapters for reverse transcription (RT) into cDNA, followed by polymerase chain reaction (PCR) amplification. In addition, short sequences referred to as barcodes are required for the identification of the resulting data during bioinformatic data analysis. Furthermore, NGS-specific sequences are necessary for immobilization on the so-called flow cell. Figure 9B depicts the reactions that occur during the sequencing process. Prior to the actual sequencing analysis, immobilization is performed by the hybridization of the aforementioned processed cDNA to the flow cell and synthesis initiation of a complementary strand at the immobilized and complementary Illumina primer sequence. Following the removal of the initial DNA strand, the newly synthesized complementary strand bends over and hybridizes once more to the flow cell, thereby allowing another round of complementary strand synthesis termed bridge amplification. This process is repeated several times resulting in the generation of clusters, which are essential for achieving sufficient fluorescent signal intensities during sequencing. Each nucleotide is functionalized with a fluorophore of a different color, which is detected after every cycle of nucleotide ligation to the strand. Consecutive signals obtained in each cycle are subsequently

processed during bioinformatic data analysis. This reveals the original sequence of the RNA.^{97,114}

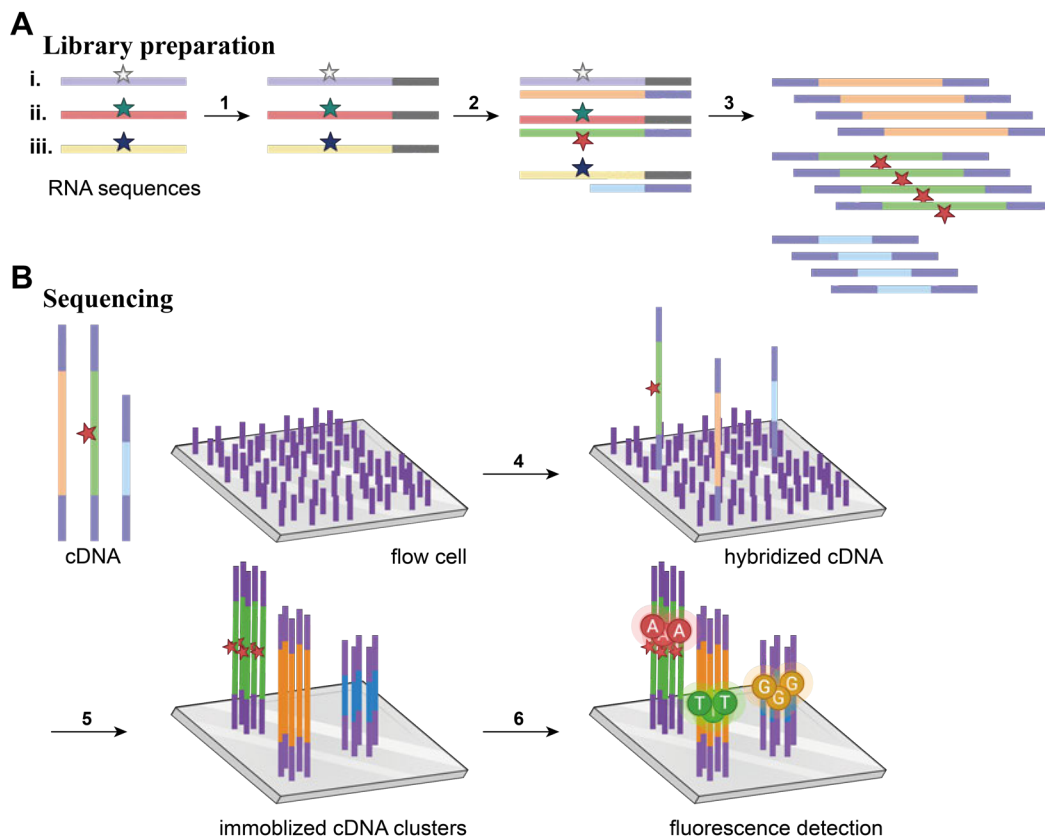


Figure 9. General NGS process via sequencing-by-synthesis.

A Library preparation of three differently modified RNA species (i., ii., iii.). The samples are derivatized by 3'- adapter ligation (1) before being reverse transcribed (2). Modified nucleosides show characteristic RT signatures in their cDNA: i. silent modifications are invisible; ii. mismatches appear as misincorporated nucleobases; iii. RT stops are abortive cDNAs. The resulting cDNA is adapter-ligated at its 5'-end and subsequently amplified via polymerase chain reaction (3). The final cDNA pool is termed sequencing library. **B** Sequencing-by-synthesis approach utilizing fluorescent dNTPs. The cDNA is loaded into a flow cell and hybridized to its surface (4). The amplification and downstream removal of the initial cDNA results in immobilized clusters of one clone (5). The read-out of the sequential addition of residues is performed via fluorescence. Each functionalized dNTP exhibits a distinct color enabling the localization of nucleosides within the sequence (6). Created with Biorender.com (2024).

The identification of RNA modifications is contingent upon the comparison with reference sequences or alternatively, the comparison of untreated vs. treated or wild-type vs. knock-out sequences. A comparison of the obtained sequences reveals differences at distinct positions. This discrepancy can be attributed to the initial cDNA synthesis during RT of the RNA, as modified nucleosides exhibit a distinctive base pairing pattern, commonly referred to as the RT signature (see Figure 9A).^{97,116} During reverse transcription, modified sites can result in mismatches, arrests, or deletions. A mismatch is defined as a base pair that differs from the classical Watson-Crick base pair (Figure 9A, ii.). Arrests are observed as RT stalls at modified sites, without any nucleotide being inserted (Figure 9A, iii.). In contrast, deletions result in the complete omission of the respective site, with the subsequent residue being incorporated directly.^{18,97,117} The knowledge of characteristic RT signatures for specific modified nucleosides allows for their identification during bioinformatic analysis. However, this approach necessitates the presence of a complete and characteristic RT signature induced by the modification itself in the generated cDNA. However, a substantial fraction of modified nucleosides is

RT silent, meaning that the correct nucleoside is inserted into the cDNA leaving the modification invisible during sequencing (see Figure 9A, i.). Consequently, a multitude of studies have been conducted to derivatize RNA modifications in a manner that would result in the RT signature being transformed into a selective and specific pattern, thereby enabling the identification of the modification.^{97,118,119}

These investigations can be achieved either enzymatically or chemically. One example of a chemical approach is the AlkAniline-Sequencing (AAS) protocol¹²⁰ developed by the █████ lab in Nancy, France. This approach relies on the site-specific cleavage of RNA molecules at 7-methylguanosine (m⁷G), 5-hydroxycytidine (ho⁵C), dihydrouridine (D) and 3-methylcytidine (m³C) sites, rather than on a characteristic RT signature.

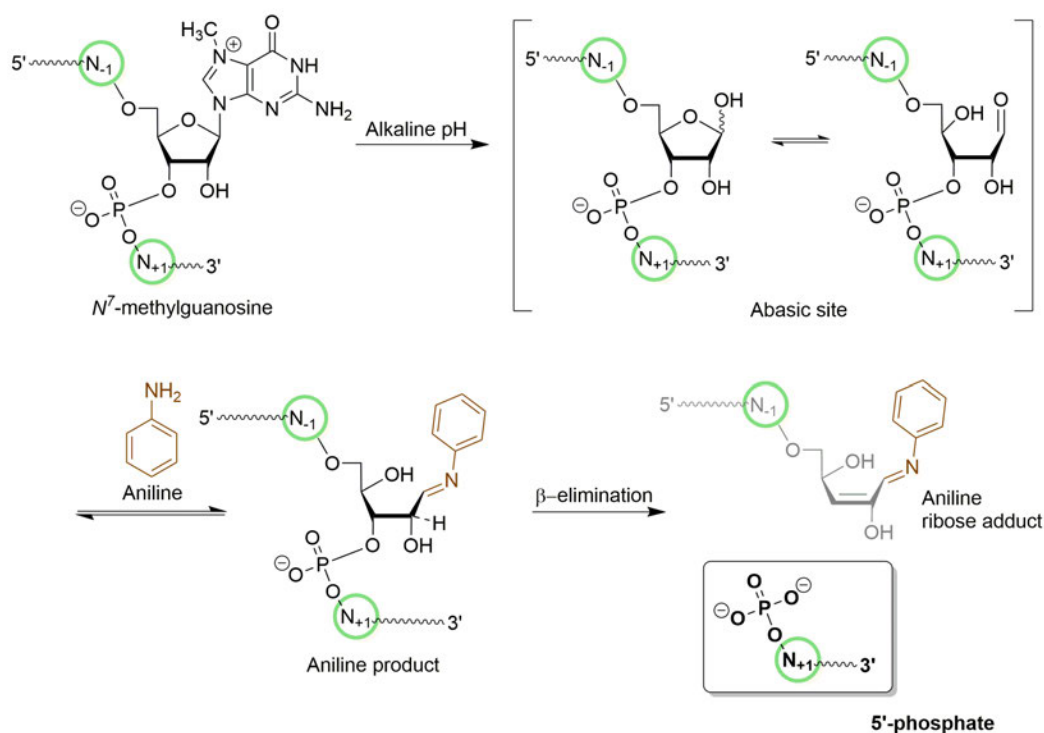


Figure 10. AlkAniline reaction scheme from Helm *et al.* 2021.¹²¹

Modified nucleosides such as m⁷G are susceptible to alkaline conditions, which initiate the removal of the nucleobase resulting in the formation of an abasic site. Abasic sites exist in an equilibrium, with the open-ring form possessing an aldehyde function. The aldehyde then reacts with amines such as aniline. The reaction of both partners results in the formation of a Schiff base which initiates strand cleavage under alkaline conditions via β-elimination. Strand cleavage occurs one nucleotide downstream of the modified site, resulting in the release of a new 5'-phosphate. Due to the complete initial removal of any natively present phosphates, only newly generated 5'-phosphates at the N+1 position of modified sites are available for adapter ligation during library preparation allowing their subsequent localization.^{117,122-125}

Figure 10 presents the reaction scheme of the AAS protocol. In the initial stage, alkaline hydrolysis induces the removal or derivatization of the nucleobases, thereby rendering the resulting product such as an abasic site, susceptible to strand cleavage. Abasic sites exist in an equilibrium between a closed-ring and an open-ring structure featuring an aldehyde group that is reactive towards amines such as aniline. The reaction of both partners results in the formation of a Schiff base which initiates strand cleavage under alkaline conditions via β-elimination. Strand cleavage occurs one nucleotide downstream of the modified site, resulting in the release of a new 5'-phosphate. Due to the complete initial removal of any natively present phosphates, only newly generated 5'-phosphates at the N+1 position of modified sites are available for adapter ligation during library preparation allowing their subsequent localization.^{117,122-125}

7 MOTIVATION AND OBJECTIVES

Ribonucleic acids (RNA) play a crucial role in a multitude of biochemical processes including protein synthesis and gene expression regulation. Moreover, RNA has emerged as a novel therapeutic system in recent years during the SARS-CoV-2 pandemic. Potential applications in other pathophysiological fields are currently under investigation. Furthermore, it has been demonstrated that damaged RNA is involved in the progression and development of diseases correlated to increased levels of oxidative stress.

Oxidative stress is a ubiquitous process in aerobic organisms and its impact on DNA has been the subject of extensive investigation. However, research on RNA remains limited. In light of this, this thesis sought to analyze oxidative stress at the molecular level in order to gain a detailed understanding of its effects on RNA.

The initial objective was to establish reliable and reproducible experimental conditions using the oxidizing agent hypochlorous acid. This would then permit the investigation of various targets including nucleosides, nucleotides, binary oligoribonucleotides, oligoribonucleotides comprising all four main nucleotides, and *in vitro* transcribed tRNA. To obtain comprehensive results, several analytical techniques were intended to be used including UV spectroscopy, gel electrophoresis, LC-MS/MS, and next-generation sequencing. While UV spectroscopy, gel electrophoresis, and LC-MS/MS were already applicable for these purposes, the sequencing approach was aimed to be established.

More precisely, the investigation of oxidized RNA was designed to identify and quantify the formed oxidation products and to analyze RNA integrity upon exposure to oxidizing conditions. LC-MS/MS analysis was primarily conceived for the purposes of identification and quantification, whereas gel electrophoresis was employed for the analysis of RNA integrity. With regard to the latter issue, the examination of abasic sites was also to be conducted through the use of fluorescent and radioactive labeling.

The AlkAniline-Sequencing approach was planned to be the basis for the sequencing protocol to be established, which aimed at the mapping of oxidized guanosine species including abasic sites.¹²⁰

8 RESULTS AND DISCUSSION

8.1 Hypochlorous acid – the oxidizing agent of choice

The significant role of oxidative stress and its impact on cellular function motivated us to investigate its effect on RNA. HOCl was chosen as the oxidant of our research due to its prominent role in oxidative stress *in vivo* and its ability to generate ROS – the most common oxidative species found in cells.^{34,46}

8.1.1 Quantification of free chlorine in HOCl

Regular quantification was essential to ensure constant quantities of oxidant measured as chlorine (Cl₂) equivalents based on the ISO norm “Water quality – Determination of free chlorine and total chlorine – Part 2: Colorimetric method using *N,N*-dialkyl-1,4-phenylenediamine, for routine control purposes” (EN ISO 7393-2:2017). This ISO standard provides an international outline for quantifying chlorine in water, using the absorption measurement of the pink-colored complex formed by oxidized “*N,N*-diethyl-1,4-phenylenediamine” (DPD). Depending on the procedure, different forms of chlorine are defined as “free chlorine”, “bound chlorine”, “total chlorine” or “chloramines”. For our purposes, the protocol for determining “free chlorine” was applicable and this term is used throughout this PhD thesis.

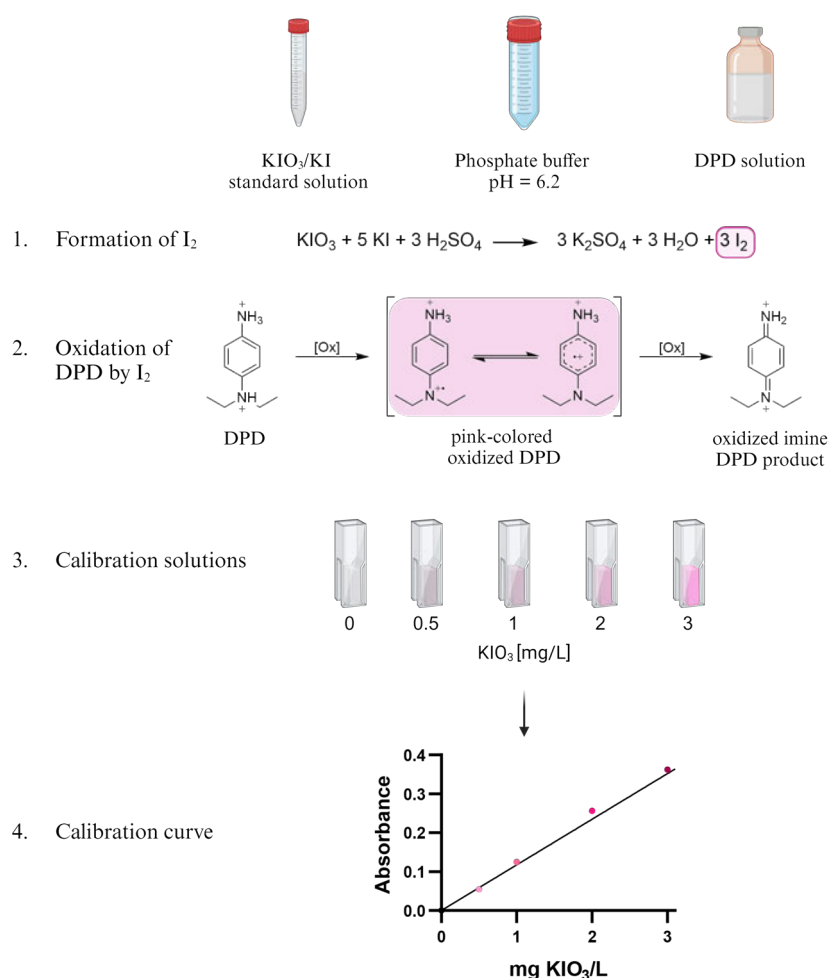


Figure 11. Quantification procedure of Cl_2 in HOCl using the DPD method.

Standard solutions with varying concentrations of KIO_3 are employed to generate a calibration curve. H_2SO_4 generates I_2 from KIO_3 and KI (step 1) which is responsible for the oxidation of DPD into its pink complex (step 2). At least five KIO_3 calibration solutions are measured via UV spectroscopy (step 3) and the resulting calibration curve (step 4) is used for the calculation of Cl_2 in HOCl. Created with Biorender.com (2024).

Figure 11 provides a schematic overview of the quantification procedure, which is based on the oxidation of DPD to a pink-colored complex, that can be measured photometrically. As the method demonstrated high sensitivity, solutions containing potassium iodate (KIO_3), sulfuric acid (H_2SO_4), and DPD were freshly prepared on the day of analysis using ultrapure water. Initially, a calibration curve was generated by using KIO_3 and potassium iodide (KI) solutions of at least five concentrations. The solutions were then oxidized by H_2SO_4 to form iodine I_2 as illustrated in Figure 11, step 1. The incubation period with H_2SO_4 was meticulously controlled to ensure a precise duration of one minute for each KIO_3 /KI concentration before terminating the reaction with a sodium hydroxide (NaOH) solution. I_2 acts as the active oxidant responsible for converting the colorless DPD to the pink-colored oxidized DPD (see step 2). The resulting absorbances were immediately measured at 515 nm using UV spectroscopy. The linear fit of the calibration curve was employed to determine the quantity of free chlorine present in HOCl (see step 4). For HOCl solution measurements, a dilution (approximately 1:5000) was prepared, supplemented with the DPD solution, and an immediate measurement was taken. It is important to note, that DPD can be further oxidized to a colorless imine derivative (see step 3). This is a crucial consideration, as high HOCl

concentrations in the measured samples can cause the pink color to disappear directly upon the addition of the DPD solution. Such a result can be misinterpreted as a failure of the DPD solution or inaccurately low Cl_2 concentrations.

8.1.2 The impact of pH and other compounds on the amount of free chlorine

The subsequent step involved evaluating the influences of pH and the presence of several compounds. The dilution of HOCl was conducted in 50 mM phosphate-buffered solutions with pH values of 6.4, 7.4, and 8.4, in comparison to unbuffered HOCl diluted in ultrapure water. As shown in Figure 12A, the quantity of free Cl_2 depended on the pH and decreased from 148 mM Cl_2 at pH 8.4, to 79 mM Cl_2 at pH 6.4, representing 47% of the unbuffered solution. Another constituent present in calibration and HOCl solutions is ethylenediaminetetraacetic acid (EDTA) to prevent interferences with copper (II) and iron cations.¹²⁶ Figure 12B presents the impact of EDTA on the determined Cl_2 concentration in diluted HOCl solutions. The results demonstrate that at EDTA concentrations between 0.0 g/L and 0.8 g/L, the Cl_2 amount decreased by approximately 40% relative to the control (0.0 g/L EDTA). Another crucial aspect of obtaining reliable results during experiments was ensuring the complete termination of oxidation reactions. In this context, several potential reducing agents were added to the diluted HOCl solution and subsequently quantified. Potential reducing agents included amines, such as Tris*HCl (pH 6.7), ammonium bicarbonate (NH_4HCO_3), ammonium acetate (NH_4OAc), sulfur-containing compounds, such as methionine, dithiothreitol (DTT), sodium thiosulfate ($\text{Na}_2\text{S}_2\text{O}_3$), β -mercaptoethanol, ammonium thiosulfate ($(\text{NH}_4)_2\text{S}_2\text{O}_3$), and potassium bicarbonate KHCO_3 . The results are depicted in Figure 12C, which shows the determined Cl_2 amount in relation to an unbuffered control, set at 100%. Complete quenching of HOCl was achieved by methionine (2), DTT (5), $\text{Na}_2\text{S}_2\text{O}_3$ (6), and $(\text{NH}_4)_2\text{S}_2\text{O}_3$ (10). The addition of Tris*HCl (pH 6.7, (3) in brown) led to a decrease in the Cl_2 content reaching 10.5%. β -mercaptoethanol (9) reached 5.1%, the ammonium salts NH_4HCO_3 (4 in pink) and NH_4OAc (8 in blue) reduced the “free Cl_2 ” to 48.8% and 63.4% respectively. The addition of KHCO_3 resulted in an increased quantity of 208.8% free Cl_2 .

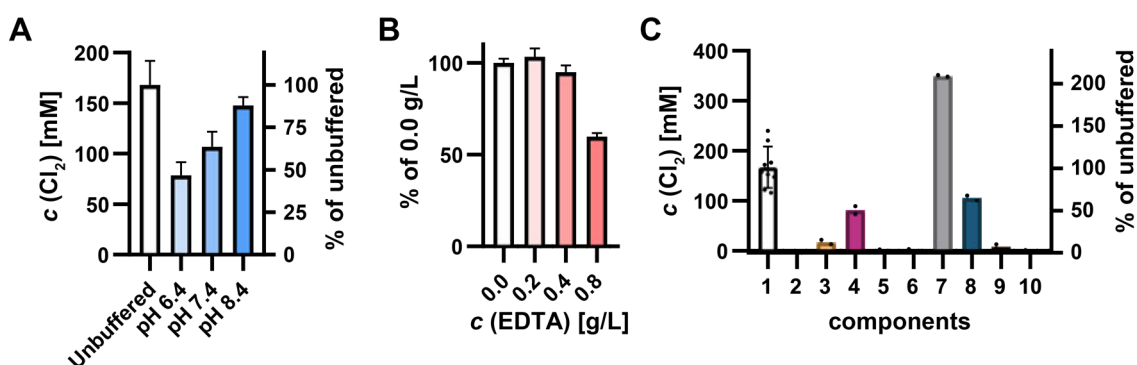


Figure 12. Influences of pH and selected compounds on detected Cl_2 amounts.

A The effect of pH in the phosphate buffer on Cl_2 concentration is indicated on the left y-axis. Quantification was performed at pH levels of 6.4, 7.4, and 8.4 compared to an unbuffered control. The Cl_2 content in the unbuffered control was set to 100% as indicated on the right y-axis. **B** The effect of EDTA in the determined Cl_2 amount was analyzed using 0.0 g/L, 0.2 g/L, 0.4 g/L and 0.8 g/L EDTA. **C** Evaluation of the effect of potential quenching agents such as amines and sulfur-containing components on Cl_2 concentrations: 1 unbuffered, 2 methionine, 3 Tris*HCl (pH 6.7), 4 NH_4HCO_3 , 5 DTT,

6 Na₂S₂O₃, 7 KHCO₃, 8 NH₄OAc, 9 β-mercaptoethanol, 10 (NH₄)₂S₂O₃. pH and EDTA experiments are indicated as mean values ($n = 3$) ± SD. Cl₂ quantification in the presence of potential quenching agents was performed in replicates ($n = 2$). Based on these careful evaluations, all experiments were conducted in a phosphate-buffered solution at pH 7.4. To ensure complete quenching, oxidation reactions were terminated by the addition of DTT to a final concentration of 10 mM. Quantification experiments were performed according to the ISO norm at pH 6.5 with the addition of 0.8 g/L EDTA.

Despite adherence to an ISO norm, a considerable amount of time was dedicated to quantification due to the unexpected limitations of the method's robustness. Experiments occasionally failed and required repetition, regardless of the thorough handling and care that was employed. In some instances, the concentration of Cl₂ was observed to increase over several weeks without any active alterations to the protocol. Potential confounding variables include fluctuations in laboratory temperature (approximately 10°C) and minor variations in solution concentrations. Significant effort was investigated in optimizing this procedure and identifying the most critical variables; however, definitive conclusions remained elusive. Consequently, it is important to note that the determined Cl₂ concentration may vary to some extent, potentially affecting the applied oxidation concentrations. Therefore, comparisons of experiments, particularly concerning the amount of oxidation products, should be interpreted with caution to some extent. The utilization of alternative quantitative methods, such as spectrometric techniques, as employed by other research groups, should be considered.^{57,127}

In contrast, HOCl is a highly effective bactericidal oxidant that is actively produced by immune cells during host defense. As a potent oxidant, HOCl generates reactive oxygen species (ROS), which are the primary mediators of oxidative stress *in vivo*. The potential damage caused by HOCl and ROS is a topic of significant interest, particularly in the context of imbalanced redox states which are characteristic of various diseases. Such conditions include neurodegenerative disorders, cancer, diabetes, and inflammatory conditions.^{34,46,52}

In recent times, several novel methodologies have been developed to analyze HOCl derived from the enzyme myeloperoxidase (MPO) under pathophysiological conditions in inflammatory diseases. These methodologies are designated to monitor and detect elevated inflammatory conditions, thereby facilitating early disease diagnosis.^{52,128,129} While these investigations are primarily conducted at the pathophysiological level, it is crucial to gain an understanding of the effects of HOCl on biomolecules, such as RNA, at the molecular level. This is necessary in order to estimate downstream consequences and expand our knowledge of oxidative stress *in vivo*.

8.2 LC-MS/MS analysis

8.2.1 LC-MS/MS method optimization for oxidized nucleosides

The optimization of nucleoside quantification by liquid chromatography-tandem mass spectrometry (LC-MS/MS) was conducted based on the previously described standard A method by Thüring *et al.* 2016.¹⁰³ The HPLC gradient consisted of acetonitrile (ACN) and 5 mM ammonium acetate (NH₄OAc) at a pH of 5.3. The concentration of ACN was initially increased to 8% over a period of 10 minutes, followed by an increase to 40% by minute 20, before being reduced to 0%. The mass spectrometer was configured to detect proton [M+H]⁺ and sodium [M+Na]⁺ adducts of oxidized nucleosides (as described in Chapter 10.2.15) using external standards where available. It was observed that chlorinated nucleosides preferentially form sodium adducts, with the mass-to-charge (m/z) ratio of [Cl⁵C+Na]⁺ being identical to that of [oxo⁸G+H]⁺ (see Figure 13A for structures and adducts of Cl⁵C and oxo⁸G). Figure 13B presents the MS signal of [Cl⁵C+H]⁺ ($m/z = 278$, shown in green) and [oxo⁸G+H]⁺ ($m/z = 300$, shown in pink) applying the standard nuc4 method. Both signals were observed at the same retention time, which is typically acceptable during dMRM mode detection when fragmentation patterns are distinct. However, as Cl⁵C not only ionizes with protons but also forms sodium adducts and the corresponding m/z [Cl⁵C+Na]⁺ = 300, differentiation was not possible.

Consequently, it was necessary to modify the previously applied HPLC method. To address this issue, the concentration of NH₄OAc was evaluated between 5 mM and 20 mM. Moreover, the initial duration of the gradient was extended, as the elution of Cl⁵C and oxo⁸G occurred within the first 10 minutes. Particularly, the separation of both compounds was enhanced by the addition of a prolonged period containing a high proportion of aqueous NH₄OAc buffer in the mobile phase. Figure 13C depicts the final gradient, which begins with an initial step of 100% buffer for 10 minutes, gradually increasing the ACN content to 10% by minute 30 and to 40% by minute 40. In conjunction with a concentration of NH₄OAc of 10 mM, the MS signal for m/z 278 eluted at 14.2 minutes, while the signal for m/z 300 appeared in two separate peaks at 14.2 and 16.6 minutes. This identified Cl⁵C at 14.2 minutes and oxo⁸G at 16.6 minutes, thereby increasing the retention time t_r difference from $\Delta t_r = 0$ minutes to $\Delta t_r = 1.8$ minutes.

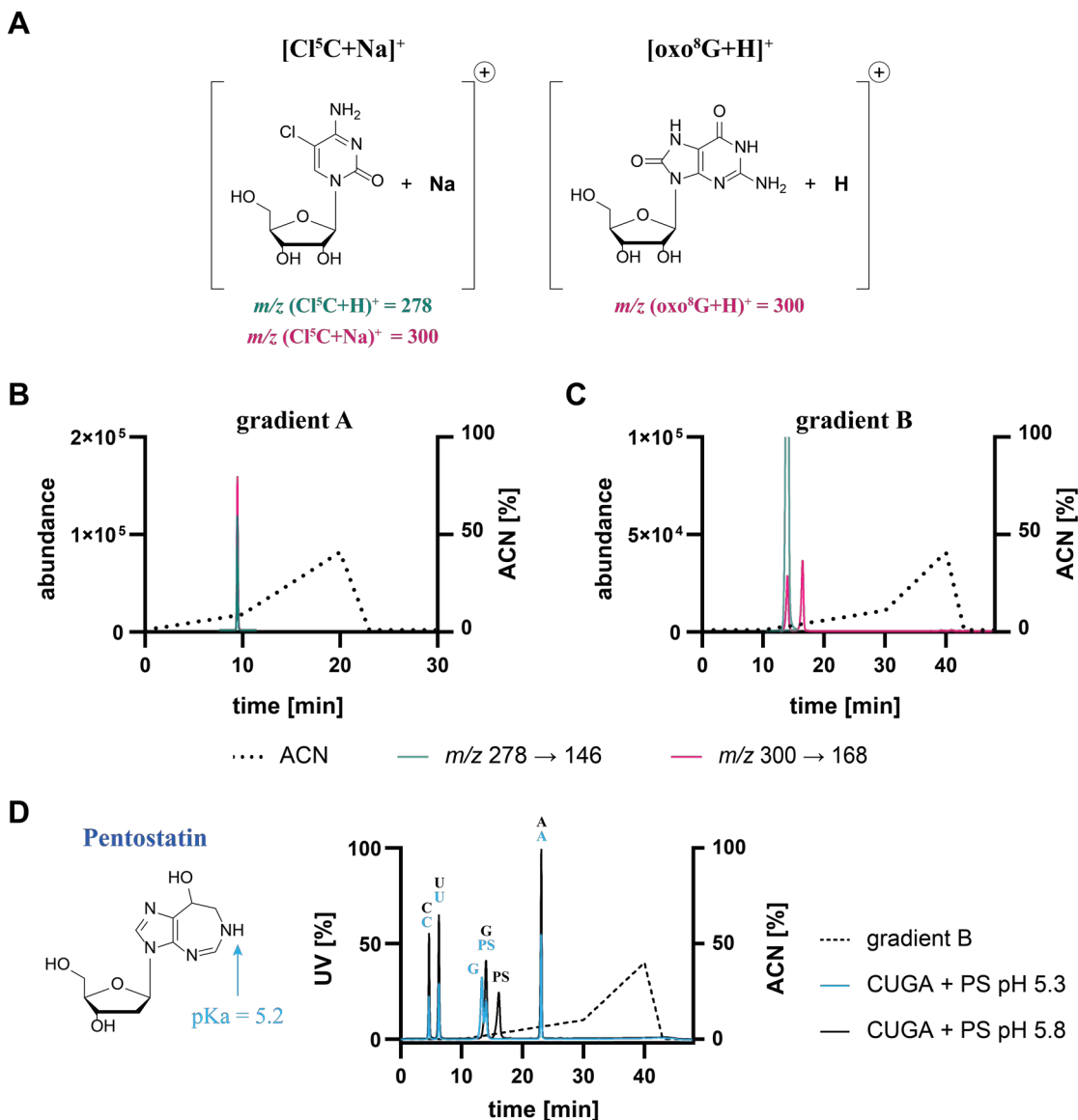


Figure 13. Optimization of HPLC-MS/MS method for oxidized nucleosides.

A Structures of 5-chlorocytidine (Cl⁵C) and 8-oxoguanosine (oxo⁸G) are shown with their preferential LC-MS/MS adduct: [Cl⁵C+Na]⁺ and [oxo⁸G+H]⁺, both resulting in $m/z = 300$. **B, C** Merged graphs displaying absolute MS abundances (left y-axis) and the proportion of acetonitrile (ACN) [%] on the right y-axis over time. MS signals for m/z 278 of [Cl⁵C+Na]⁺ are indicated in green and MS signals for m/z 300 are indicated in pink corresponding to [Cl⁵C+Na]⁺ and [oxo⁸G+H]⁺. **B** The standard ribonucleoside gradient A (dotted line) merged with the MS signals of m/z 278 (green) and m/z 300 (pink). The retention times were identical preventing differentiation between Cl⁵C and oxo⁸G. **C** The optimized gradient B for separating oxidized nucleosides. Retention times were 14.2 minutes for Cl⁵C and 16.6 minutes for oxo⁸G. **D** UV trace (shown as a relative signal [%] on the left y-axis) of main nucleosides supplemented with the deaminase inhibitor pentostatin (structure presented on the left). The optimized B gradient at pH 5.3 (blue) and 5.8 (black). Adjusting the pH value from 5.3 to 5.8 delayed the elution of pentostatin (PS) to 16.0 minutes allowing separation from guanosine (G) in black at pH 5.8) in the UV trace. Cytidine (C), uridine (U), and adenosine (A) are also indicated.

Furthermore, adjustments were implemented to differentiate guanosine from pentostatin (PS, Figure 13D) in the UV trace. Transferring the optimized gradient to oxidized samples revealed a coelution of PS with guanosine, which was visible in the UV trace. Figure 13D shows the optimized gradient B (dotted line) and the UV trace of the main nucleosides supplemented with PS eluted in NH₄OAc at pH 5.3 (blue) and at pH 5.8 (black). PS coeluted with guanosine at pH 5.3, which is visible in the UV signal and prevents absolute quantification. Given that PS has a pKa value of 5.2¹³⁰ increasing the

buffer pH to 5.8 allowed for the separation of both signals in the UV trace (see Figure 13D, black UV trace). The final settings for the LC-MS/MS analysis, including absolute quantification using external standards, were as follows: 10 mM NH₄OAc, pH 5.8, and a 54-minute gradient, termed gradient B.

In the context of investigating the impact of oxidative stress on nucleosides and RNA, LC-MS/MS represents a preferred method for qualitative and quantitative analysis. Given the high sensitivity of this technology, a preliminary examination of the procedure was conducted to ensure accurate measurements. Since oxidation products exhibit increased polarity compared to most other RNA modifications, our standard HPLC method proved unsuitable. It became evident that chlorinated nucleosides preferentially ionized as sodium adducts. Despite the exclusion of sodium-containing components from prior reactions and purification procedures and the incorporation of an additional desalting step, sodium could not be entirely removed from the sample. This resulted in a unique issue where two compounds exhibited identical retention times and mass transitions, rendering them indistinguishable in quantitative analysis. The most significant enhancement in the separation of Cl⁵C and oxo⁸G separation was achieved by extending the aqueous phase elution period from 0 to 10 minutes in the initial phase. Additionally, the increase of NH₄OAc concentration further improved their separation. The pH was adjusted from 5.2 to 5.7, which facilitated the separation of guanosine and pentostatin in the UV trace, a prerequisite for quantification based on UV signals. It should be noted that only these parameters were investigated; therefore, further optimization can be achieved by evaluating a wider range of conditions including the column temperature, ion source-specific parameters to enhance ionization efficiency, and flow rate.^{107,108} Subsequent analysis revealed that Cl⁵C was present in picomolar quantities, coeluting with guanosine in the UV trace. Consequently, further improvements are necessary.

8.2.2 Detection of ARP-labeled abasic sites via LC-MS/MS

This chapter describes the evaluation of the liquid chromatography-tandem mass spectrometry (LC-MS/MS) method for detecting the ARP-ribose product used in this thesis. For new molecules, where ionization and fragmentation patterns are unknown, it is crucial to identify these features to perform analysis in the dynamic multiple reaction monitoring (dMRM) mode of LC-MS/MS. This highly sensitive detection mode allows the analysis of very low abundance molecules, making it worthwhile to investigate MS settings and fragmentation behavior despite the time required.

Initial attempts to detect the ARP-ribose product in a mixture of oxidized and labeled RNA after digestion were unsuccessful. To address this, a control was synthesized according to Tanaka *et al.* 2011⁸⁵ by reacting ARP with ribose or ultrapure water. This was done to establish the detection of the ARP-ribose product via our LC-MS/MS system, in parallel with oxidized nucleosides. Figure 14A shows the reaction between ribose (1 in purple), which partially exists in an open-ring aldehyde form, and the ARP reagent (2), which contains nucleophilic hydroxylamine (orange) linked to a fluorescent Alexa Fluor™ 488 dye (green). Figure S2A shows a 20% denaturing PAGE analysis of the water-treated (ARP only, shown in gray) and ribose-treated ARP samples, revealing a second band that migrated slightly higher after a 3-hour run, indicating product formation. The fluorescence of the Alexa Fluor™ 488 dye linked to the ARP was utilized for scanning after gel electrophoresis and for detection during LC-MS measurements. The instrument's diode array detector (DAD) permitted the simultaneous scanning of several

wavelengths, thereby enabling the detection of nucleosides at 254 nm as well as of the fluorescent dye at 488 nm. Figure 14B depicts the UV trace at 488 nm over a 30-minute gradient for both water-treated (ARP only, shown in gray) and ribose-treated ARP (ARP + ribose, shown in pink), with the chromatogram zoomed in to highlight differences in absorbance at minute 12. Initially, an MS2 scan was performed to identify precursor ions after ionization following HPLC separation. This measuring mode allows the analysis of charge and adduct formation in the source compartment to identify the precursor ions. A fragmentor voltage of 80 V allowed the detection of both molecules, resulting in mass-to-charge (m/z) ratios of m/z (2) = 692 and m/z (3) = 824, indicating monoprotonated adduct formation upon ionization. Figures 14C and 14D illustrate the UV signal at 488 nm (pink) next to the detected precursor ions (m/z (2) = 692 in blue and m/z (3) = 824 in green) of the ARP only (Figure 14C) sample and the ARP + ribose sample (Figure 14D). The MS signals were detected 0.1 minutes after the UV detection due to the sequential reach of both detectors. While the m/z 692 signal was detected in both samples, the m/z 824 signal was only present in the ARP + ribose sample indicating successful product formation and confirming the ability to differentiate the ARP from the ARP-ribose product.

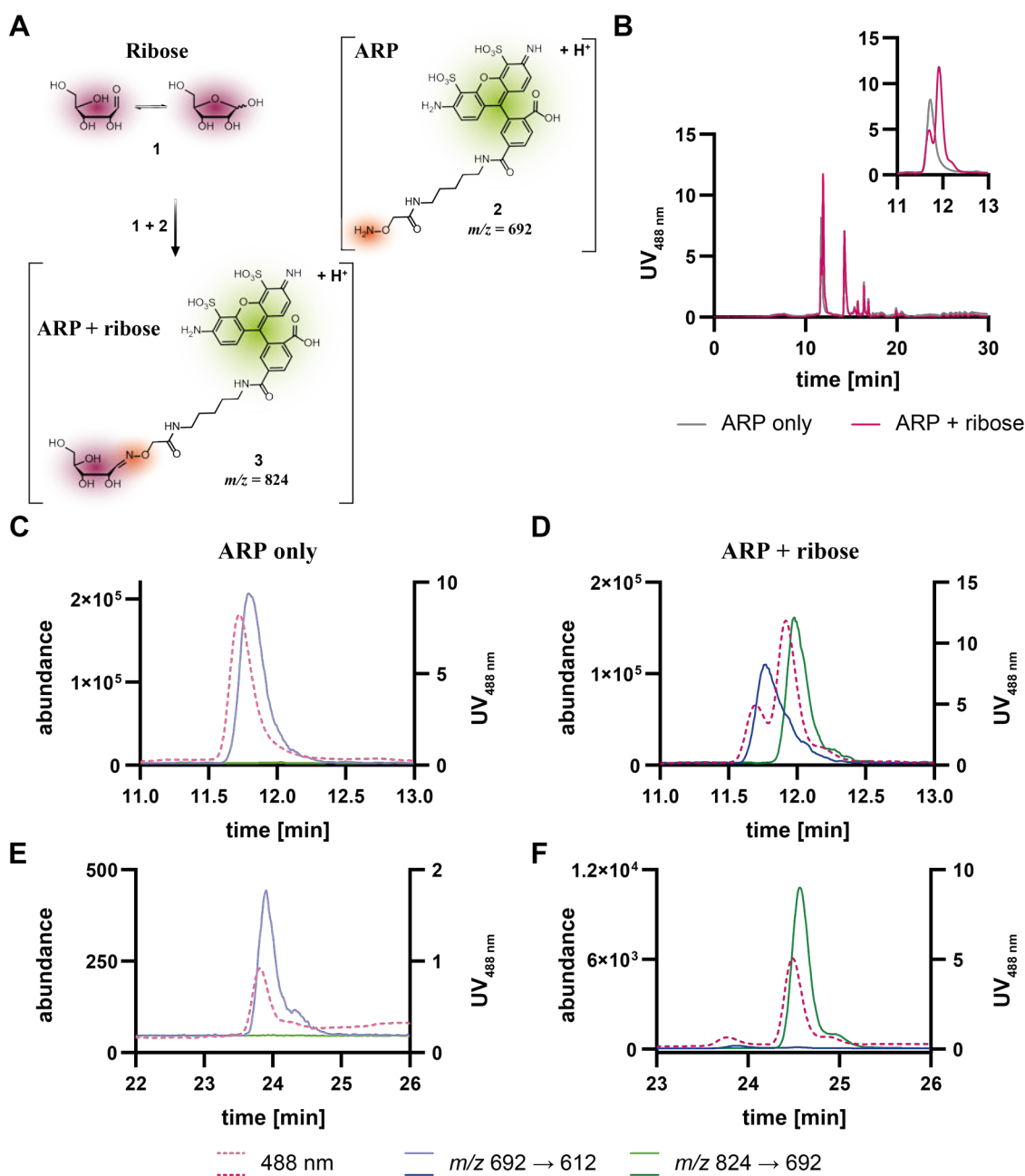


Figure 14. LC-MS/MS method evaluation of the ARP-ribose product.

A The ribose (1, shown in purple) exists in equilibrium between a closed-ring and an open-ring form containing an aldehyde moiety. This aldehyde reacts with nucleophiles such as hydroxylamines. The ARP reagent (2) includes a hydroxylamine group (highlighted in orange) and a fluorescent Alexa Fluor™ 488 dye. The reaction between 1 and 2 results in a Schiff base and the attached fluorescent dye allows detection at 488 nm. The resulting ARP-ribose product (3) is detectable via LC-MS with m/z (3) = 824. **B** UV traces at 488 nm of the ARP reagent alone in gray and the ARP+ribose sample in pink over a 30-minute gradient. The zoomed-in chromatogram highlights differences at 12 minutes. **C, D** Chromatograms of the MS2 scans for the ARP only (C) and the ARP+ribose sample (D). The UV signal at 488 nm is indicated in pink, the MS signal corresponding to the ARP only is shown in blue and the MS signal corresponding to ARP+ribose in green. **E, F** Final MRM analysis measuring the identified mass transitions of m/z (ARP only) = 692 → 612 and m/z (ARP+ribose) = 824 → 692. The UV signal at 488 nm is indicated in pink.

A product ion scan was then performed to identify the fragmentation characteristics of the two ARP molecules (2 and 3). This method detects all ions resulting from the fragmentation of specific precursor ions. For ARP detection, the first quadrupole was set to pass the previously identified precursor ions with m/z (2) = 692 and m/z (3) = 824

corresponding to ARP only and ARP-ribose, respectively. Using mild fragmentation settings (collision energy = 20 eV) in the collision cell, both molecules were characterized as monoprotonated adducts in the third quadrupole with the following fragmentation patterns of m/z (2) = 692 \rightarrow 612 and m/z (3) = 824 \rightarrow 692. These mass transitions were then used in a multiple reaction monitoring (MRM) mode using the adapted gradient B for oxidized nucleosides as described in Chapter 8.2.1 to identify the corresponding retention times. The resulting chromatograms displayed in Figures 14E and 14F showed a retention time of 23.9 minutes for the m/z (2) = 692 \rightarrow 612 transition and 24.6 minutes for m/z (3) = 824 \rightarrow 692 corresponding to the ARP-ribose product. These settings were then employed to analyze abasic sites in RNA after ARP labeling in dMRM mode.

The initial attempts to detect the ARP-ribose product using our standard LC-MS protocol proved challenging. However, the synthesis of a control sample based on the procedure described by Tanaka *et al.*⁸⁵ allowed a systematic investigation of the compound's MS properties. Utilizing various detection modes of the instrument facilitated the step-by-step identification of the correct MS signals and fragmentation patterns. In particular, the fluorescence of the dye detected at 488 nm of the ARP-ribose product significantly simplified its identification. The absence of precursor ion detection at the initial stage was attributed to in-source fragmentation. The original fragmentation voltage was set to 135 V, as previously employed for nucleosides. However, no conclusive signals were observed, and only a reduction to 80 V resulted in detectable signals corresponding to the proton, sodium, and potassium adducts of a monocharged ion.

Ultimately, the analysis of the ARP-ribose product within oxidized and labeled RNA samples was successful. This experiment will be further discussed in Chapter 8.4.2 which focuses on binary oligonucleotides.

8.3 Oxidation of ribonucleosides

To achieve a comprehensive understanding of the impact of HOCl oxidation, investigations were undertaken across various molecular substrates including nucleosides, nucleotides, binary oligoribonucleotides, oligoribonucleotides featuring all four main nucleotides, *in vitro* transcribed tRNA and total RNA extracted from *Saccharomyces cerevisiae*. The objective was to assess oxidation effects at the nucleoside level discriminating resultant products and potential interferences between nucleosides within a given sequence of small synthetic oligonucleotides and native RNA under diverse conditions.

Initially, the focus was on the oxidation of individual nucleosides - uridine (U, Figure 15), cytidine (C, Figure 16), adenosine (A, Figure 17), and guanosine (G, Figure 19) - to elucidate fundamental oxidative mechanisms devoid of other impacting factors. UV and LC-MS analyses were conducted across a range of Cl₂ concentrations (0 - 500 μM) applying stringent experimental protocols to minimize affecting variables given the sensitivity of Cl₂ to various components and conditions (as detailed in Chapter 8.1.2). Final oxidation experiments were performed as described in the methods section (10.2.8), excluding sodium to prevent preferential sodium adduct formation during LC-MS measurements. Additionally, MgCl₂ was included in the reaction mixture to mimic conditions akin to folded RNA experiments.

8.3.1 Pyrimidine oxidation

HOCl oxidation selectively modifies nucleosides favoring C5 in pyrimidines and C8 in purines.^{46,52} Figure 15A depicts the resulting oxidation products for uridine: 5-hydroxyuridine (ho⁵U, light blue) and 5-chlorouridine (Cl⁵U, dark blue) focused during this study. In a first approach, oxidation reactions on nucleosides were monitored via UV analysis to evaluate reaction kinetics and the impact of oxidation on their chromophore over time. Typically, nucleosides exhibit a peak absorbance at 260 nm as demonstrated by uridine. Spectral comparison of oxidized uridine showed minor changes (see Figure 15B) across Cl₂ concentrations ranging from 0 (gray) to 500 μM (black) compared to cytidine, adenosine, and guanosine described in the following chapter. The maximum absorbances remained constant at $\lambda_{max} = 262$ nm demonstrating a slight hypochromic shift from 0.40 to 0.31 without altering λ_{max} , suggesting modest impacts of HOCl on the chromophore (see also Figure S3A). Reference spectra of external standards for ho⁵U and Cl⁵U are shown in Figure S4A.

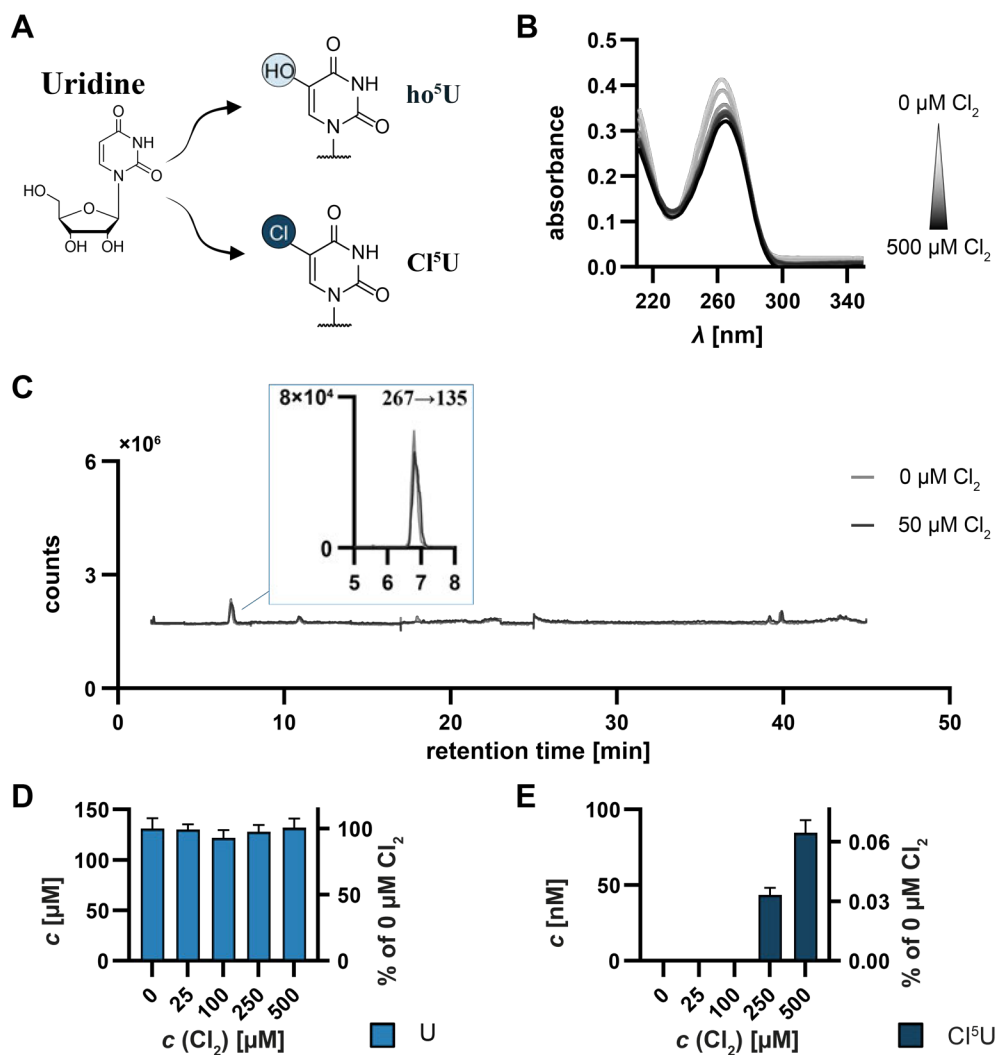


Figure 15. Oxidation on uridine revealed only minor changes analyzed via UV and LC-MS.

A Molecular structures of major oxidation products: 5-hydroxyuridine (ho⁵U) and 5-chlorouridine (Cl⁵U). **B** Absorbance spectra of 100 μM U oxidized from 0 to 500 μM Cl₂ were recorded after incubation for 10 minutes from 200 to 350 nm. **C** Total ion chromatograms of a neutral loss scan (NLS) detecting mass transitions of *m/z* 132 corresponding to a ribose moiety. Chromatograms display counts against the retention time of 50 pmol injected untreated U (gray) and 50 μM Cl₂-treated U (dark gray). The inset illustrates the extracted ion chromatogram (EIC) of *m/z* 267 corresponding to the sodium adduct of uridine [U+Na]⁺. **D**, **E** Absolute quantification of U (37.5 pmol injected) and its oxidation products was performed by applying external calibration of nucleoside standards. Abundances are depicted as mean ± SD, *n* = 3. Panel **D** displays the amount of U in μM (left y-axis) and quantities relative to initial reaction concentrations (right y-axis) for 0, 25, 100, 250, and 500 μM Cl₂. **E** shows the amount of Cl⁵U in nM, ho⁵U was not detectable.

To further investigate generated oxidation products, a neutral loss scan¹¹¹ (NLS) was conducted comparing untreated uridine with uridine treated with 50 μM Cl₂ following the standard oxidation procedure omitting the final quenching step. During the NLS, all molecules experiencing a mass loss of 132 corresponding to the ribose moiety were detected while excluding the mass transition of the protonated uridine (mass-to-charge *m/z* = 245) to prevent MS system saturation. In Figure 15C, the total ion chromatogram represents MS counts (y-axis) plotted against the time of untreated (gray) and treated (dark gray) uridine. Apart from the sodium adduct of uridine at a retention time *t_r* of 6.8 minutes, *m/z* = 267 (as illustrated in the Figure 15C inset), no other signals were observed as well as in the DTT-quenched sample (Figure S5A). It is noteworthy, that only those compounds that exhibited a sufficient ionization efficiency were detected,

indicating that other oxidation products may have been formed but were not observed during the analysis.

Based on these results, quantification of ho⁵U and Cl⁵U was performed using commercially available external standards for calibration purposes in a dynamic multiple reaction monitoring (dMRM) mode enabling the detection of selected mass transitions in a specific retention time window corresponding to targeted nucleosides, thereby increasing the MS' sensitivity.¹⁰⁴ Absolute quantities of oxidized nucleosides were determined by external calibration in the range of 1 fmol to 5000 fmol in the MS, while main nucleosides were quantified by measuring the UV area detected by the diode array detector (DAD) installed after HPLC separation. For each experimental condition, 37.5 pmol of nucleoside was injected without further purification. Quantification revealed that uridine stayed unaffected with its quantity remaining constant even up to 500 μM Cl₂ (Figure 15D) under applied conditions. The primary oxidation product, Cl⁵U was only detectable in low femtomolar ranges at high Cl₂ concentrations (250 and 500 μM) resulting in < 0.1% of the untreated control, while ho⁵U was undetectable (Figure 15E). Notably, the detection limits of uridine nucleosides were relatively high compared to other modifications (ho⁵U = 10 fmol, Cl⁵U = 50 fmol). LC-MS analysis of uridine and its oxidation products was also performed on UMP showing similar quantities and presented in Figure S6A. Overall, UV and LC-MS analysis indicated the robustness of uridine against HOCl oxidation characterized by changes in absorption and low abundances of oxidation products even at over-stoichiometric ratios up to 1:5 (U : Cl₂). This observation is consistent with uridine's redox potential $E^0(\text{U}) = 1.7 \text{ V}$ ⁶⁹ which is lower compared to that of HOCl ($E^0 = 1.9 \text{ V}$) and supports earlier reports suggesting uridine as the least sensitive nucleoside to oxidation.^{57,58}

Comparison of the spectra of cytidine with uridine revealed a heightened susceptibility to oxidation consistent with their redox potentials ($E^0(\text{U}) = 1.7 \text{ V}$ vs. $E^0(\text{C}) = 1.6 \text{ V}$).⁶⁹ Absorbances at 270 nm decreased from 0.33 (0 μM Cl₂, gray) to 0.11 (500 μM Cl₂, black) accompanied by a noticeable bathochromic shift (Figure 16B) as supported by kinetic UV analysis at 300 nm (Figure S3B). The emergence of absorbance maxima at higher wavelengths indicates the presence of enlarged chromophores following especially oxygenation, but also chlorination of pyrimidines at C5 resulting in the formation of 5-hydroxycytidine (ho⁵C) and 5-chlorocytidine (Cl⁵C) upon HOCl oxidation (Figure 16A). Reference spectra are additionally shown in Figure S4B displaying maximum absorbances of Cl⁵C and ho⁵C at higher wavelengths. Oxidation products were identified and quantified using LC-MS/MS as described for uridine. Our targeted approach using an NLS detected three major signals eluting at 15.5, 17.0, and 21.6 minutes as depicted in the total ion chromatogram of untreated (gray) and 50 μM Cl₂ oxidized (black) cytidine (Figure 16C). The signals at 15.5 minutes and 21.6 minutes exhibited a mass-to-charge (m/z) ratio of 278 corresponding to monochlorinated cytidines (left inset in Figure 16C). Cl⁵C was identified at 15.5 minutes through comparison with external standards, while the second signal at 21.6 min potentially corresponded to an *N*-chloramine. The third peak (m/z 312) at 17.0 minutes (right inset in Figure 16C) was potentially assigned to a dichlorinated product based on the mass difference ($\Delta m/z = 68$) which corresponds to two chlorine atoms and the characteristic chlorine isotope pattern. A respective NLS of DTT-quenched cytidine (Figure S5B) showed only one major signal at 15.5 minutes matching the elution time and mass transition of the Cl⁵C standard highlighting the susceptibility of HOCl oxidation reactions to changes in experimental conditions as the other two products were not stable upon addition of the reductant DTT.

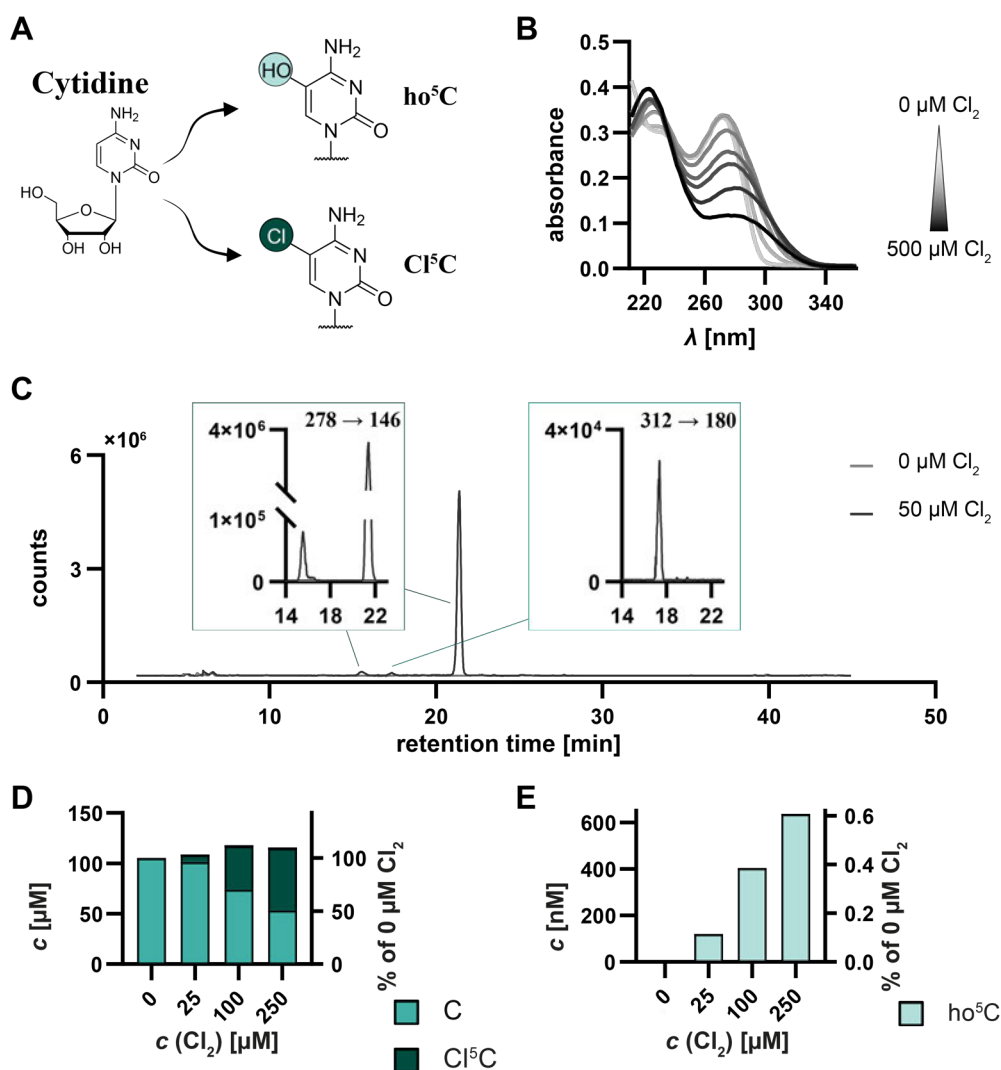


Figure 16. Cytidine oxidation results in the quantitative formation of 5-chlorocytidine (Cl⁵C).

A Molecular structures of primary oxidation products, 5-hydroxycytidine (ho⁵C) and Cl⁵C. **B** Absorbance spectra from 200 to 350 nm of 100 μM cytidine oxidized with varying concentrations of Cl₂ (0 to 500 μM) after a 10-minute incubation period. Increasing concentrations of oxidant resulted in concurrent hypochromic and bathochromic shifts. **C** NLS analysis comparing untreated cytidine (gray) with cytidine oxidized by 50 μM Cl₂ (green). Total ion chromatograms plotted against time revealed distinct peaks. Insets exhibit extracted ion chromatograms at *m/z* 278 → 146 and *m/z* 312 → 180, identifying two signals for *m/z* 278 corresponding to monochlorinated oxidation products, with retention times of 15.5 and 21.6 minutes and to a dichlorinated one at 17.0 minutes. Comparison with external standards confirmed the peak at 15.5 min as Cl⁵C whereas the identity of the other two signals was not further investigated. **D, E** Quantification of cytidine (37.5 pmol injected) and its oxidation products represented as the mean of two experimental replicates. Panel **D** presents the amounts of cytidine and Cl⁵C in pmol/μL (left y-axis) and the relative amount towards present cytidine in 0 μM Cl₂ on the right y-axis. Cl⁵C was generated at the expense of cytidine with the total of both equating to 100% of cytidine present in 0 μM Cl₂ control. **E** The formation of ho⁵C was limited to 0.6% under applied conditions in a femtomolar range.

Absolute quantification mirroring the methodology applied to uridine relied on commercial external standards and calibration curves spanning from 0 to 5000 fmol (with LOD of ho⁵C = 1 fmol, Cl⁵C = 5 fmol) for oxidation products detected via the MS system and 1 - 500 pmol of the parent nucleoside detected via UV. Cytidine underwent partial consumption at 25 μM Cl₂ diminishing to 50% of the initially present cytidine at 250 μM Cl₂ (Figure 16D). Simultaneously, the primary oxidation product Cl⁵C was generated to a comparable extent, such that the combined amount of cytidine and Cl⁵C constituted 100% of the initially present nucleoside excluding the formation of alternative oxidation products or undetected mechanisms in a relevant manner (Figure

16D). 5-hydroxycytidine was detected only in femtomolar traces comprising less than 0.1% of the untreated control (Figure 16E). Oxidation reactions and analysis by UV and LC-MS was also conducted on CMP resulting in similar showing similar quantities (Figure S6B).

HOCl-induced oxidation of nucleosides can lead to direct chlorination or oxidation by reactive oxygen species (ROS) of the nucleobase. Particularly, pyrimidines react at C5 resulting in 5-chloro- or 5-hydroxy- derivatives or get chlorinated at the exocyclic amine group of cytidine.^{52,65} Previous studies demonstrated that the chloramine product of cytidine is unstable and can act as a chlorine donor itself. Among the chlorination products of uridine and cytidine, only Cl⁵C was detected in both *in vivo* and *in vitro* experiments using the physiological enzyme myeloperoxidase (MPO), suggesting a lack of stability of alternative oxidation products⁵² also observed during our NLS analysis comparing unquenched and DTT-quenched cytidine. Other studies reported dichlorinated products for uridine¹³¹ at high HOCl to uridine ratios (5:1) as well as for cytidine and a mixed chlorinated-oxygenated cytidine derivative.¹³² Under applied conditions omitting DTT quenching only the dichlorinated cytidine was detected during this work. Another corroborative observation stems from the redox potential E^0 of nucleosides in the order of E^0 (U) = 1.7 V > E^0 (C) = 1.6 V > E^0 (A) = 1.4 V > E^0 (G) = 1.3 V.⁶⁹ The redox potential of HOCl and its base OCl⁻ is 1.48 V and 0.9 V, respectively, offering a potential explanation for the differences between uridine and cytidine.⁴⁶ This difference results in the abundances of cytidine oxidation products reaching approximately 50% of initial cytidine whereas uridine oxidation products only reached less than 0.1%.

LC-MS/MS analysis necessitates a sufficient ionization efficiency for mass spectrometric measurements, which is unknown for compounds where no external standard is available. This implies that other oxidation products may have been formed but not detected. Given the quantity of parent nucleosides, the formation of other oxidized nucleosides than Cl⁵C is unlikely. However, the possibility of low-abundance oxidation products still remains.

Prütz *et al.*¹⁰⁰ examined pyrimidine monophosphates upon reaction with HOCl, primarily via UV absorbances, consistent with the findings of this work showing increasing absorbances at 230 and 290 nm for CMP and identical, albeit weaker effects for UMP. Upon addition of the reductant GSH, the reaction was reversed in the case of UMP, whereas only the *N*-chloramine disappeared in oxidized CMP leaving the 5-chloro-substituted CMP as the sole product. It was demonstrated that the presence of reducing agents as GSH or DTT alters reaction products with the disappearance of the *N*-chloramine and reversal of detected UV absorbance changes. While a change in reaction outcome depending on the presence of reductants was also observed in LC-MS analysis during this PhD project, analysis via UV was not conducted.

In summary, the oxidation of pyrimidines by HOCl displayed varying efficiencies, with uridine exhibiting relatively low reactivity compared to cytidine which underwent quantitative oxidation to Cl⁵C. Furthermore, these findings underscore the sensitivity of oxidation reactions to reaction conditions, highlighting the potential for significant alterations in the composition of generated oxidation products.

8.3.2 Oxidation of adenosine

Purines are known to exhibit heightened sensitivity to oxidation due to their lower redox potential compared to pyrimidines: uridine > cytidine > adenosine > guanosine.⁶⁹ Primary oxidation predominantly targets the C8 position leading to the formation of 8-oxo- and 8-chloro- derivatives as illustrated in Figure 17A for adenosine (oxo⁸A in light orange and Cl⁸A in red).

Adenosine oxidation experiments as conducted on uridine and cytidine revealed substantial hypochromic changes at 260 nm (Figure 17B) with absorbances dropping from 0.53 (0 μ M Cl₂ in light gray) to 0.14 (500 μ M Cl₂ in black) suggesting nucleoside consumption. Additionally, absorbances at wavelengths greater than 300 nm increased for oxidant concentrations exceeding 50 μ M Cl₂, discernible after subtracting the corresponding HOCl-treated buffer controls (see Figure S3C). Figure S4C shows UV spectra of commercial standard nucleosides: oxo⁸A and Cl⁸A indicating alternative oxidation mechanisms beyond the formation of C8 oxidation products as the reference spectra notably differ from those of the oxidized samples. Similar to uridine and cytidine, an NLS analysis was conducted detecting signals exhibiting a loss of mass of 132 corresponding to a ribose moiety for 50 μ M Cl₂-treated adenosine compared to untreated control. Figure 17C illustrates absolute counts plotted against time revealing additional signals in oxidized adenosine (black) such as those at 13.3 minutes, 28.6 minutes, and 33.4 minutes (see insets) compared to untreated control (light gray). The signal at 13.3 minutes corresponds to inosine (I), the deamination product of adenosine with m/z 269, confirmed by comparison with an external standard. As inosine was not a primary focus of this study, quantification was only performed at later stages utilizing data obtained from an NLS (Figure S10). Cl⁸A manifested as a minor peak at 33.4 minutes (m/z 302), respectively. Unlike the other nucleosides, adenosine was the only one yielding oxidation products with mass-to-charge values greater than 420, potentially corresponding to dimers as exemplified by the peak eluting at 28.6 minutes (m/z 519) shown in Figure 17C.

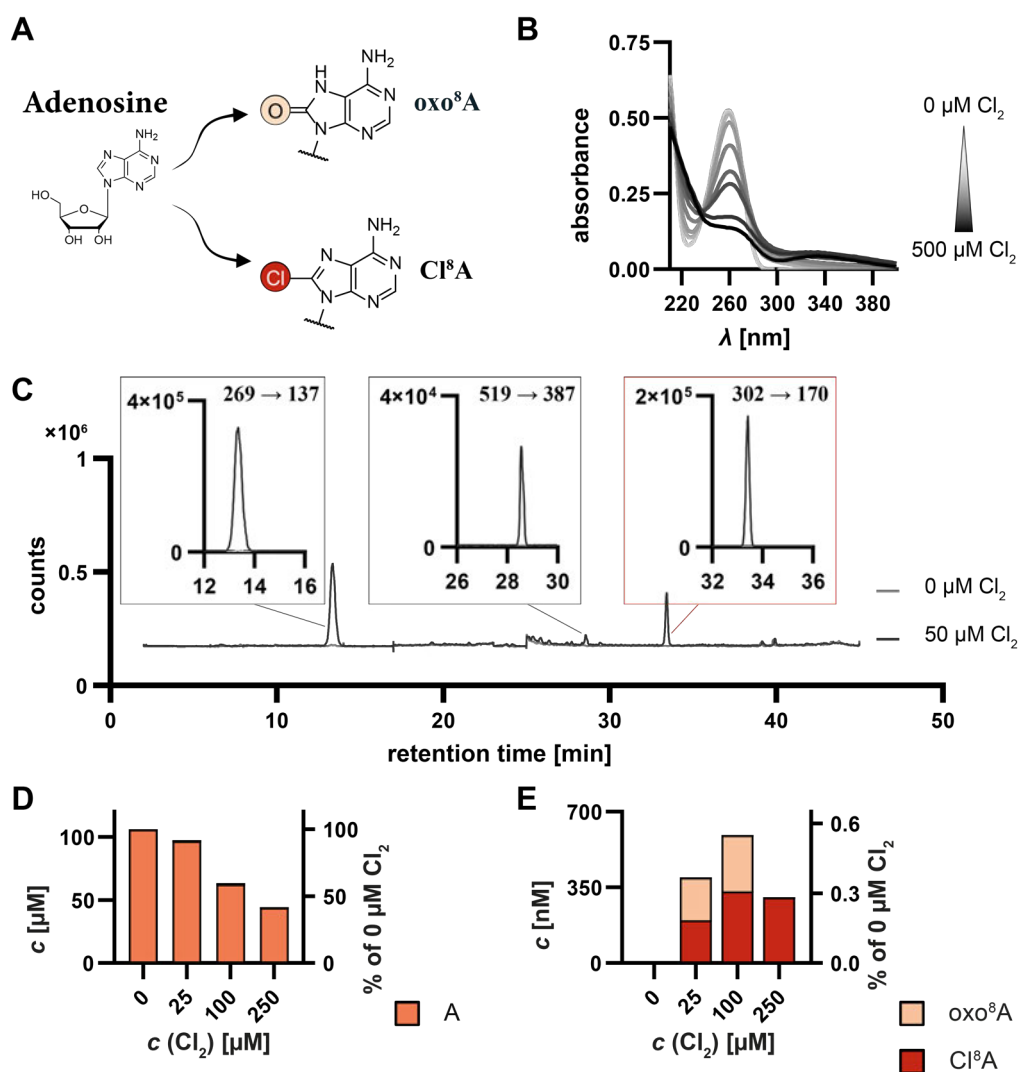


Figure 17. UV and LC-MS results of oxidized adenosine.

A Illustration of the oxidation reaction of adenosine (A) at the C8 position leading to the formation of 8-oxoadenosine (oxo⁸A, light orange) and 8-chloroadenosine (Cl⁸A, dark orange). **B** UV absorbance spectra of A under oxidation with HOCl ranging from 0 – 500 μM Cl_2 concentrations (represented from light gray to black). Reduction in absorbance at 260 nm was observed alongside the emergence of a new peak at 340 nm. **C** Total ion chromatograms of adenosine treated with 0 μM Cl_2 (light gray) and 50 μM Cl_2 (dark gray) illustrating MS counts experiencing a mass loss of 132 corresponding to a ribose over a 54-minute gradient. Extracted ion chromatograms highlight prominent signals in oxidized A at 13.3 min (m/z 269 \rightarrow 137), 28.6 min (m/z 519 \rightarrow 387) and 33.4 min (m/z 302 \rightarrow 170). **D** Absolute quantification of A at various oxidant concentrations (0, 25, 100, and 250 μM Cl_2) revealing decreasing abundances down to approximately 45% of A present in the untreated control (expressed in μM concentrations related to initial reaction volumes). **E** Representation of absolute amounts of oxo⁸A and Cl⁸A per μL for 0, 25, 100, and 250 μM Cl_2 concentrations in nM nucleoside concentrations. Oxidation products reached maximum abundances at 100 μM Cl_2 followed by a decline. Values are shown as mean ($n = 2$) \pm SD.

Dimer formation initiates through oxidation at C8 facilitating a nucleophilic attack at C2 of the purine moiety, a unique characteristic of adenosine due to the inhibitory effect of the amine group at the corresponding position of guanosine. Figure 18 depicts the mechanism of dimer formation on oxo⁸A being oxidized to an iminoquinone in a first step. The iminoquinone facilitates nucleophiles such as nitrogens (green) present in other purines to attack its C2 position (highlighted with a red asterisk). The resulting product is a covalently linked oxo⁸A-A dimer.^{62,133}

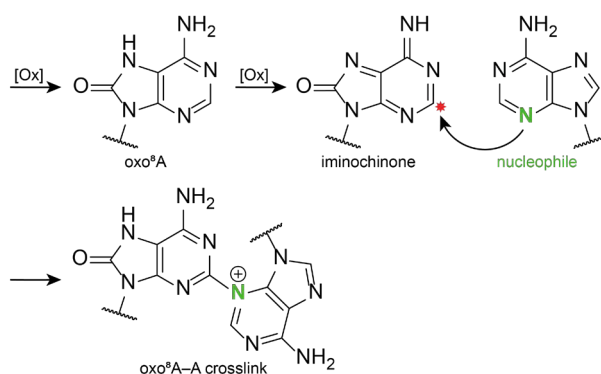


Figure 18. Cross-link formation between oxo⁸A and A induced by oxidation.

Oxidation of adenosine leads to the formation of oxo⁸A which can undergo a second oxidation reaction leading to an unstable iminoquinone derivative. The C2 position (red asterisks) of the iminoquinone is susceptible to nucleophiles such as nitrogens (green) present in other purines. Resulting crosslinking products typically exceed m/z 400. Figure adapted from Nilov *et al.* 2013.⁶²

LC-MS/MS quantification confirmed decreased quantities of adenosine (Figure 17D) alongside increasing amounts of oxo⁸A and Cl⁸A with escalating concentrations of applied oxidant (Figure 17E). At 250 μ M Cl₂ less than 50% of A present in the untreated control remained while the C8 oxidation products accounted for only less than 1%. The same results were obtained in oxidized adenosine monophosphate (AMP) analyzed via LC-MS (Figure S6C). This suggested the generation of additional, yet undetected oxidation products that were not quantified. Another notable difference was observed in the response to increasing concentrations of oxidant. While pyrimidine oxidation products exhibited a constant increase, oxo⁸A and Cl⁸A did not show further enhancements with higher oxidant concentrations suggesting the possibility of secondary reactions consuming primary oxidation products.

Comparative analysis of adenosine and pyrimidine oxidation revealed marked differences in the quantity of detected products. While analyzed pyrimidine oxidation products encompassed the total initially present main nucleosides either as the sum of Cl⁵C plus cytidine or only uridine, the total of detected products of adenosine only amounted to approximately 50% of adenosine in the untreated control. Possible explanations include alternative oxidation reactions on the nucleobase, dimerization, and the generation of abasic sites. While respective oxidation products have been documented for guanosine, comparable studies on adenosine remain scarce.⁷² Reported alternative products include Fapy-A and inosine, observed in one-electron oxidation systems not readily transferrable to HOCl oxidation reactions.^{42,134,135} However, both were not present in sufficient quantities to account for the lack of detected nucleoside. The formation of abasic sites will be discussed in the subsequent Chapter 8.4 on binary oligoribonucleotides, while dimer formation was previously mentioned in this chapter.

Adenosine's unique nucleophilic C2 position upon oxidation renders it the only nucleoside capable of dimerization.^{62,133} This feature is of particular interest in the context of structured RNA and can be utilized for RNA-RNA and RNA-protein structure probing.^{136,137} From a pathophysiological perspective, crosslinks lead to the impairment of both macromolecules being potentially toxic to the cellular metabolism. As the formation of crosslinks was not the primary focus of this PhD project, further investigations are essential to identify crosslinked adenosine species and analyze *in vivo* effects.

8.3.3 Guanosine – the most susceptible nucleoside

Guanosine is the nucleoside most prone to oxidation, particularly at position C8 resulting in the formation of 8-oxoguanosine (oxo⁸G) and 8-chloroguanosine (Cl⁸G) illustrated in Figure 19A. Additionally, oxidation at C5 can generate alternative oxidized nucleosides, which will be discussed later in this chapter.

UV spectra of oxidized guanosine presented in Figure 19B revealed substantial changes in absorbance. An extensive decrease in absorbance at 260 nm indicated oxidation-induced alterations in the chromophore. This drop in absorbance from approximately 0.42 (0 μM Cl₂ in light gray) to 0.13 (500 μM Cl₂ in black) in parallel with elevated absorbances lower than 240 nm and higher than 300 nm suggested the occurrence of several oxidation reactions (Figure S3D). Reference spectra of oxo⁸G and Cl⁸G are provided in Figure S4D for comparison and identification purposes.

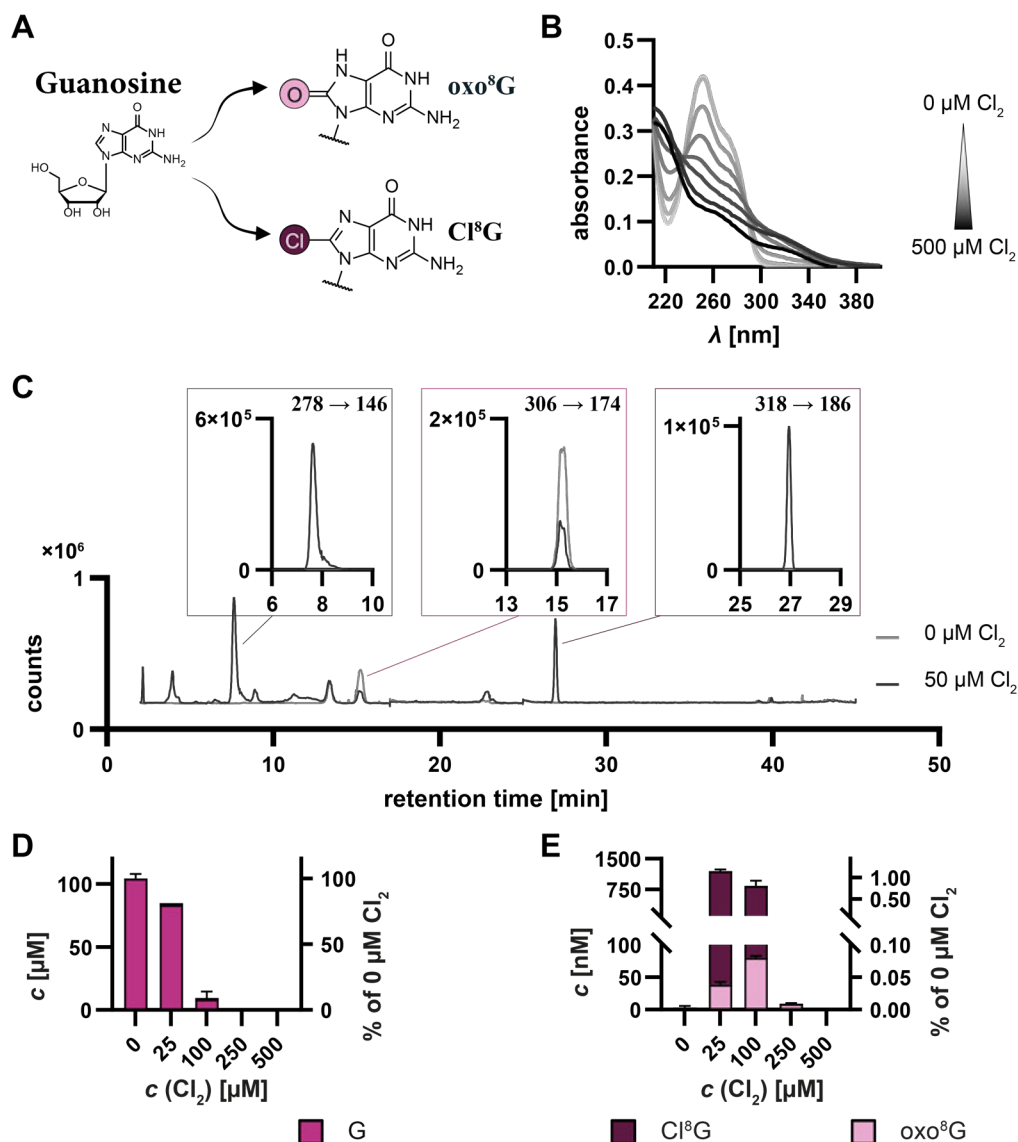


Figure 19. Guanosine nucleoside oxidation exhibited high reactivity resulting in a variety of products.

A Guanosine experiences primary oxidation at position 8 leading to the formation of 8-oxoguanosine (oxo^8G , light pink) and 8-chloroguanosine (Cl^8G , dark pink). **B** UV spectra of 100 μM guanosine (G) oxidized with increasing concentrations of Cl_2 (0 – 500 μM , represented from light gray to black). **C** Total ion chromatograms illustrate detected counts of nucleosides experiencing a mass loss of 132 corresponding to a ribose moiety for untreated control (0 μM Cl_2 , light gray) and guanosine treated with 50 μM Cl_2 (black). Insets display extracted ion chromatograms for mass transitions of m/z 278 \rightarrow 146, m/z 306 \rightarrow 174 and m/z 318 \rightarrow 186. The signal at m/z 306 corresponds to the sodium adduct of guanosine ($[\text{G}+\text{Na}]^+$), while the signal at m/z 318 was attributed to $[\text{Cl}^8\text{G}+\text{H}]^+$ by comparison with external standards. **D** Absolute amounts per μL of G and its oxidation products are depicted upon oxidation with increasing concentrations of Cl_2 (0, 25, 100, 250, and 500 μM) quantified by LC-MS using external calibration. Left y-axis shows the concentration of nucleoside in μM present in the reaction and the right y-axis indicates the proportion related to 0 μM Cl_2 treated G. **E** illustrates abundances in nM concentrations with otherwise identical depictions.

The NLS scan conducted on 50 pmol oxidized guanosine as shown in Figure 19C provided further insights into the oxidation products. The analysis revealed reduced signals corresponding to the parent nucleoside eluting at 15.2 minutes, detected as its sodium adduct (m/z 306), indicating consumption of guanosine due to oxidation. New signals emerged at approximately 2.2, 3.9, 7.6, and 27.1 minutes suggesting the formation of oxidation products. Further analysis of the signals eluting at 2.2 and 3.9 minutes will be addressed in subsequent section 8.3.4. The signal observed at

7.6 minutes (m/z 278) exhibited isotopic MS signals of +2, indicative of the presence of a chlorine atom; however, definitive conclusions were drawn at this juncture. The oxidation product detected at 27.1 minutes was identified as Cl⁸G based on comparison with an external standard. Major signals corresponding to m/z values of 318, 340, and 356, representing proton, sodium, and potassium adducts of Cl⁸G, respectively, confirmed its identity. Notably, chlorinated nucleosides demonstrated a preference for forming sodium adducts over proton adducts, a trend observed across all nucleosides. An NLS scan of DTT-quenched guanosine was also performed and the corresponding TIC is provided in the appendix (Figure S5D). Quantification via LC-MS/MS revealed consumption of guanosine even at low concentrations of 25 μ M Cl₂ becoming undetectable at 250 μ M Cl₂ underscoring its pronounced susceptibility to oxidation (Figure 8D). Similarly to adenosine, analyzed oxidation products (oxo⁸G and Cl⁸G) did not constitute 100% of the initially present guanosine, accounting for only about 1% at moderate Cl₂ concentrations and decreasing thereafter. As for the other nucleosides, respective oxidation reactions were also performed on GMP yielding comparable results (Figure S6D).

8.3.4 Identification of alternative guanosine oxidation products

The identification of various oxidation products of guanosine has been the subject of extensive research particularly focusing on deoxyguanosine/-guanine.^{61,70,72} These oxidation products include both C8 and C5 oxidation derivatives as illustrated in Figure 20. C8 oxidation products are oxo⁸G and Cl⁸G as well as the oxo⁸G-derived 4 e⁻ oxidation products: guanidinohydantoin (rGh) and spiroiminodihydantoin (rSp). Alternatively, oxidation can occur at C5 of guanosine leading to the 2 e⁻ oxidation products: 5-carboxamido-5-formamido-2-iminohydantoin (r2Ih), diiminoimidazole (rDiz) and the 4 e⁻ oxidation products imidazolone (rIz) and its hydrolyzed counterpart oxazolone (rZ).

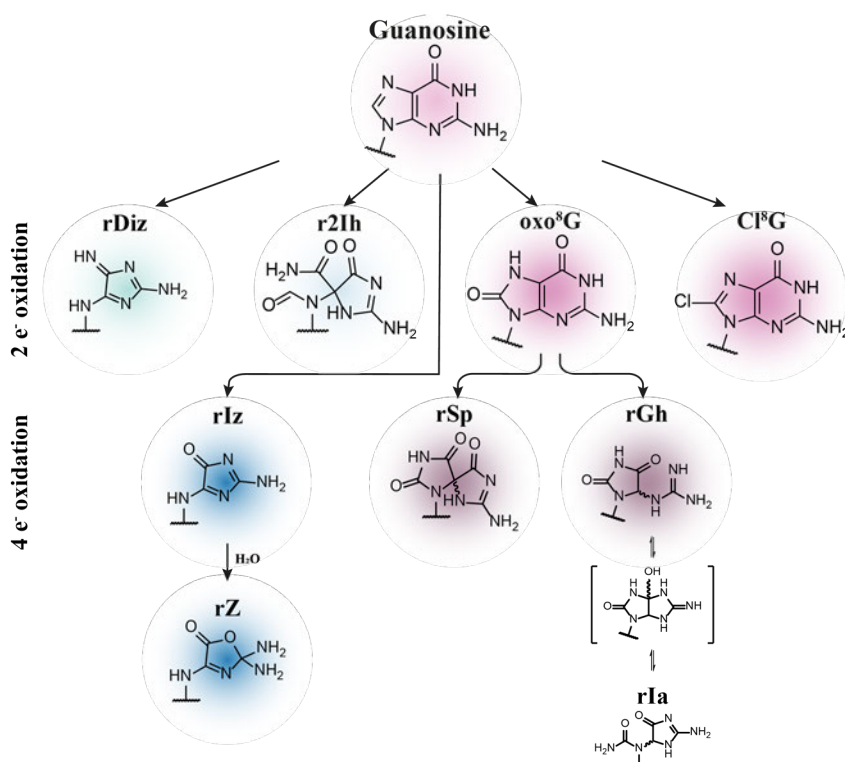


Figure 20. Oxidation products of guanosine (light pink) generated upon two-electron (e⁻) (top) and four-electron (bottom) oxidation reactions.

Oxidation at C5 of the purine moiety results in the 2 e⁻ oxidation products diiminoimidazole (rDiz, light green) and 5-carboxamido-5-formamido-2-iminohydantoin (r2Ih, light blue). Corresponding 4 e⁻ oxidation products are imidazolone (rIz, blue) and its hydrolyzed counterpart oxazolone (rZ, blue). C8 oxidation leads to the formation of 8-oxoguanosine (oxo⁸G, pink) and 8-chloroguanosine (Cl⁸G, pink). Guanidinohydantoin (rGh, dark pink) and spiroiminodihydantoin (rSp, brown) are subsequent oxidation products from oxo⁸G upon another two-electron oxidation. Isomerization of rGh ends in the formation of iminoallantoin (rIa) with rGh being the predominant isomer for pH < 10.1.

Isotopically labeled ¹³C- and ¹⁵N-guanosine alongside native ¹²C-guanosine for oxidation were utilized for identifying alternative oxidation products under our LC-MS/MS conditions in the absence of external standards. The use of isotopes offers a distinct advantage in LC-MS analysis including consistent chemical properties and chromatographic elution behavior. However, their differing masses enable the identification of nucleosides based on matched retention times after HPLC separation, as well as specific fragmentation patterns. Therefore, a multiple reaction monitoring (MRM) scan was selected for analysis, exploiting known mass transitions without requiring prior knowledge of retention times. Figure 21A and S7A illustrate analyzed nucleosides and their corresponding mass transitions.

Figure 21B provides MS chromatograms depicting normalized signals of ¹²C- (black), ¹³C- (pink) and ¹⁵N- (green) isotopes over time for selected guanosine oxidation products. Analysis revealed that all investigated oxidation products eluted within the initial 5 minutes, with some even eluting as early as 2 minutes corresponding to the dead volume of the LC-MS system. The overlay of respective MS signals shown in Figure 21B distinctly identified rSp at a retention time (*t_R*) of 2.1 minutes, rZ at 2.2 minutes, and rDiz at 3.8 minutes, as their chromatograms seamlessly merged into a single homogeneous signal. Additionally, corresponding chromatograms of r2Ih, rIz and rGh are shown in Figure S7B. While the MS signals for these oxidation products were not as conclusive due to relevant background levels, careful evaluation allowed for the assignment of signals at 2.1 minutes to rIz and signals at 2.2 minutes to r2Ih and rGh.

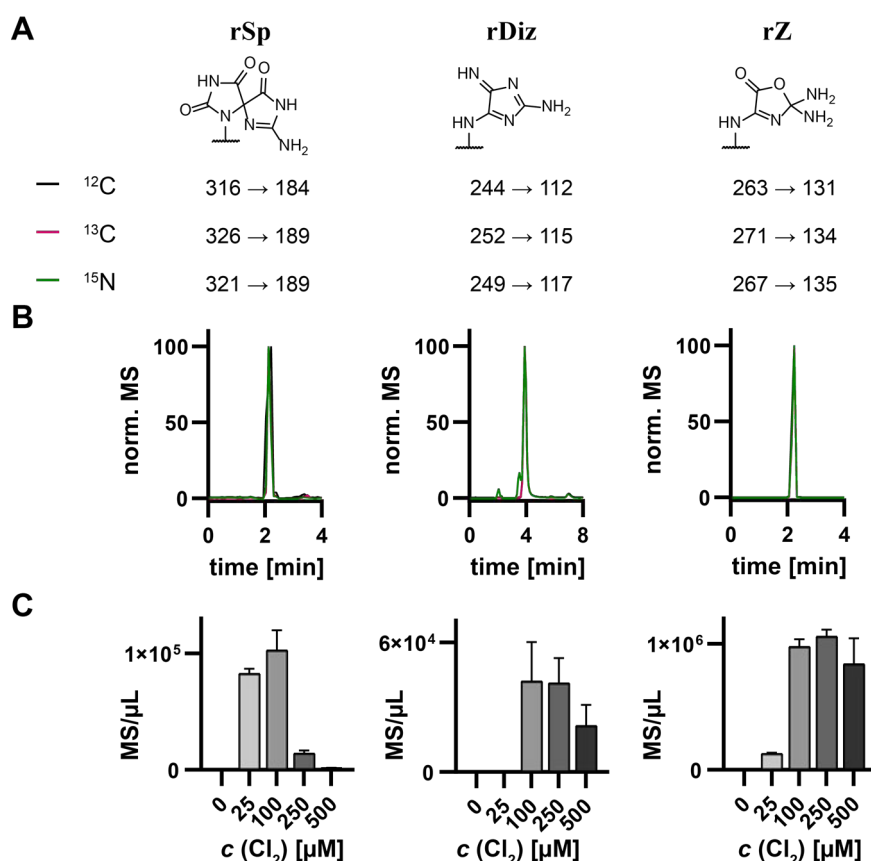


Figure 21. Identification of alternative guanosine (G) oxidation products using ^{12}C -, ^{13}C - and ^{15}N -guanosine.

Isotope-labeled G was subjected to oxidation with 50 μM Cl_2 , followed by analysis of 50 pmol using LC-MS/MS in MRM mode. **A** Structures and mass transitions of ^{12}C (top), ^{13}C (middle) and ^{15}N isotopes for spiroiminodihydantoin (rSp, left), diiminoimidazole (rDiz, middle) and oxazolone (rZ, right) are depicted. **B** Normalized MS signals for rSp, rDiz and rZ of the ^{12}C (black), ^{13}C (pink) and the ^{15}N (green) isotopes were merged to identify signals corresponding to the oxidation products of interest. Nucleosides adhering to the mass transitions listed in A eluted within 5 minutes on an RP-18 column using a gradient of 10 mM NH_4OAc , pH 5.8 and acetonitrile. **C** Presentation of the results obtained from oxidized ^{12}C -guanosine across a range of 0 μM (light gray) to 500 μM Cl_2 (dark gray) displayed as MS signals normalized to the initial reaction volume.

The examination of oxidized guanosine revealed varying levels of oxidation products other than oxo⁸G and Cl⁸G depending on the concentration of Cl_2 as presented in Figure 21C. Both rSp and rZ were detectable at 25 μM Cl_2 , while rDiz became apparent only at 100 μM Cl_2 and reached a maximum at that concentration. rZ levels plateaued at higher concentrations of oxidant. Moreover, the other oxidation product, including r2Ih, rIz and rGh, exhibited peaks at 100 μM Cl_2 mirroring the behavior observed with rSp (Figure S7C).

Guanosine stands out as the nucleoside most prone to oxidation when compared to uridine, cytidine, and adenosine as evidenced by its standard reduction potential $E^0(\text{G}) = 1.3 \text{ V}$.⁶⁹ This susceptibility leads to the quantitative depletion of the parent nucleoside observed through UV spectroscopy and mass spectrometry rather than the direct detection of oxidation products. Absolute quantification methods detected oxo⁸G and Cl⁸G each in abundances of up to 1% relative to untreated control levels of G. To explore alternative oxidation products, isotopically labeled ^{13}C - and ^{15}N - guanosine were employed for detection purposes. The formation of these products is accentuated by the lower redox potential of oxo⁸G itself ($E^0(\text{oxo}^8\text{G}) = 0.6 \text{ V}$)⁷¹ compared to that of guanosine $E^0(\text{G}) = 1.3 \text{ V}$.^{61,72} However, comparable studies in literature reveal, that their

generation strongly depends on various reaction conditions including the choice of oxidant, presence of reducing agents, pH, and temperature resulting in a complex array of guanosine oxidation products that have been under thorough investigation, particularly in DNA.^{61,70,72} Absolute quantification of these alternative oxidation products proved challenging due to the absence of external standards. Yet, it is conceivable that the chemical and biological properties of these oxidation products are significantly altered due to modifications in the nucleoside moiety compared to guanosine.³⁷ The observed maxima of most of these oxidation products may indicate subsequent downstream reactions potentially involving the formation of abasic sites. The forthcoming Chapter 8.4 on binary oligoribonucleotides will delve into the generation and detection of abasic sites in greater detail.

8.4 The Impact of sequence environment on nucleoside oxidation

8.4.1 Oxidation of binary oligoribonucleotides

Results of nucleoside oxidation revealed pronounced disparities among uridine, cytidine, adenosine, and guanosine, with uridine exhibiting the lowest reactivity under applied conditions as described in Chapter 8.3. In order to elucidate the consequences of oxidation within an RNA milieu, direct comparisons of the aforementioned nucleosides were undertaken utilizing binary oligoribonucleotides. Combinations featuring cytidine, adenosine, or guanosine paired with uridine were systematically examined to evaluate the influence of intramolecular interactions on the oxidative processes of nucleosides (Figure 22A).

Oxidation reactions were executed following our standard conditions outlined in the methods section, employing oligonucleotides at a concentration of 25 ng/ μ L in phosphate buffer pH 7.4, with oxidant concentrations ranging from 0 – 500 μ M Cl_2 . After quenching, RNA isolation was carried out through several steps to eliminate salts and other oxidation by-products prior to LC-MS analysis.

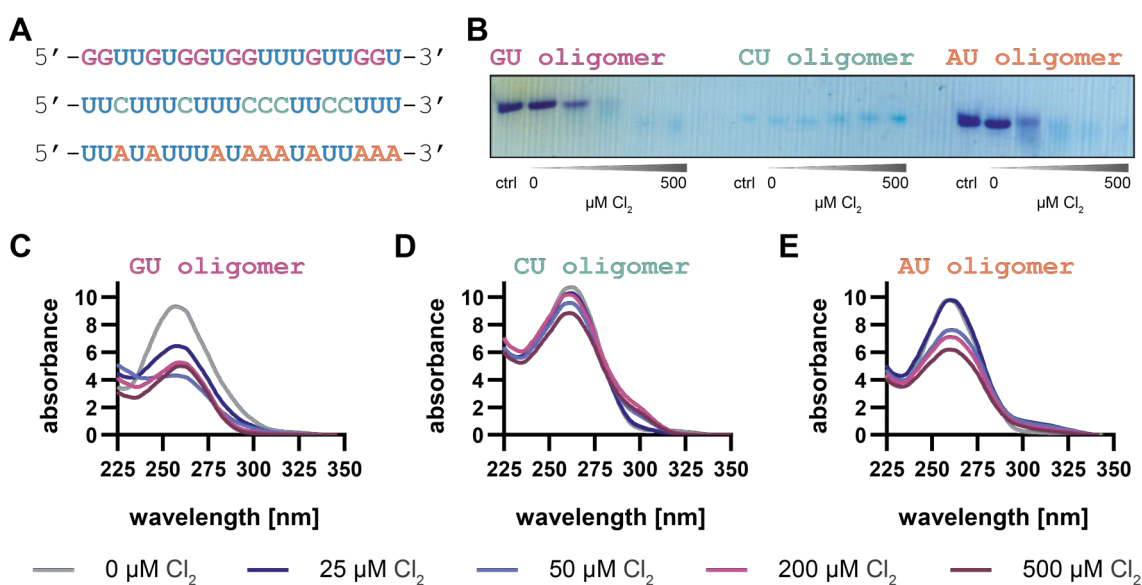


Figure 22. Binary oligonucleotides (GU, CU, and AU combinations) show distinct behaviors upon oxidation.

Sequences of binary oligoribonucleotides are depicted in **A**. **B** displays a 15% denaturing PAGE of samples including 250 ng oxidized oligonucleotide in the order of a control (ctrl) followed by 0, 25, 50, 200, and 500 $\mu\text{M Cl}_2$ treatments for each oligonucleotide (GU in pink, CU in green, and AU in orange). Staining was performed using Toluidine blue, because standard nucleic acid dyes e.g. GelRed are not compatible with specific binary nucleotide combinations. Bands show changes in migration behavior upon oxidation. GU and AU were affected to a higher degree as bands vanished and migrated faster than visual for the CU combination. Color differences are characteristic of each nucleoside composition. **C - E** Absorbance spectra of the same samples after purification (**C**: GU oligonucleotide, **D**: CU oligonucleotide, and **E**: AU oligonucleotide). In line with denaturing PAGE results, the GU and AU oligonucleotides revealed stronger changes in absorbances than the CU combination. Absorbances were lowered for purine + uridine oligonucleotides at 25 $\mu\text{M Cl}_2$ (**C**: GU) and 50 $\mu\text{M Cl}_2$ (**E**: AU) while spectra of oxidized CU (**D**) oligonucleotides only showed slightly decreased absorbances at 260 nm.

Figure 22B shows a 15% denaturing PAGE of oxidized oligonucleotides (GU, CU, and AU) with increasing concentrations of Cl₂ (0, 25, 50, 200, and 500 μM). An aliquot equivalent to 250 ng of initial oligonucleotide was directly taken after quenching before any purification steps to ensure uniform RNA quantities across varying conditions. Staining was performed using Toluidine blue due to its interaction with negatively charged molecules such as those in the phosphate backbone¹³⁸ because ethidium bromide-based dyes such as GelRed were unable to interact with certain nucleotide combinations. The color of Toluidine blue-stained bands differed in intensity and blue shade depending on the oligonucleotide and applied Cl₂ concentration. Bands corresponding to the GU oligonucleotide (pink) began disappearing at 25 μM Cl₂, accompanied by a downward shift indicative of RNA integrity alterations. Conversely, the CU oligonucleotide (green) exhibited no changes in band appearance or migration behavior, while the AU combination (orange) mirrored the observation for the GU oligonucleotide (pink) albeit to a lesser extent.

In Figure 22C-E absorbance spectra for corresponding oxidized oligonucleotides are depicted in order to examine RNA integrity using a Nanodrop™ device. These spectra revealed a hypochromic shift at 260 nm, concomitant with a bathochromic shift indicating the formation of oxidation products characterized by an increased chromophore, resulting from the incorporation of additional oxygen and chlorine atoms (Figure S4). Hypochromic alterations were particularly pronounced in the GU (pink) and AU (orange) combinations (Figure 22C, E) pointing to a decline in nucleobase content, while the bathochromic shift was observed in all three binary oligonucleotides (Figure 22C-E).

In the next step, quantification of parent nucleosides and oxidation products was conducted using tandem mass spectrometry. Measurements of 25 ng (~75 pmol nucleoside) digested sample were performed in a dMRM mode with external standards for calibration purposes as described for nucleosides (Chapter 8.2.1 and 10.2.15). Results are presented as nucleoside concentration in oxidation reactions in relation to the applied oxidant (Figure 23). Furthermore, the relative amounts are depicted on the right y-axis, normalized to control samples (0 μM Cl₂). Figure 23A illustrates the concentrations of parent, chlorinated, and oxygenated nucleoside within the GU oligonucleotide displayed in μM. In the untreated control the G vs. U ratio was 1:1 consistent with its sequence (Figure 22A). This ratio shifted towards higher proportions of uridine, culminating in the exclusive detection of uridine. Only Cl⁵U reached picomole concentrations, while ho⁵U was not detected under applied conditions. Oxidation products of guanosine, oxo⁸G, and Cl⁸G, were only present in femtomole quantities (Figure 23B). Conversely, the C-to-U species ratio remained relatively stable in the CU oligonucleotide combination. Decreased cytidine levels were observed with increasing Cl₂ concentrations, accompanied by the generation of Cl⁵C at the expense of its parent nucleoside (Figure 23C). Oxidation products of uridine were detectable only in femtomolar ranges (Figure 23D). The binary oligonucleotide containing adenosine and uridine exhibited behavior akin to the GU combination with significant A reduction across all Cl₂ concentrations, primarily yielding Cl⁵U as the major oxidation product (Figure 23E, F).

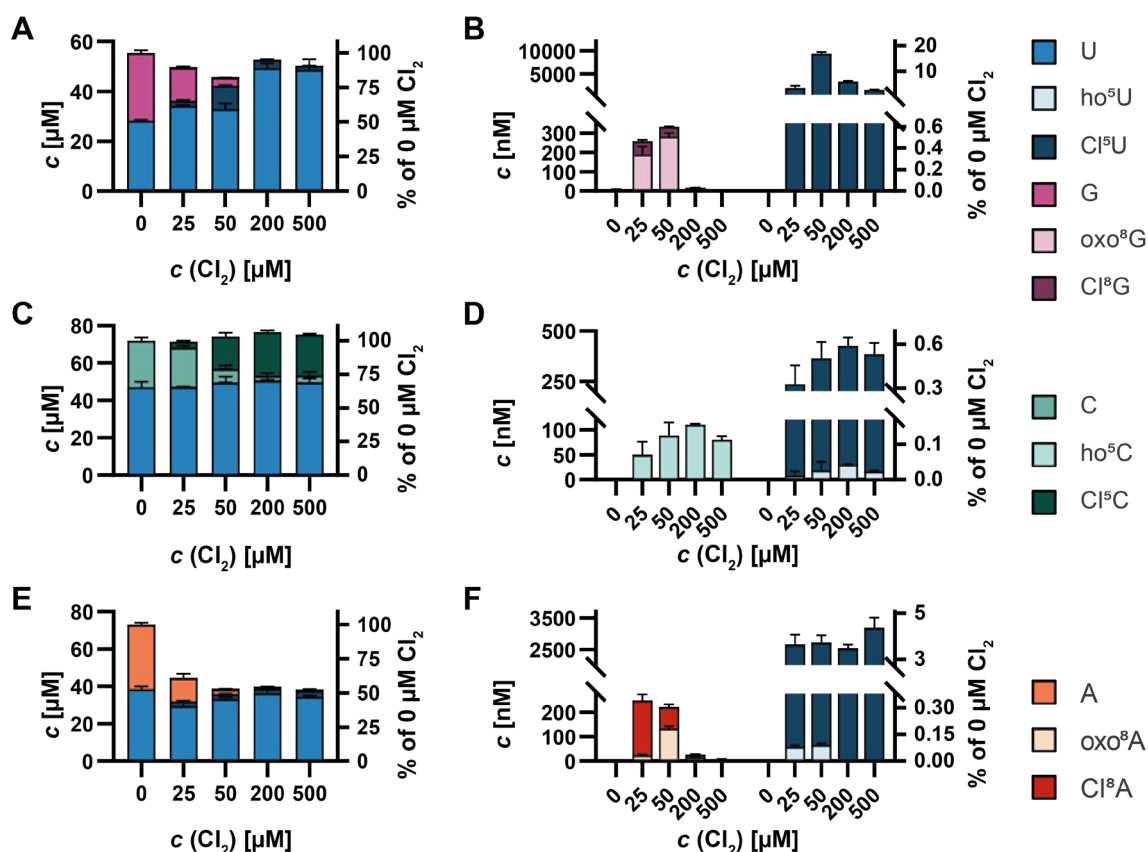


Figure 23. Quantification of oxidation products in binary oligonucleotides revealed similar sensitivities towards oxidation as detected in nucleosides.

25 ng (~75 pmol nucleosides) oxidized sample was digested and measured in a dMRM mode detecting oxo- and chloro-products. Graphs on the left (**A**, **C**, **E**) indicate the amount of nucleoside in μM in relation to applied Cl_2 concentrations. Right graphs (**B**, **D**, **F**) display low abundant oxidized nucleosides in nM. The right y-axis indicates the proportion related to untreated control ($0 \mu\text{M Cl}_2$). Results of the GU oligonucleotide are shown in **A** (μM) and **B** (nM), the CU combination in **C** (μM) and **D** (nM), and the AU combination is shown in **E** (μM) and **F** (nM). Cl^5U was detected in picomolar ranges in all combinations, whereas ho^5U was only detectable in low femtomolar quantities in the CU and AU oligonucleotides. Guanosine levels decreased by 50% at $25 \mu\text{M Cl}_2$ and were undetectable at $200 \mu\text{M Cl}_2$, while uridine levels increased proportionally with Cl_2 concentrations reaching near-complete levels at $500 \mu\text{M}$ applied Cl_2 (**A**). Oxidation products of guanosine were only present in femtomolar ranges and were most abundant at $50 \mu\text{M Cl}_2$ (**B**). Only Cl^5C was detectable in picomolar quantities and was formed at the expense of its parent nucleoside (**C**). While the total of detected nucleosides ended up at about 100% of initially present nucleosides in the GU and CU combination (**A**, **E**), this was not the case for the AU combination. The amount of uridine stayed constant whereas oxidation products of adenosine did not account for the consumed parent nucleoside indicating the presence of alternative products, which were not detected in our LC-MS method. Data are presented as mean values \pm SD, $n = 3$.

Oxidation reactions on binary oligonucleotides revealed discrepancies among the four main nucleosides regarding their sensitivity to oxidation. As observed for nucleosides (Chapter 8.3), uridine exhibited the least sensitivity, while cytidine was almost quantitatively converted into its chlorinated counterpart. In contrast, both purines exhibited dynamic changes, with oxidation products reaching maximum abundances at medium oxidant concentrations, but only occurring in a thousandth of an order of magnitude. Additionally, alterations in RNA integrity induced by oxidation were observed leading to altered migration patterns and absorbance spectra. While purine bases may undergo various oxidation mechanisms, including the formation of hydantoin as described for nucleosides (Chapter 8.3.4),⁷² the CU oligonucleotide exhibited migration patterns suggesting a different pathway involving solely the generation of oxidized nucleosides alone. LC-MS analysis confirmed the presence of uridine and cytidine species, constituting 100% of the expected nucleoside content. In

the GU combination, there was a notable increase in uridine abundance at the expense of guanosine and its oxidized derivatives. This observation suggests that detected nucleosides, quantified via UV absorbance, contributed to the injected amount of 25 ng of oligonucleotide as LC-MS quantification resulted in about 100% of untreated control. However, this trend was not observed within the AU oligonucleotide. With increasing oxidant concentrations, the relative amount consistently decreased, reaching approximately 50% of control in 500 μM Cl_2 . While the amount of uridine remained constant, adenosine species nearly disappeared, possibly due to the formation of alternative oxidation products as described in Chapter 8.3.4 for guanosine.⁷² The LC-MS/MS quantification results of the remaining binary oligonucleotides, AC, AG, and CG are presented in Figure S8. The analysis confirmed guanosine as the nucleoside with the highest reactivity and showed similar reactivities for adenosine and cytidine. An alternative outcome of oxidation reactions is the formation of abasic sites⁷⁹ arising from the loss of a nucleobase, thereby affecting molecular weight and consequently, size resulting in decreased retention during electrophoresis.

8.4.2 Detection of abasic sites in binary oligoribonucleotides

The progressive disappearance of bands and LC-MS signals with escalating oxidant concentrations suggested that oxidation induced more severe damage beyond mere nucleoside oxidation. Alternatively, abasic or apurinic/aprimidinic (AP) sites (Figure 24A, 1) are known to form in the context of oxidative damage to RNA and DNA. To assess the loss of nucleobase, an aldehyde-reactive probe (ARP, Figure 24A, 2) was employed to identify such damaged sites. This ARP is functionalized with a fluorescent dye (Alexa Fluor™ 488) via a linker (Figure 24A, 2, green), which facilitates detection via gel electrophoresis concurrently with other dyes such as ethidium bromide-based ones like GelRed. Figure 24A illustrates the reaction scheme between the resultant abasic site (1) and the ARP reagent (Alexa Fluor™ 488 hydroxylamine, 2). Abasic sites solely consist of a ribose moiety, existing in equilibrium between the closed-ring hemiacetal and the aldehyde as its open-ring counterpart. The ARP reagent features a hydroxylamine group (Figure 24A, 2, orange) acting as a nucleophile towards the ribose aldehyde, yielding an oxime (3) comprising the open ribose and the ARP reagent.

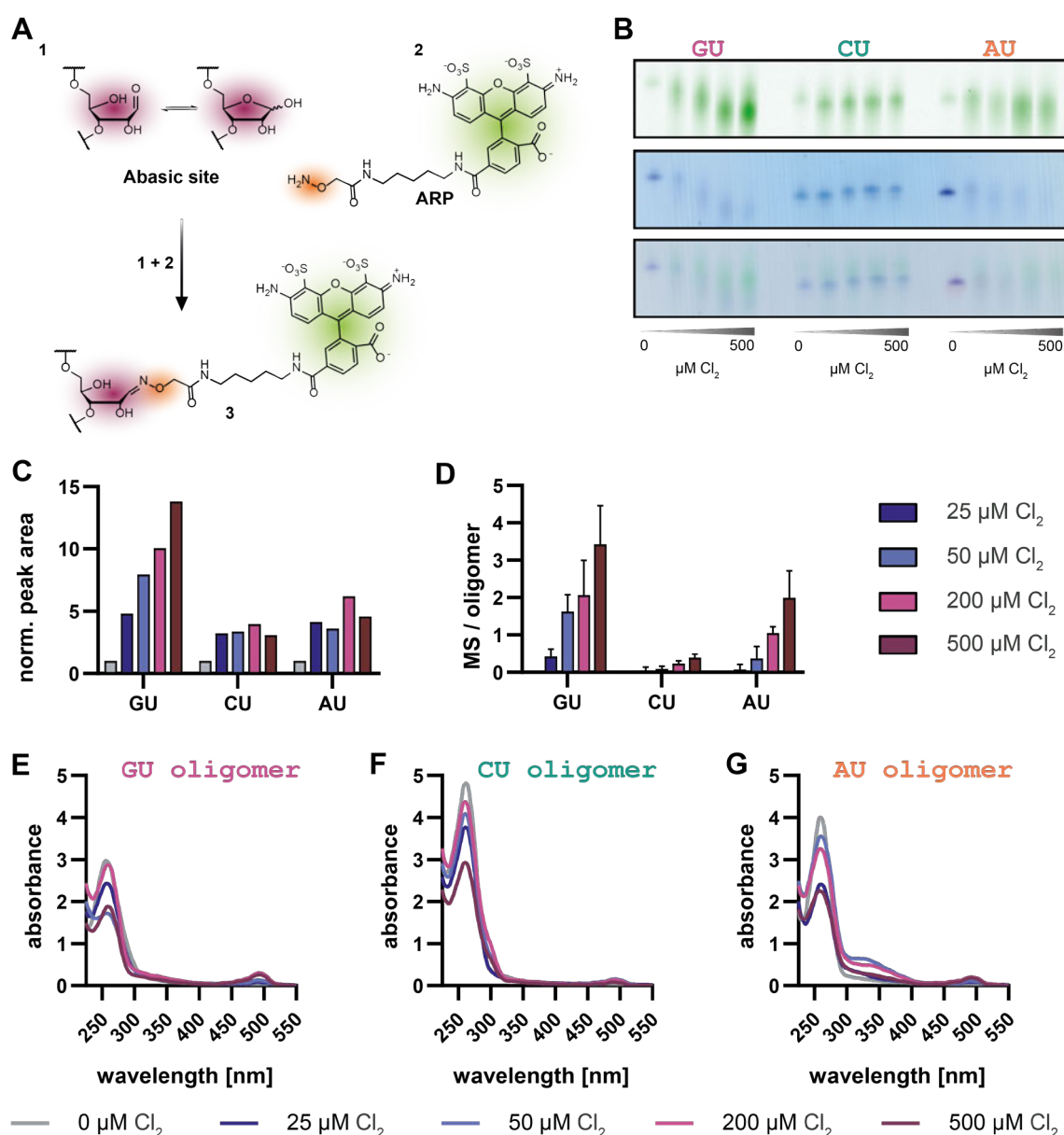


Figure 24. Detection of abasic sites using an aldehyde-reactive probe in binary oligonucleotides.

A Reaction scheme illustrating an abasic site 1 (pink) reacting with an abasic site reactive probe (ARP) 2 containing a fluorescent dye (green) and a nucleophilic hydroxylamine moiety (orange) resulting in the formation of a covalently linked fluorescently labeled AP site (3). **B** 15% denaturing PAGE of ARP-labeled binary oligonucleotides. A total of 150 ng of GU (pink), CU (green), and AU (orange) oligonucleotide was loaded in increasing Cl_2 concentrations (0, 25, 50, 200, and 500 $\mu\text{M Cl}_2$). The upper panel shows the fluorescent scan ($E_{\text{ex}} = 488 \text{ nm}$, $E_{\text{em}} = 526 \text{ nm}$) visualizing covalently-linked AP sites. The middle panel displays the corresponding Toluidine blue image of the same gel after staining. The lower panel presents the merged image of both scans. **C** Integrated fluorescent signal normalized to the signal of 0 $\mu\text{M Cl}_2$ for the respective oligonucleotide revealing increased intensities for oxidized samples in all binary combinations. The strongest signal was observed for the GU oligonucleotide consistently increasing with oxidant concentrations. **D** ARP-ribose adduct MS signal (3, m/z 824) normalized to the absolute amount of U and corrected by the number of potential reactive sites ($G = 10$, $A = 10$ and $C = 7$). Results are presented as mean \pm SD, $n = 3$. **E – G**: Absorbance spectra of labeled oligonucleotides ranging from 225 nm to 500 nm.

Considering the low reactivity of uridine upon oxidation under applied conditions, binary oligonucleotides (GU: pink, CU: green, and AU: orange) were utilized to determine which nucleoside can form abasic sites. ARP labeling was conducted on oxidized oligonucleotides (as described in 8.4.1) using 100 μM ARP reagent. Excess reagent was removed using the Oligo Clean & Concentrator™ kit and an aliquot equal to $\sim 150 \text{ ng}$ of

the 0 μM Cl_2 sample was loaded on a 15% denaturing PAGE (Figure 24B). The upper panel shows the fluorescent scan indicating labeled abasic sites followed by the Toluidine blue scan and the merged image of both scans at the bottom. Samples loaded on the gel were as follows: 0, 25, 50, 200, and 500 μM Cl_2 oxidized and labeled GU, CU, and AU oligonucleotides. Bands increasingly smeared with ascending concentrations of oxidant that shifted downward observable in the fluorescent and Toluidine blue scan particularly for the GU (pink) and AU (orange) oligonucleotide. The overlay of both scans revealed an upshift upon labeling, counteracting the downshift observed upon oxidation (Figure 24B, lower panel) which is probably induced due to the additional presence of several ARP adducts. Quantification of band intensities was performed using ImageJ by normalizing each signal to the respective 0 μM Cl_2 treated samples for each oligonucleotide combination as depicted in Figure 24C. The GU (pink) combination exhibited the highest reactivity, followed by AU (orange) and CU (green). A linear increase in intensity was noted for GU, but not for CU and AU. This finding was corroborated by LC-MS quantification of the ARP-ribose product detected as the $[\text{M}+\text{H}]^+$ precursor ion (m/z 824). 100 ng of the digested sample was injected and MS signals were normalized to uridine, which is considered unchanged upon oxidation, thus representing the actual amount of injected RNA (Figure 24D). As observed before, the quantities of the ARP-ribose adduct (Figure 24A, 3) exhibited a descending order of the overall abundance in the GU (pink), AU (orange), and CU (green) oligonucleotides. A consistent increase in signal intensity per oligonucleotide was observed not only for the GU combination, as analyzed via PAGE, but also in the AU and CU oligonucleotides. Moreover, the enrichment of the adduct was approximately four-fold higher in AU compared to CU. Confirmation of ARP reagent incorporation was also achieved by recording absorbance spectra ranging from 220 nm to 800 nm. Figures 24E-G depict overlapping spectra for each binary oligonucleotide combination (24E: GU, 24F: CU, 24G: AU) displayed separately for each oligonucleotide. A second peak emerged at 488 nm corresponding to the excitation wavelength of Alexa Fluor 488™ of the ARP reagent. However, due to potential variations in yield upon purification, quantitative conclusions cannot be drawn based on these spectra.

Considering these findings collectively, abasic sites were identified in oxidatively damaged binary oligoribonucleotides using the fluorescently labeled ARP reagent, Alexa Fluor™ 488 hydroxylamine. Gel electrophoresis facilitated the visualization of RNA integrity and indicated quantitative distinctions among G, C, and A which were further analyzed by LC-MS measurements. Semi-quantitative analysis was conducted based on normalized ARP-ribose signals. This analysis revealed the highest abundances of abasic sites in the GU combination, followed by AU and CU, while only small amounts were detected in the CU oligonucleotide compared to GU and AU. However, due to the unavailability of a standard for the ARP-ribose adduct, final conclusions regarding absolute quantities cannot be made at this point. Nevertheless, the reactivity towards the ARP reagent exhibited a comparable pattern to that observed for oxidation within the three binary combinations, as described in Chapter 8.4.1. Alternatively, it is worth considering that additional electrophilic sites may be generated serving as reaction partners for the hydroxylamine and contributing to the fluorescent signal detected via PAGE. Placing these findings within a broader biological context, oxidation promotes the formation of electrophilic sites that can react with nucleophiles present in proteins (e.g. cysteine, lysine), glutathione, and other biomolecules. The resultant covalent products may interfere with proper functionality, dynamic structural changes, and interactions crucial for maintaining physiological cellular processes.

8.5 Oxidation of ribonucleic acids

In the next step, the impact of oxidation on RNA molecules was explored with a particular focus on the proximity of nucleotides linked via their phosphate moiety. To achieve this, synthetic oligonucleotides and *in vitro* transcribed tRNA^{Asp} (IVT-tRNA^{Asp}) were subjected to oxidation reactions, with a subsequent comprehensive analysis through gel electrophoresis, mass spectrometry, and sequencing methodologies.

8.5.1 Examining the impact of oxidation on the phosphate backbone of RNA

A synthetic, unmodified oligonucleotide served as the basis for assessing RNA integrity following oxidation induced by HOCl. As elaborated in Chapter 8.4 focusing on binary oligonucleotides, oxidation significantly impacts RNA integrity. Synthetic oligonucleotides comprising all four main nucleosides - adenosine, cytidine, guanosine, and uridine - were subjected to oxidation and subsequent analysis through gel electrophoresis employing three orthogonal visualization techniques. A conventional method for nucleic acid visualization during gel electrophoresis involves staining with ethidium bromide-based dyes like GelRed, which interact with planar stacked nucleobases through π - π stacking. This interaction enhances the dye's fluorescence^{102,139} enabling the visualization of nucleic acids. However, as observed with binary oligonucleotides, oxidation not only generated oxidized nucleosides but also induced the loss of nucleobases resulting in the formation of apyrimidinic/apurinic (AP) sites commonly known as abasic sites. These abasic sites render intercalation-based staining less effective or completely abolish interactions, as depicted in Figure 25A.

To assess integrity within RNA molecules, synthetic oligonucleotides and IVT-tRNA^{Asp} were subjected to oxidation reactions followed by quenching. Subsequently, an aliquot corresponding to 100 ng of initially present RNA was directly loaded onto denaturing polyacrylamide gels. Figure 25B displays two denaturing PAGE gels of an oxidized synthetic oligonucleotide (upper panel) and IVT-tRNA^{Asp} (lower panel) stained with GelRed. Oxidation was performed within a concentration range of 0 to 1600 μ M Cl₂ following the standard protocol outlined in Chapter 10.2.9. Lane 1 and 11 included ladders, lane 2 contained an RNA loading control, and lanes 3 to 10 the oxidized samples. Upon oxidation, RNA bands became diffuse (lane 4) and were undetectable at approximately 50 μ M Cl₂ (lane 6) suggesting insufficient GelRed intercalation.

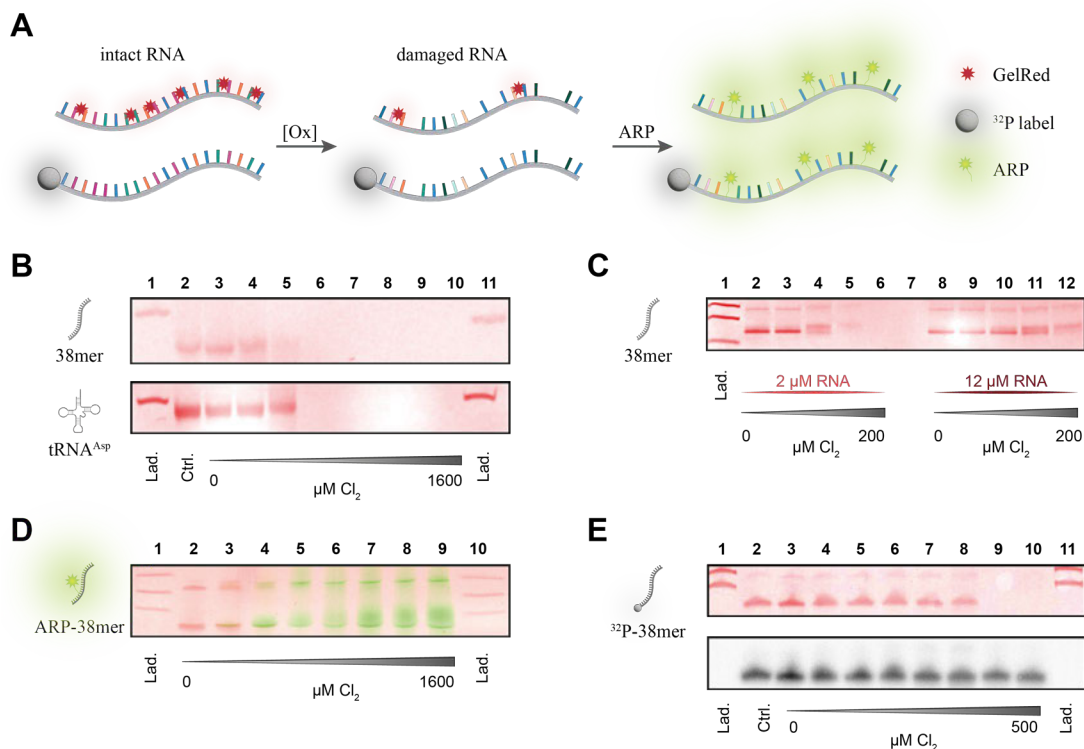


Figure 25. Visualization of RNA integrity by gel electrophoresis using ³²P- and ARP-labeling.

A Illustration of RNA visualization approaches affected by oxidation. Intact RNA (left) is stained by ethidium bromide-based dyes (red star) via intercalation between planar organized nucleobases. Oxidatively damaged RNA (middle panel) shows impaired staining due to the loss of nucleobases, which prevents π - π -interactions between dye and base. ³²P-labeling (indicated by gray balls) RNA molecules enables detection despite abasic sites as the label is attached at the 5'-end. Abasic or apyrimidinic/apurinic (AP) sites (right) are visualized by covalent linkage to fluorescent dyes (indicated by a green star) due to their reactive hemiacetal structure at the ribose moiety. **B** Denaturing PAGE gels of a synthetic oligonucleotide (top) and IVT-tRNA^{Asp} (bottom) after oxidation (0 – 1600 μ M Cl₂) stained with GelRed. Lanes 1 and 11: ladder (50 bp for top gel and 100 bp for bottom gel), lane 2: untreated control, lane 3 to 10: 100 ng of oxidized samples (0, 25, 50, 100, 200, 400, 800, 1600 μ M Cl₂). **C** RNA oxidized with 0, 25, 50, 100 and 200 μ M Cl₂ and RNA concentrations of 2 μ M (lane 2 – 6) and 12 μ M (lane 8 – 12). 100 ng was loaded and stained with GelRed. Lane 1 included a ladder with 20, 50, and 100 bp. **D** Merged 15% denaturing PAGE gel showing GelRed (red) and fluorescent (green) scans of oxidized and ARP-labeled oligonucleotide. Applied oxidant concentrations included 0, 25, 50, 100, 200, 400, 800, and 1600 μ M Cl₂ (lane 2 – 9). Lane 1 and 10: ladder with 20, 50, and 100 bp. **E** ³²P-labeled unmodified oligonucleotide subjected to oxidation (0, 10, 25, 50, 75, 100, 250 and 500 μ M Cl₂) and analyzed on a 15% denaturing PAGE gel. Lane 1 and 11: ladder indicating 50 and 100 bp, lane 2: RNA control, lane 3 – 10 included oxidized samples. Upper panel: GelRed scan, lower panel: phosphor image of the identical gel. **B – E** Gels were run at 20 W for 3 h loading an aliquot of 100 ng after oxidation reactions. ³²P-labeling was performed to reach 10,000 CPM radiation per 100 ng. Scans were performed for GelRed (E_{Ex}/E_{Em} : 532 nm/610 nm) and AlexaFluor™ 488 (E_{Ex}/E_{Em} : 488 nm/526 nm). Images were edited and merged using ImageJ. Created with BioRender.com (2024).

Figure 25C illustrates a gel comparing oxidation reactions of synthetic oligonucleotides at concentrations of 2 μ M (lane 2 – 6) and 12 μ M (lane 8 – 12) equivalent to 25 ng/ μ L and 150 ng/ μ L, respectively, under otherwise identical reaction conditions. Considering the behavior of HOCl oxidation on RNA, calculations for input quantities were conducted based on masses instead of moles. This choice was made because oxidation predominantly affects individual nucleotides rather than entire RNA molecules as observed in targeted reactions involving RNA and enzymes. Alternatively, the average molecular weight of the four nucleoside monophosphates (ϕ NMP = 339.5 g/mol) was used to calculate RNA concentration. Lane 1 included a ladder (20, 50, and 100 base

pairs) followed by oxidized samples spanning a range of 0 to 200 μM Cl_2 . Bands began to disappear at approximately 50 μM Cl_2 treatment of 2 μM oligonucleotide (lane 4) and 200 μM Cl_2 of the 12 μM oligonucleotide reaction (lane 12). The band running at 100 base pairs corresponds to the dimerized oligonucleotide, while the new band appearing slightly higher than the original band visible in 0 μM Cl_2 samples, represents an oxidized species. The displayed gel underscores the sensitivity of oxidation reactions particularly the ratio between oxidant and RNA. Results suggested that the reaction behaved more akin to a second-order reaction rather than the typical pseudo-first-order reaction observed in targeted processes like enzyme-catalyzed reactions,¹⁴⁰ as the outcome heavily depends on the concentrations of both reaction partners: RNA and HOCl. Hence, caution is advised when setting experimental conditions, hereby considering RNA concentrations, temperature, pH, or other reagents that may potentially quench oxidants.

As previously discussed in Chapter 8.4.2 the ineffective staining observed led to the hypothesis that abasic sites were formed within an RNA molecule. To validate this, an alternative labeling method was used utilizing a hydroxylamine-containing fluorescent dye named aldehyde-reactive probe (ARP). As represented in Figure 25A, visualization depends on the fluorescent ARP-ribose product upon covalent linkage between the ribose's aldehyde functionality and the nucleophilic ARP reagent.⁸⁵ Since Nanodrop quantification is based on the measurement of nucleobase UV absorbances, the resulting concentrations were deemed unsuitable for accurate calculations of RNA amounts, as the presence of abasic sites in significant quantities would not be reflected by measured values. Therefore, RNA amounts after purification were assumed to be like those of the 0 μM Cl_2 sample within the identical replicate series rather than the measured concentration retrieved from Nanodrop. Consequently, calculations for ARP experiments were based on the detected concentration of RNA present in untreated control after purification within one replicate of a series of eight samples. ARP labeling was performed according to the procedure outlined in Chapter 8.4.2 involving the incubation of oxidized oligonucleotide with the ARP reagent followed by the removal of excess ARP reagent. Equal volumes of each sample were then directly loaded on a 15% denaturing PAGE, stained with GelRed, and subsequently scanned for GelRed and Alexa Fluor™ 488. Figure 25D displays the corresponding merged image of an ARP-labeled oligonucleotide. Red bands indicate GelRed signals, while green bands result from the ARP-linked abasic site product. GelRed-stained bands diminished at 50 μM Cl_2 indicating insufficient intercalation, at the same time as Alexa Fluor™ 488 signals appeared representing labelled abasic sites.

Furthermore, a complementary approach was accomplished involving radioactive labeling of the oligonucleotide at its 5'-end which utilized ^{32}P -phosphorylation facilitated by T4 polynucleotide kinase and [γ - ^{32}P]-ATP to prove the integrity of the phosphate backbone, as illustrated in Figure 25A. Subsequently, the ^{32}P -labeled oligonucleotide was oxidized followed by gel electrophoresis of an aliquot equivalent to 10,000 CPM in 100 ng. ^{32}P -labeling and subsequent oxidation experiments were performed by [REDACTED]. Figure 25E depicts two images of the resulting 15% denaturing urea gel featuring a ladder (lane 1 and 11, with bands at 50 and 100 base pairs), a control of the oligonucleotide (lane 2), and samples subjected to oxidation with increasing Cl_2 concentrations (0, 10, 25, 50, 75, 100, 250 and 500 μM Cl_2 , lanes 3 - 10). The upper panel presents the GelRed scan (in red) while the lower panel presents the phosphor scan (in black) indicating the presence of ^{32}P -labeled RNA. GelRed bands were detectable up to 100 μM Cl_2 whereas ^{32}P signals were observed across the entire range of oxidant concentrations suggesting the integrity of the phosphate backbone even under the most

severe conditions regardless of any present abasic sites. The corresponding gel of the ARP labeling experiment is shown in Figure S9 confirming labeled abasic sites at 100 μM and 500 μM Cl_2 treatments.

Present findings on RNA integrity upon exposure to oxidative stress revealed the intactness of the phosphate backbone confirmed by three orthogonal nucleic acid visualization methods. GelRed staining turned out to be unsuitable for RNA that underwent severe oxidation as generated abasic sites inhibited intercalation and thus proper staining. This was also described by Hawkins *et al.* 2002 investigating the effect of HOCl oxidation on plasmid DNA and assuming that either backbone cleavage or formation of structures insensitive towards ethidium bromide staining were underlying reasons.⁵⁵ Alternatively, visualization was achieved by employing the unique aldehyde moiety present in abasic sites via labeling with a nucleophilic ARP reagent. Fluorescent signals of the ARP-abasic site product were only detectable in those samples insensitive towards GelRed staining indicating an intact phosphate backbone and the presence of remaining ribose moieties. This hypothesis was further verified by 5'-end labeling of the oligonucleotide with radioactive ^{32}P resulting in labeled product present over the complete range of oxidant concentrations.

The detection of abasic sites utilizing ARP labeling and downstream streptavidin pull-down in oxidatively damaged RNA was already performed by Tanaka *et al.*^{84,85} concluding that H_2O_2 -oxidized HeLa cells were dose-dependently enriched in abasic sites as well as *in vitro* γ -irradiated and Fenton-oxidized RNA. Findings in the literature also describe HOCl as another oxidant present *in vivo*⁵² and capable of generating reactive oxygen species (ROS) in the same way as the Fenton reagent, γ -irradiation, or peroxyxynitrite.⁷⁹ As abasic sites are known lesions in damaged RNA resulting from ROS, the formation of abasic sites by HOCl is very likely.

From a biological perspective, it has already been demonstrated in the literature that abasic sites in mRNA are involved in transcription regulation by stabilizing R-loops, which can induce RNA polymerase pausing, thereby inhibiting RNA synthesis.^{79,83} Abasic RNAs also function as important signaling molecules, being involved in stress responses. Their high chemical reactivity leading to the formation of crosslinked enzyme-RNA, RNA-RNA or other RNA dimers, as well as their impeded functionality, necessitate the existence of several repair and degradation enzymes that act particularly on oxo⁸G and abasic sites. The presence of oxo⁸G in mRNA results in ribosome stalling and subsequent decay and quality control processes. PNPase is an oxo⁸G-specific ribonuclease that degrades oxidized RNA. APE1 recognizes abasic sites that are either enzymatically generated through oxo⁸G removal by RNA glycosylases such as MPG or non-enzymatically formed by oxidation and initiates RNA repair or degradation.^{45,79} Since abasic sites are highly abundant oxidative lesions and based on their involvement in several biological processes, their detection, quantification, and localization are of high interest to gain a detailed understanding of the effect of oxidative stress *in vivo*.

8.5.2 LC-MS/MS quantification of oxidized nucleosides in RNA

To provide a deeper understanding of the dynamic formation of oxidation products within RNA molecules, a series of LC-MS/MS quantification experiments were conducted on oxidized IVT-tRNA^{Asp} and synthetic unmodified oligonucleotides.

Figure 26A illustrates the oxidation experiments performed on RNA, alongside downstream purification steps as described in the standard protocol in Chapter 10.2.9.

Treatments were performed on RNA at a concentration of 25 ng/ μL RNA equivalent to 75 μM nucleoside monophosphates (NMPs), with oxidant concentrations ranging from 0 to 1600 μM Cl_2 . Subsequent analysis included UV spectroscopy, mass spectrometry, and NGS-sequencing on an Illumina platform. Figure 26B presents UV spectra of oxidized RNA after purification recorded on a Nanodrop device. Oxidation covered a range between 0 μM (light gray) to 200 μM (black) Cl_2 exhibiting similar changes as observed in nucleosides alone (Chapter 8.3) including a hypochromic and a bathochromic shift at 260 nm and 300 nm, respectively, indicating the destruction of chromophores and the formation of chlorinated and oxygenated products. 50 ng of oxidized RNA was analyzed via mass spectrometry using external standards for absolute quantification following thorough purification to remove interfering salts.

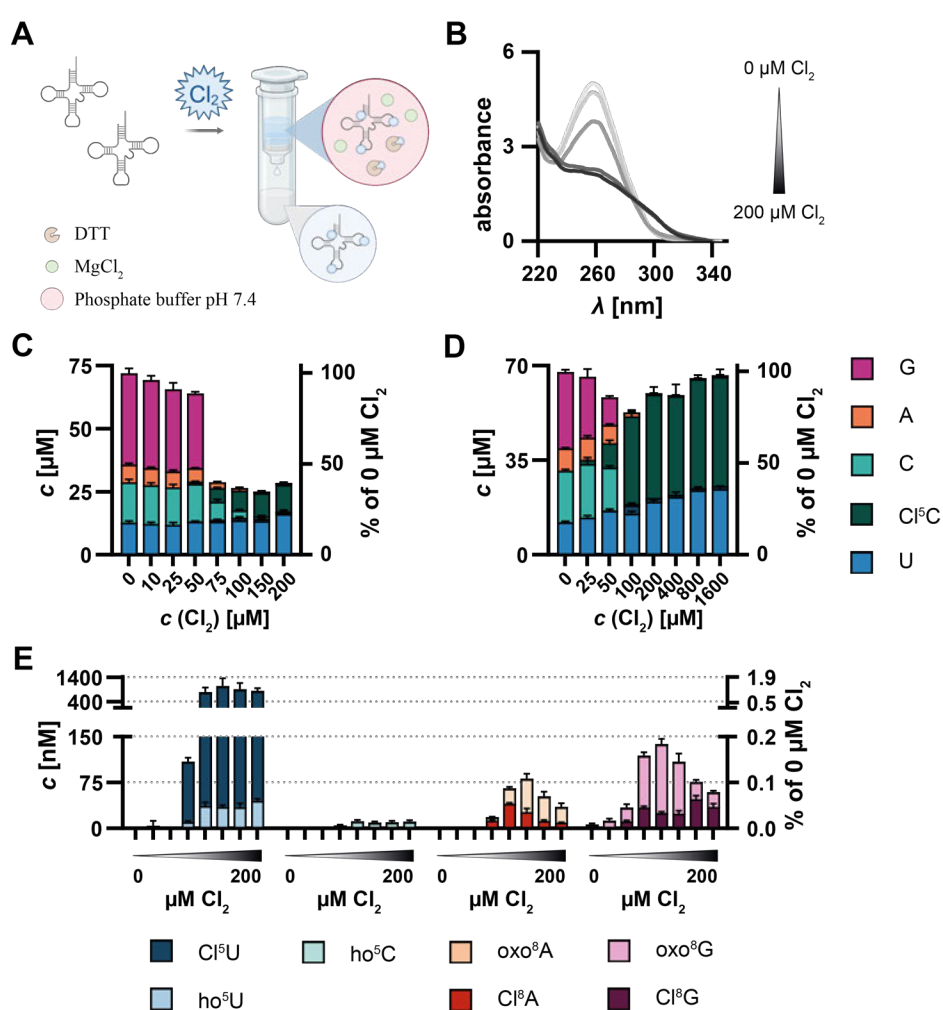


Figure 26. LC-MS/MS quantification of oxidized nucleosides derived from IVT-tRNA^{Asp} and an unmodified oligonucleotide.

A Schematic illustration detailing an RNA oxidation experiment including subsequent purification steps removing any salts and buffer components prior LC-MS/MS analysis. Created with Biorender.com (2024). **B** Absorbance spectra of oxidized IVT-tRNA^{Asp} at varying Cl_2 concentrations of 0, 25, 50, 100, and 200 μM . **C – E** LC-MS/MS quantification of oxidized IVT-tRNA^{Asp} (**C**) and an unmodified oligonucleotide (**D**). Absolute quantities of nucleosides are depicted in micromolar concentration as initially present in oxidation reactions correlated to increasing oxidant concentrations. The right y-axis indicates relative quantities related to total nucleosides present in 0 μM Cl_2 control. **E** Displayed are oxidation products of IVT-tRNA^{Asp} corresponding to **C** present in nanomolar concentrations ($\text{Cl}^{\text{F}}\text{C}$ not depicted here). 50 ng sample was injected

following enzymatic digestion down to nucleosides. Absolute quantification utilized calibration curves of external standards. Mean values ($n = 3$) \pm SD are indicated.

In Figure 26C, absolute quantities of nucleosides derived from oxidized IVT-tRNA^{Asp} are represented, showing parent and oxidized nucleosides in micromolar concentrations on the left y-axis and the proportion of nucleoside compared to untreated control on the right y-axis. Uridine (blue), cytidine (green), and adenosine (orange) concentrations remained relatively constant up to 50 μ M Cl₂ while guanosine (pink) steadily declined within that range and became undetectable at higher concentrations. Notably, Cl⁵C levels surpassed those of guanosine to the extent that they were indistinguishable in the UV trace, preventing guanosine detection, particularly at low guanosine concentrations and high Cl⁵C concentrations. Consequently, quantification of guanosine was unfeasible at 75 μ M and 100 μ M Cl₂. Further exploration regarding this matter is detailed in Chapter 8.2.1 addressing LC-MS/MS method optimization. As observed for nucleosides and binary oligonucleotides (Chapters 8.3 and 8.4), Cl⁵C (dark green) emerged at the expense of cytidine, while uridine levels remained relatively stable. Adenosine and guanosine experienced consumption at moderate Cl₂ concentrations of 75 to 100 μ M. Additionally, Inosine was detected in relevant concentrations ending in a maximum of 15% to 20% of initially present adenosine and shown in Figure S10 for IVT-tRNA^{Asp}, the unmodified oligonucleotide, and binary oligonucleotides.

Figure 26D presents another example depicting absolute quantities of an oligonucleotide oxidized across a wider Cl₂ concentration range covering 0 to 1600 μ M Cl₂. At 50 μ M Cl₂, reductions in guanosine, adenosine, and cytidine were evident, with Cl⁵C formation already observed concurrently. Unlike the findings shown in Figure 26C, the ratio of purine to pyrimidine species predominantly shifted towards pyrimidines, notably uridine, and Cl⁵C, particularly evident at the highest Cl₂ concentrations. A possible explanation for the observed differences lies in the method for RNA quantification before LC-MS analysis, which relied on Nanodrop absorbance measurements. The presence of abasic sites significantly disrupted these absorbance values leading to an overestimation of pyrimidine content. This is because abasic sites were primarily found in purines lacking the chromophores, as discussed in Chapter 8.4.2. The impact of abasic sites on absorbance measurements was further emphasized by the quantity of oxidized nucleosides shown in Figure 26E, which corresponds to the experiment detailed in Figure 26C. The left y-axis denotes nanomolar concentrations, while the x-axis represents oxidant concentrations with the relative ratio shown on the right y-axis. Quantities of 5-hydroxypyrimidines (ho⁵U in light blue, ho⁵C in light green) and 5-chloropyrimidines (Cl⁵U in dark blue, Cl⁵C in dark green shown in Figure 26C) exhibited consistent increases reaching a plateau. In contrast, a maximum was observed for 8-oxo- and 8-chloropurines constituting less than 1% of initially present nucleosides pointing to alternative oxidation products such as abasic sites. Alternative guanosine oxidation products as already investigated in Chapter 8.3.4 are depicted in Figure S11.

In conclusion, LC-MS/MS quantification of oxidation products in RNA revealed dynamic changes in the abundance of pyrimidines and purines. Increasing oxidant concentrations led to a concentration-dependent formation of oxidation products such as chlorinated and oxygenated nucleosides. Guanosine emerged as the predominant target of oxidation, acting as a scavenger for other nucleosides, particularly evident in the case of Cl⁵C. While Cl⁵C was detected at 25 μ M Cl₂ in nucleoside oxidation experiments (see Chapter 8.3), its appearance within an RNA molecule occurred only after guanosine consumption at 50 μ M or 75 μ M Cl₂. Absolute quantification showed that the total of parent pyrimidine nucleoside and its C5-substituted oxidation product reached approximately 100% of initially present nucleosides, whereas purines yielded less than

1%. Our findings also indicated the formation of dimers at adenosine residues considering the results presented in Chapter 8.3.2, alternative oxidation products at guanosine residues (Chapter 8.3.4) and abasic sites (see Chapter 8.4.2). As no external standards were available for these oxidized lesions, absolute quantification was not possible but would allow the estimation of their abundancies and a better understanding of their potential *in vivo* relevance. The total RNA extracted from *S. c.* was subjected to identical analysis, which revealed a comparable pattern of quantities for the parent nucleosides and their oxidation products (see Figure S12).

During LC-MS analysis, we observed that the injected amount of oxidized RNA per molecule was biased due to the presence of abasic sites preferentially located at purine bases as discussed in Chapter 8.4. Thus, abasic sites did not contribute to absorbance-based RNA concentration determination. This resulted in an apparent increase in pyrimidines and posed challenges in normalization, as the determined concentration did not accurately represent RNA molarity. While normalization is typically conducted by relating the absolute amount of modification to a single nucleoside such as adenosine,¹⁰⁴ the fluctuation in the quantity of parent nucleosides upon oxidation made normalization challenging. Although uridine was largely unaffected by applied oxidation conditions, normalization to uridine led to masking of increased pyrimidine proportions which serve as indirect markers for abasic sites. However, omitting normalization steps does not correct pipetting and technical errors.

Comparison of the present findings with existing literature revealed that research into oxidative damage has expanded to encompass not only DNA but also RNA, investigating the involvement of oxidized nucleosides in inflammation-associated cancer diseases and inflammatory processes.^{37,46} The functional integrity of RNA critically depends on its base pairing ability, giving modifications on the Watson-Crick interface significant impacts, such as those caused by oxidized nucleosides. These oxidized sites can lead to miscoding between tRNA and mRNA or disrupt other processes involving RNA base pairing.^{37,44} Among oxidized nucleosides, oxo⁸G is of particular significance as an RNA lesion worthy of further investigation. Its ability to induce cellular damage is emphasized by the presence of several repair enzymes within human cells and its role as an epitranscriptional modification. Notably, oxo⁸G serves as an effector for various regulatory mechanisms involving writer, eraser, and reader proteins implicated in stress regulation.⁴⁵ Chlorinated nucleosides have gained significant attention in studies focusing on immune response and inflammatory diseases primarily in DNA.^{46,52,60} Their mutagenic potential is initiated by mispairing during nucleoside-protein or nucleoside-nucleoside interaction and therefore very likely to occur not only on DNA but also on RNA.^{52,55,56,60,67,141,142}

The diverse and incomplete picture of RNA oxidation in the current literature highlights the need for further investigation into oxidized nucleosides. A comprehensive understanding of these complex mechanisms is essential for estimating their damaging effects *in vivo* and their potential contribution to pathophysiological circumstances and disease progression.

8.6 Sequencing of oxidized RNA

8.6.1 Next-generation sequencing (NGS) method development utilizing synthetic oligonucleotides

In order to further investigate the effects of oxidative stress on RNA, a high-throughput sequencing (NGS) method sensitive to oxidation products was developed. This part of the project was conducted in close collaboration with the [REDACTED] lab in Nancy and their PhD student, [REDACTED]. Oxidation experiments were performed in Mainz by me. The sequencing experiments including library preparation were carried out in Nancy either by myself during a stay in their lab or by [REDACTED]. [REDACTED] performed bioinformatic data analysis. Synthesis of the AP-modified oligonucleotide was performed by [REDACTED] from the group of [REDACTED], Innsbruck based on the procedure described by Küpfer *et al.* 2007.¹⁴³

This method is based on the Maxam & Gilbert sequencing approach initially invented for DNA in 1977⁸⁸ and later adapted for RNA by Peattie & Gilbert in 1980.⁸⁷ The fundamental approach of both methods involves the chemical treatment of nucleic acids, for example, by dimethyl sulfate (DMS) which methylates nucleosides such as guanosine at position 7 resulting in 7-methylguanosine (m⁷G). Specifically, methylated nucleosides are weakened at their *N*-glycosidic bond, making them susceptible to reactions with nucleophiles such as hydroxyl ions or amines leading to bond cleavage.^{122,143} The resulting abasic (AP) sites are then targeted by hot pyrimidine in DNA or aniline in RNA leading to strand cleavage. These site-specific cleavages can then be utilized for mapping-based detection approaches. Modern developments of the Maxam & Gilbert technique have adapted the knowledge of nucleoside-specific strand cleavage for the detection and mapping of naturally occurring modified sites such as m⁷G or 3-methylcytidine (m³C) in RNA by NGS. One such application is the AlkAniline-Sequencing (AAS) protocol established by the [REDACTED] lab in Nancy, France.¹²⁰ This approach utilizes the combination of AP site generation by alkaline hydrolysis at specific modified sites followed by aniline-induced chain scission at AP sites to map modifications accessible via this protocol. Successfully mapped nucleosides include m⁷G, m³C, and 5-hydroxycytidine (ho⁵C). The finding that ho⁵C is accessible via AAS served as a motivation to apply the protocol to oxidatively damaged RNA.

More precisely, three oligonucleotides with identical sequences with either guanosine, oxo⁸G, or an AP site incorporated at a defined position were synthesized and subjected to AAS analysis. Results achieved from synthetic oligonucleotide data were subsequently applied to *in vitro* transcribed tRNA^{Asp} (IVT-tRNA^{Asp}) and extracted *S. c.* total RNA.

Figure 27A depicts a scheme of the AAS protocol for guanosine, oxo⁸G, and an AP site. In the first step (1.), alkaline hydrolysis is performed creating AP sites at nucleosides with weakened *N*-glycosidic bonds such as oxo⁸G but not guanosine. Additionally, this step fragments particularly long RNA species making them compatible for Illumina sequencing. Guanosine and AP sites remain unchanged by alkaline hydrolysis. In the next step, thorough dephosphorylation (Figure 27A, step 2a.) is carried out removing all present phosphates (shown in blue) in RNA molecules. The complete removal of all phosphate groups is crucial as it is a prerequisite for subsequent aniline cleavage. Aniline (Figure 27A, step 2b.) reacts with AP sites as well as ring-opened or non-aromatic nucleosides leading to strand scission via a Schiff base initiating β -elimination and

generating new 5'-phosphates (depicted in green) in the 3'-fragments (see last step). Due to the preceding removal of all native phosphate groups, the location of the generated 5'-phosphates is limited to the N+1 nucleotide of AAS-sensitive residues enabling adapter ligation at this position. This results in high specificity and sensitivity during downstream bioinformatic analysis.^{120,144}

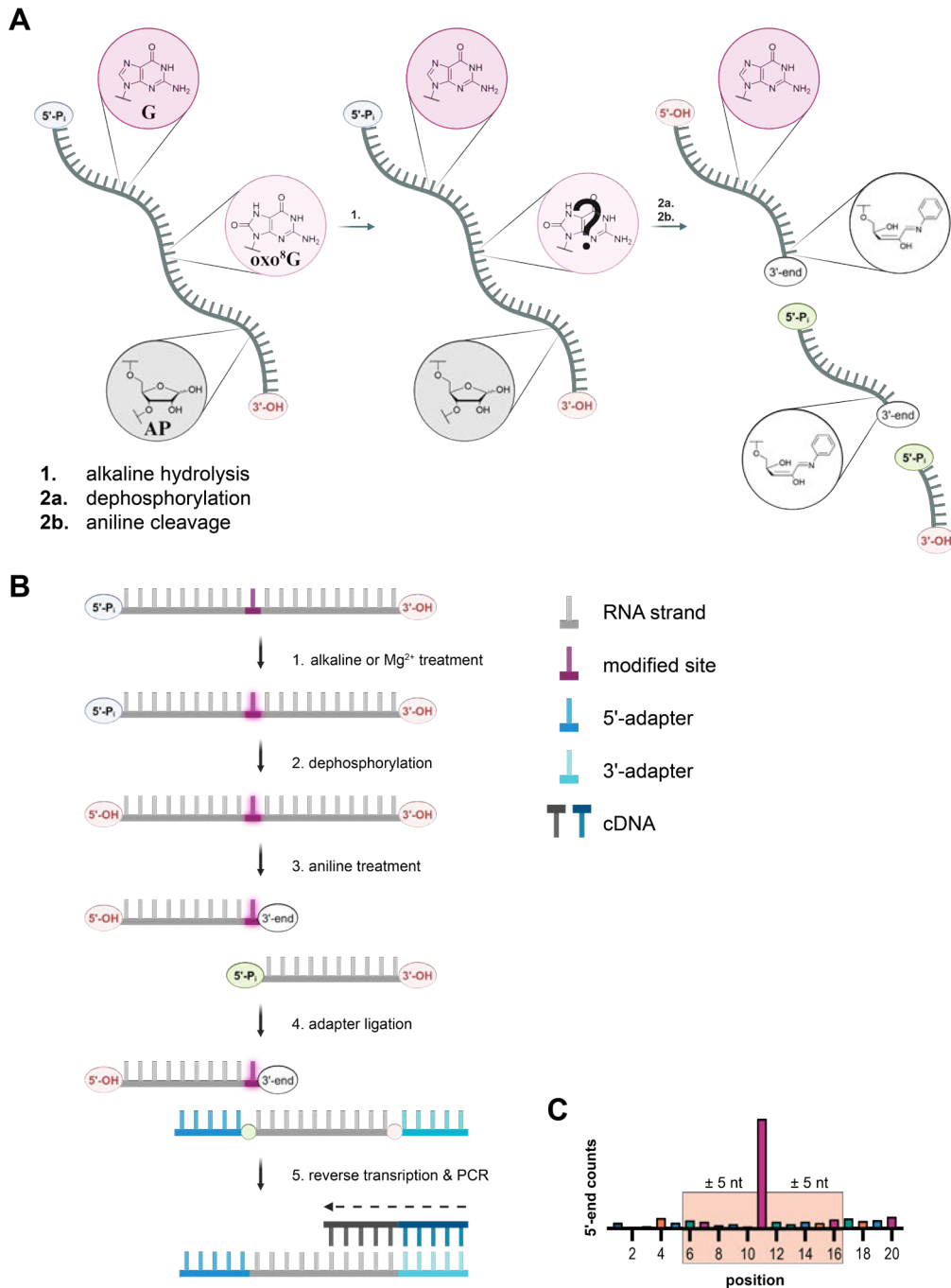


Figure 27. Schematic illustration of the AlkAniline-Sequencing protocol exemplified for guanosine (G), oxo⁸G and an abasic (AP) site.

A An RNA molecule containing an unmodified G (top), an oxo⁸G (middle) and an AP (bottom) site within its sequence is depicted including the native 5'-phosphate (blue) and the 3'-OH (red) group. In the first step, alkaline hydrolysis is performed affecting only specific nucleosides such as m⁷G or oxo⁸G followed by thorough dephosphorylation to remove all 5'-phosphates. Subsequent aniline treatment initiates cleavage of the RNA strand at position N+1 relative to modified

sites resulting in new 5'-phosphates (green). These site-specific phosphate groups serve as entry point for adapter ligation allowing the mapping of modified sites based on their N+1 position. **B** Library preparation protocol for AlkAniline-sequencing. 1. Alkaline hydrolysis or Mg^{2+} treatment is followed by 2. dephosphorylation and 3. aniline-induced strand cleavage. Aniline cleavage results in two RNA fragments: the 5'-fragment which contains the aniline adduct responsible for strand cleavage and lacks any 5'-phosphate groups and the 3'-fragments which holds a newly generated 5'-phosphate serving as a site-specific entry point for adapter ligation (4.) at the N+1 position relative to the initially modified site. The ligated RNA fragments are then subjected to reverse transcription and polymerase chain reaction (PCR) amplification (5.) before Illumina sequencing. **C** Graph illustrating the calculation of normalized G counts (NormGcount). Counts at a given position x are normalized to the median within the 11-nucleotide window (position $x \pm 5$ nucleotides) highlighted in the orange box. Created with Biorender.com (2024). Figure adapted from Motorin *et al.* 2024.¹⁴⁴

The entire procedure is also provided in Figure 27B as an overview of the above-mentioned steps differentiating native 5'-phosphates (blue) and newly generated 5'-phosphates (green) which serve as unique entry points for adapter ligation. The protocol included 1. alkaline hydrolysis or Mg^{2+} treatment, 2. dephosphorylation of native phosphate groups, 3. aniline-induced strand cleavage, 4. adapter ligation, 5. reverse transcription (RT), polymerase chain reaction (PCR) amplification, and Illumina sequencing. Mg^{2+} treatment was used in the first step instead of alkaline hydrolysis to differentiate AP sites from oxidized nucleosides as a variation of the standard AAS protocol. Mg^{2+} induces fragmentation of long RNAs but does not hydrolyze weakened *N*-glycosidic bonds as alkaline hydrolysis does. Consequently, signals detected only after Mg^{2+} treatment and not after alkaline hydrolysis in the first step are caused by oxidized nucleosides other than oxo⁸G such as preexisting AP sites. Finally, bioinformatic analysis counts the number of reads starting at the N+1 position and normalizes these counts to the median within an 11-nucleotide window (see Figure 27C). Additionally, counts at G residues are excluded due to their predominant reactivity during oxidation, therefore the score was referred to as normalized G count (NormGcount).

Figure 28A shows NormGcounts for the G-, oxo⁸G- and AP-modified oligonucleotides at each position after alkaline (left) and Mg^{2+} treatment (right) following the procedure shown in Figure 27B. The unmodified oligonucleotide (top panels) did not reveal any signals above background level, whereas the corresponding oxo⁸G- (middle panel) and AP-modified oligonucleotides (bottom panel) showed increased NormGcounts at position 16. Initial alkaline hydrolysis resulted in a NormGcount of 180 for the oxo⁸G site and reached 14,800 for the AP site. Data obtained from Mg^{2+} treatment reduced the oxo⁸G-derived signal to 50 indicating a lower quantity of aniline-induced strand cleavage. Conversely, the NormGcount in the AP-modified oligonucleotide slightly increased. To identify the product formed from oxo⁸G after alkaline hydrolysis, the oxo⁸G-modified oligonucleotide was hydrolyzed under AAS conditions in bicarbonate buffer (pH 9.2) and subsequently labeled with the fluorescent aldehyde-reactive probe (ARP) as described in Chapter 10.2.17. Figure 28B shows the corresponding denaturing gels after alkaline hydrolysis (i.) and subsequent ARP labeling (ii.). Comparison of the oxo⁸G-modified control sample (i., lane 2) with the water-treated (i., lane 3) and alkaline-treated sample (i., lane 4) revealed increased degradation resulting from the 45-minute incubation at 96°C, with no visual difference between lane 3 and 4. Subsequent detection of AP sites via ARP labeling (ii.) did not reveal any fluorescent signals (ii., left gel, marked in a green box) in either the water-treated (ii., lane 1) or alkaline-treated sample (ii., lane 2) while bands were still detectable upon GelRed staining (ii., right gel). This observation does not confirm the generation of AP sites after alkaline hydrolysis at oxo⁸G sites, instead suggesting an alternative nucleoside is generated upon hydrolysis responsible for aniline-induced strand cleavage.

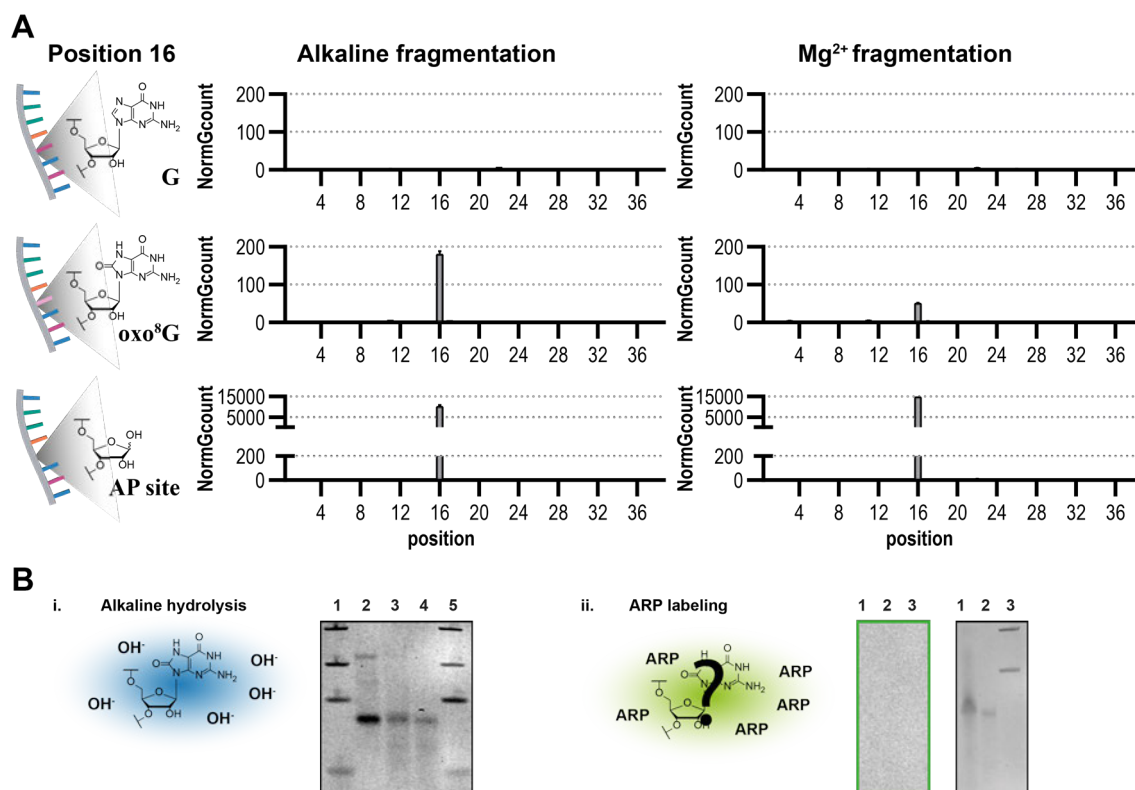


Figure 28. Comparing signals resulting from the AlkAniline-sequencing protocol comparing alkaline and magnesium fragmentation on three oligonucleotides including either G, oxo⁸G, and an abasic (AP) site at position 16.

A Graphs show Normalized G counts (NormGcount) for each position. Alkaline treatment resulted in signals for the oxo⁸G- and the AP-modified oligonucleotide, whereas no signal was detectable for the unmodified version. NormGcounts reached 180 at the oxo⁸G site and were about 56-fold increased in the corresponding AP-modified 38mer upon initial alkaline treatment. Replacing alkaline with Mg²⁺ fragmentation led to a decreased NormGcount of 50 at the oxo⁸G site and a slightly increased one in the AP-modified 38mer (NormGcount = 14761). Created with BioRender.com (2024). **B** The oxo⁸G-modified 38mer was treated with either ultrapure water (lane 3) or 10 mM bicarbonate buffer pH 9.2 (lane 3) according to the alkaline hydrolysis performed during AAS for 45 minutes at 96°C and analyzed on a 15% denaturing PAGE (**i**). Lane 1 and 5 include ladders (visible are 200, 100, 50 and 20 base pairs from top to bottom), lane 2 includes the 38mer control. Slightly degraded bands are visible for the incubated samples in lane 3 and 4. In a second step, samples were labeled with the ARP reagent to detect generated AP sites and analyzed via denaturing PAGE (**ii**). The fluorescent (left gel in green box) and GelRed scan (right gel in black box) of the hydrolyzed and ARP-labelled 38mer show the water-treated control in lane 1 and the 10 mM bicarbonate buffer pH 9.2 treated sample in lane 2. Lane 3 shows the 100 and 50 base pairs of a ladder. No signals were detectable in the fluorescent scan, whereas bands were still visualized via GelRed staining. Gels were run for 2 h at 18 W and 7 pmol was loaded for every sample.

8.6.2 Investigating the AAS protocol on structurally folded and oxidized IVT-tRNA^{Asp}

A first application of this protocol was performed on folded IVT-tRNA^{Asp} oxidized at various Cl₂ concentrations. The results of AAS are presented in Figure 19A after initial alkaline hydrolysis. The modified AAS protocol with initial Mg²⁺ treatment was also performed, but the results show negligible differences at 100 μM Cl₂ concentrations (graph shown in Figure S13A). Therefore, the following section focuses on the results

obtained from the standard AAS protocol utilizing initial alkaline hydrolysis. The graph in Figure 29A shows superimposed data of 0 μM (gray), 25 μM (light red), 50 μM (red), and 100 μM (dark red) Cl_2 -oxidized tRNA. Prominent signals were exclusively detected at G residues specifically at positions 18, 20, 34, 45, 56, and 67. The highest signal was detected at G18 (NormGcount_{25 μM} = 391, NormGcount_{50 μM} = 912) with the maximum observed after 50 μM Cl_2 oxidation. Other prominent signals at position 20, 34, 45 and 56 ranged between 50 and 100 with the highest values at moderate 50 μM Cl_2 oxidation. Although G67 also showed a signal in AAS, the highest NormGcount of 59 was observed in the untreated control, suggesting that the reactivity at this site is due to an alternative effect. The results of the absolute quantification of oxo⁸G and relative quantification of other guanosine G oxidation products via LC-MS/MS are presented in Figure 26D and Supplementary Figure S13B. At 50 μM Cl_2 , parent nucleosides were still detectable alongside the emergence of oxidation products. These oxidation products, including oxo⁸G, rGh, and rSp, reached their maximum abundances at 100 μM Cl_2 . This indicates, that the AAS protocol is most effective when applied to RNA molecules containing moderate or low levels of oxidized sites while maintaining overall structural integrity. Mapping these results onto the secondary cloverleaf structure of tRNA^{Asp} (Figure 29B) revealed that reactive guanosine residues were exclusively located in loop regions and were not involved in Watson-Crick base pairs indicating structural effects of oxidation on RNA.

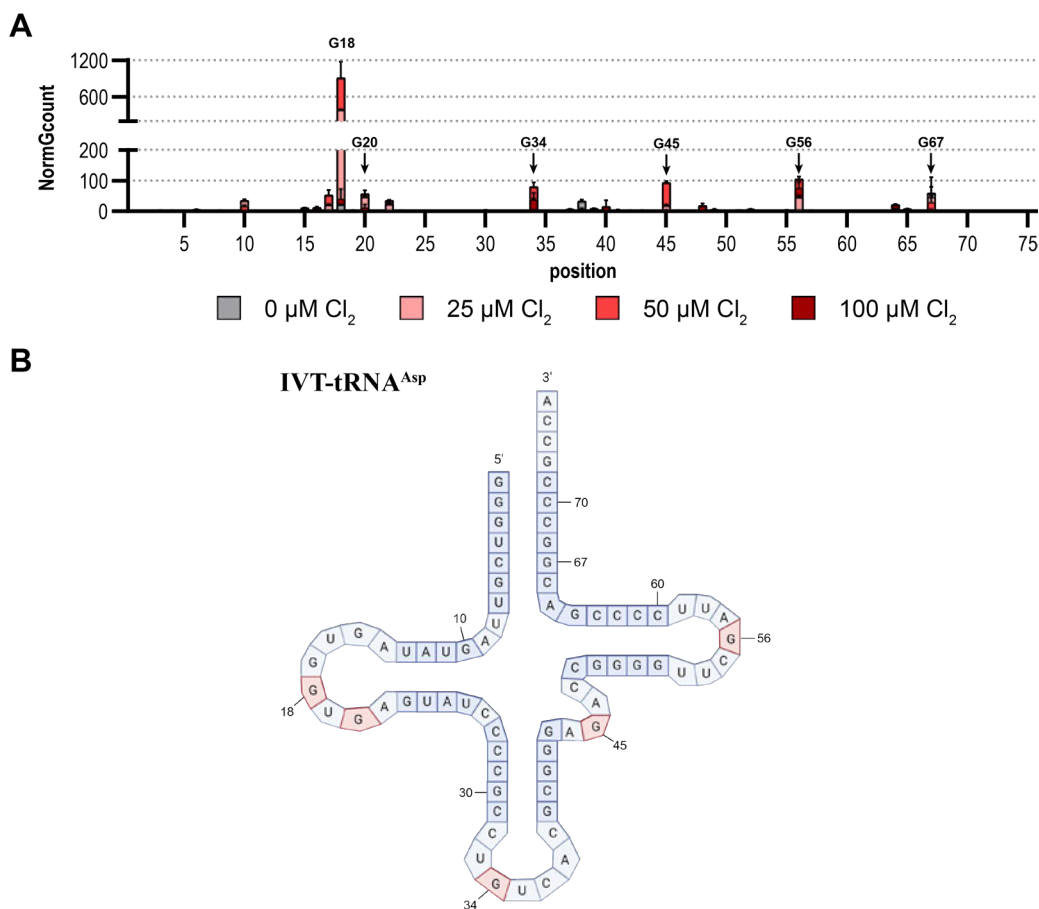


Figure 29. AAS was performed on folded *in vitro* transcribed tRNA^{Asp} revealing prominent signals exclusively at G residues.

A The graph shows superimposed NormGcounts for 0 μM (gray), 25 μM (light red), 50 μM (red), and 100 μM (dark red) Cl_2 -oxidized tRNA. Major signals were detected at positions 18, 20, 34, 45, 56 and 67 being exclusively G residues.

NormGcounts for these residues: 0 μM Cl_2 : G67 = 59; 25 μM Cl_2 : G18 = 391, G34 = 40, G45 = 19, G56 = 47; 50 μM Cl_2 : G18 = 912, G34 = 80, G45 = 93, G56 = 105; 100 μM Cl_2 : G18 = 42, G34 = 39, G45 = 3.5, G56 = 79. Sequencing experiments were performed on three independent experimental replicates ($n = 3$). Indicated are mean values \pm SD. **B** Reactive sites mapped onto the cloverleaf structure of tRNA^{Asp}. All sites are located in loop regions indicating structural impacts on oxidation reactions. Created with BioRender.com (2024). Created with BioRender.com (2024).

Our application of the AlkAniline-Sequencing (AAS) protocol to oxidized RNA successfully detected oxidation products of guanosine including oxo⁸G and AP sites. To validate the AAS method, we used synthetic oligonucleotides containing either guanosine, oxo⁸G, or an AP site within an otherwise identical sequence. Both types of oxidized lesions produced detectable signals for mapping purposes, with AP sites generating the most robust signals. This result aligns with the underlying chemistry from the Maxam & Gilbert sequencing method^{87,88} which relies on AP site formation for subsequent strand cleavage and sequencing. Conversely, oxo⁸G yielded comparatively weaker signals, suggesting less efficient strand cleavage following alkaline hydrolysis and aniline treatment.

In adapting the standard AAS protocol, we replaced the initial alkaline hydrolysis with Mg^{2+} treatment to differentiate oxo⁸G from AP sites. This modification was motivated by the fact that aniline-induced strand cleavage directly targets natural AP sites but not oxo⁸G. A direct comparison of both procedures on synthetic oligonucleotides containing oxo⁸G or AP residues revealed a decrease in NormGcounts for oxo⁸G and an increase for AP sites under Mg^{2+} treatment compared to alkaline treatment. This observation can be attributed to differences in the random cleavage rates induced by hydroxyl and Mg^{2+} ions, as their yields likely vary. Such random cleavages contribute to background signals, which are accounted for during normalization and calculation of NormGcounts. Lower background noise results in higher NormGcounts, potentially explaining the increased NormGcounts observed in the Mg^{2+} -treated AP-modified oligonucleotide. Based on the chemistry affecting oxo⁸G during alkaline or Mg^{2+} treatment, the NormGcount for oxo⁸G was expected to disappear nearly completely after Mg^{2+} treatment if AP sites were generated upon alkaline hydrolysis. However, ARP labeling experiments excluded AP sites as hydrolysis products, suggesting the presence of an alternative oxo⁸G-derived nucleoside. This alternative product may contribute to the Mg^{2+} -derived signals in the oxo⁸G-oligonucleotide by stabilizing or coordinating transition states¹⁴⁵ during aniline cleavage. Additionally, trace amounts of oxidized oxo⁸G nucleosides, being sensitive to aniline, may be responsible for the observed signal. The sensitivity of various guanosine oxidation products, including open-ring hydantoins towards aniline cleavage in RNA has been investigated by Fleming *et al.*¹⁴⁶ showing, that efficient and partly quantitative strand scission is achieved. Furthermore, the analysis of the obtained reverse transcription (RT) signatures, as shown in Figure S14, provides insights into the identity of the initial nucleoside responsible for the resulting signal. Both AP and oxo⁸G residues preferentially base pair with adenosine in the corresponding cDNA, providing additional clues to the initial oxidized lesion.¹⁴⁷⁻¹⁵⁰

Our first application of the AAS protocol on oxidized IVT-tRNA^{Asp} showed that only moderate Cl_2 concentrations were suitable for sequencing analysis, as highly damaged RNA was incompatible with reverse transcription (RT) and therefore downstream bioinformatic analysis. Detected signals were mostly observed at guanosine residues oxidized with 50 μM Cl_2 . Differentiating between oxo⁸G and AP sites was only successful for the synthetic oligonucleotide, not for oxidized IVT-tRNA^{Asp} containing numerous oxidation products on one RNA molecule. Given the complex and dynamic nature of these guanosine oxidation products, as described in mass spectrometry analysis (Chapter 8.3.4), definitive conclusions about the specific oxidized nucleoside lesion

responsible for the AAS signal cannot be drawn solely based on the comparison of NormGcounts after alkaline and Mg^{2+} treatment. Since oxidized guanosine sites were exclusively found in loop regions, it suggests that oxidation occurs in a structure-dependent manner. However, a direct comparison between native and denatured conditions has not yet been conducted. Further investigations are recommended to better understand the impact of RNA structure on oxidation events and sequencing outcomes.

Current literature on methods for detecting oxo⁸G or AP sites in RNA includes antibody-based pulldown protocols for oxo⁸G^{42,151,152} and NGS-based protocols. These approaches involve combinations of immunoprecipitation (IP) coupled with sequencing in DNA^{45,153} as well as selective chemical derivatization of oxo⁸G followed by biotinylation and streptavidin pulldown.⁴⁵ Another technique involves the enzymatic generation of AP sites from oxo⁸G which are then used for Illumina sequencing in both DNA^{45,92} and RNA.^{45,79} In the realm of these protocols, the described AAS method benefits from its utilization of site-specific 5'-phosphates contributing to high sensitivity, which is particularly crucial when investigating low-abundance modified or damaged nucleosides.

In summary, the established protocol effectively analyses low-abundant oxidized sites on RNA molecules while also providing insights into the structural context of these sites. This dual capability is highly valuable in a biological context, as damaged sites are typically low in abundance, yet their presence can significantly impact or induce structural changes, which may trigger molecular repair mechanisms

9 CONCLUSION AND PERSPECTIVES

The present study was designed to gain a deeper insight into the effects of oxidative stress on RNA. While the impact of oxidative stress on DNA has been extensively studied, RNA has not received as much attention. However, given its role as an intermediate between DNA and proteins, RNA is a central component whose integrity is of essential importance.¹⁻³

The protection of DNA against oxidative stress is facilitated by its complexation with proteins, its localization in the nucleus, and its double-stranded structure. In contrast, RNA is primarily located in the cytosol, where the majority of oxidative processes occur, and it naturally forms diverse structures that include single-stranded regions.¹⁵⁴ In comparison to DNA, RNA is a transient molecule with a half-life of three to seven days¹⁵⁵ as observed for tRNA and rRNA and playing a role in a multitude of cellular processes such as mRNA translation. As numerous translation processes are dependent on single tRNA or rRNA molecules, the downstream impact of these damaged molecules is amplified.

To address this issue, the experimental work presented in this thesis was designed to analyze oxidative stress at a molecular level. One objective was to identify damaged nucleosides and quantify them in response to increasing oxidant concentrations. The *in vitro* analysis demonstrated a notable sensitivity towards alterations in RNA and oxidant concentrations as well as the presence of additional components. Furthermore, the ratio between oxidant and reactive sites was found to be dependent on the number of reactive sites on nucleobases rather than being correlated to the concentration of RNA molecules. To overcome this obstacle, RNA concentrations were calculated as mass rather than as moles per volume only which yielded comparable results for different RNA species.

The initial identification and analysis of oxidized nucleosides was conducted using the standard LC-MS/MS method which was then adapted for the analysis of polar nucleosides with respect to the pH value, buffer concentration, and gradient composition. Nevertheless, some alternative guanosine oxidation products still eluted within the dead volume of the HPLC system indicating that further investigation are necessary. The latter may include the replacement of the lipophilic RP-18 column with a more hydrophilic alternative as a HILIC column and optimizations of the HPLC and MS methods such as pH, flow rate, and ion source-specific parameters. The subsequent objective is to quantify these oxidation products which will require the preparation of an external standard as well as a stable isotope-labeled internal standard (SILIS). One potential approach is to collect the corresponding fractions after HPLC separation, perform purification, and utilize them as external standards. Quantifying the formed oxidation products is essential for drawing conclusions about the extent of potential damage in a biological system. This is particularly important given that the signal intensity derived from LC-MS/MS depends on the ionization efficiency and other instrumental and sample-specific parameters which prevents conclusions about the absolute quantity.

The absolute quantification of adenosine and guanosine species was primarily based on the declining concentrations of parent nucleosides, as their 8-oxo- and 8-chloro-purine derivatives accounted for only approximately 1% of the total while the adenosine and

guanosine were no longer detectable at corresponding oxidant concentrations. Alternative oxidation products for guanosine were identified to a certain extent through the use of isotopically labeled nucleosides. However, further research is necessary to elucidate the oxidation products of adenosine. The preliminary findings of this study yielded several promising results, including the potential formation of dimers between two adenosine derivatives and the formation of inosine. The next steps may include the utilization of isotopically labeled adenosine which could provide a more detailed insight into the structural composition of these dimers. Additionally, the use of alternative analytical techniques such as nuclear magnetic resonance (NMR) or high-resolution mass spectrometry (HRMS) may be employed. In this context, the availability of external standards would again permit absolute quantification and an estimation of their abundance similar to previously discussed guanosine oxidation products.

The two pyrimidines, uridine and cytidine exhibited comparatively less complex oxidation reactions. While uridine remained largely unaltered under the applied conditions, cytidine underwent a quantitative oxidation to 5-chlorocytidine resulting in the recovery of 100% of the initially present parent nucleoside. In summary, the reactivities of nucleosides were found to decrease in the order of guanosine, adenosine, cytidine, and uridine, with the latter being the least susceptible. This observation was also corroborated in the analysis of binary oligonucleotides composed of only two nucleosides.

Oxidation did not only result in the formation of oxidized nucleosides but also in the complete removal of the nucleobase from the ribose, thereby generating abasic sites. To analyze these abasic sites and the integrity of the RNA backbone, fluorescent labeling and ^{32}P -labeling of the RNA's 5'-end were employed. The results demonstrated that the ribose-phosphate backbone remained intact upon oxidation, though conventional nucleic acid staining was unsuccessful. The high prevalence of abasic sites was the primary factor impeding the intercalation of the dye which was attributed to the absence of planar stacked nucleobases. As previously discussed, the quantification of these sites is crucial for a more comprehensive understanding and estimation of their impact, particularly given their high reactivity in forming inter- and intramolecular cross-links.

Another objective of this PhD thesis was to develop a sequencing protocol to facilitate the mapping of oxidized guanosine species including abasic sites. This protocol is based on the AlkAniline-Sequencing (AAS) approach¹²⁰ and the susceptibility of oxidized guanosines and abasic sites to aniline-induced strand scission.¹⁴⁶ At this point of the study, the differentiation between potential guanosine oxidation products remained unresolved as synthetic oligonucleotides were unavailable for modified sites other than oxo⁸G and the abasic site. Nevertheless, some assumptions may be made by considering the resulting RT signatures and the behavior upon alkaline and Mg^{2+} treatment. In particular, oxo⁸G only produced quantitative signals after alkaline hydrolysis, but not after initial Mg^{2+} treatment. In contrast, abasic sites and some alternative guanosine oxidation products did not require initial alkaline hydrolysis and demonstrated direct sensitivity to aniline chain scission. In order to definitively identify the underlying oxidized guanosine species, it is essential to analyze the specific sequencing outcomes for each oxidation product by comparing alkaline and Mg^{2+} treatment followed by aniline cleavage. Despite these challenges, oxidized guanosine species can be mapped and assumptions regarding their identities can be made.

Other NGS methods have been published for the detection of oxo⁸G or abasic sites, although they are primarily applied to DNA.^{45,90-94} Despite the aforementioned limitations, the distinctive utilization of the 5'-phosphate moieties for adapter ligation

in the AAS protocol represents a promising option for further investigation. The method's high sensitivity and specificity render it a favorable option for the analysis of oxidatively damaged RNA which is likely to be present only in low abundance in biological systems. The potential impact of oxidized RNA on disease development underscores the importance of further research in this field which should also include investigations of inter- and intramolecular cross-links at abasic sites.

In this study, hypochlorous acid was used as an oxidizing agent. As a consequence of its unstable nature, it was necessary to carry out regular quantification by determining the Cl_2 content. The applied method proved to be sensitive, pointing to numerous fluctuations and irregularities in the quantities of Cl_2 . Therefore, the results of the aforementioned quantification procedure should be evaluated in comparison to alternative methods such as spectroscopic approaches as described elsewhere.^{57,127} Moreover, an examination of alternative oxidizing agents would be beneficial for the purpose of differentiating between HOCl-specific and general oxidation products. In this context, the analysis of oxidation products in pathophysiological cell lines of diseases associated with oxidative stress would allow for a preliminary estimation of *in vivo* occurrences and impacts. The diseases of interest include neurodegenerative disorders, cancer, diabetes, and inflammatory conditions.^{46,52}

The dynamic and complex nature of oxidation reactions and their impact on RNA are evident as various detected effects ranging from the molecular level of oxidized nucleosides to a more global level of structural reaction dependencies. A more comprehensive understanding and evaluation of these molecular mechanisms in a biological and cellular context would facilitate the application to therapeutic or alternative fields.

10 MATERIALS AND METHODS

10.1 Materials

10.1.1 Chemicals, enzymes and kits

Table 1. Chemicals, enzymes and kits used for conducting experiments described in this PhD thesis.

¹³ C guanosine	Silantes, Munich, Germany
¹⁵ N guanosine	Silantes, Munich, Germany
³² P- ATP	Hartmann Analytics, Germany
5-chlorocytidine (Cl ³ C)	BIOLOG, Bremen, Germany
5-chlorouridine (Cl ³ U)	Santa Cruz Biotechnology, Dallas, USA
5-hydroxycytidine-5'-triphosphate (ho ³ CTP)	tebubio, Offenbach, Germany
5-hydroxyuridine (Cl ³ U)	Biosynth Ltd, UK
8-chloroadenosine (Cl ³ A)	BIOLOG, Bremen, Germany
8-chloroguanosine (Cl ³ G)	BIOLOG, Bremen, Germany
8-oxoadenosine (oxo ³ A)	abcr, Karlsruhe, Germany
8-oxoguanosine (oxo ³ G)	BIOSYNTH CARBOSYNTH, Compton, UK
Acetic acid, glacial	Honeywell, Morris Plains, USA
Acetic acid, LC-MS grade	Sigma-Aldrich, Darmstadt, Germany
Acetonitrile, LC-MS grade	Honeywell, Morris Plains, USA
Adenosine	Thermo Fisher Scientific, Dreieich, Germany
Alexa Fluor™ 488 Hydroxylamine	Thermo Fisher Scientific, Dreieich, Germany
Alkaline phosphatase from bovine intestinal mucosa	Sigma-Aldrich, Darmstadt, Germany
Ammonium acetate	Carl Roth, Karlsruhe, Germany
Ammonium acetate ≥ 99%	Sigma-Aldrich, Darmstadt, Germany
Ammonium persulfate	Carl Roth, Karlsruhe, Germany
Ammonium sulfate, (NH ₄) ₂ SO ₄	Carl Roth, Karlsruhe, Germany
AMP	Sigma-Aldrich, Darmstadt, Germany
Aniline for analysis	Merck KGaA, Darmstadt, Germany
Antarctic Phosphatase	New England Biolabs, Frankfurt am Main, Germany
ATP ≥ 90%, lyophilized	Carl Roth, Karlsruhe, Germany
Benzonase® Nuclease (> 250 U/μL)	Sigma-Aldrich, Darmstadt, Germany
Bovine serum albumine (BSA)	Thermo Fisher Scientific, Dreieich, Germany
Chloroform ≥ 99.8%	Sigma-Aldrich, Darmstadt, Germany

Materials and Methods

CMP	Sigma-Aldrich, Darmstadt, Germany
CTP ≥ 90%, lyophilized	Carl Roth, Karlsruhe, Germany
Cytidine	Sigma-Aldrich, Darmstadt, Germany
Dichlordimethylsilane	Sigma-Aldrich, Darmstadt, Germany
di-Potassium hydrogen phosphate ≥ 99%	Carl Roth, Karlsruhe, Germany
Dithiothreitol (DTT)	Thermo Fisher Scientific, Dreieich, Germany
DNase I, RNase-free, HC (50 U/μL)	Thermo Fisher Scientific, Dreieich, Germany
dNTP mix	Thermo Fisher Scientific, Dreieich, Germany
Ethanol ≥ 99.9%	Carl Roth, Karlsruhe, Germany
Ethylenediaminetetraacetic acid (EDTA)	Carl Roth, Karlsruhe, Germany
Fast AP thermosensitive Alkaline Phosphatase (1 U/μL)	Thermo Fisher Scientific, Dreieich, Germany
FastRuler Ultra Low Range DNA Ladder	Thermo Fisher Scientific, Dreieich, Germany
Formamide	Sigma-Aldrich, Darmstadt, Germany
GelRed™ (3X)	Biotium, Hayward, USA
Glycogen, RNA grade	Thermo Fisher Scientific, Dreieich, Germany
GMP	Sigma-Aldrich, Darmstadt, Germany
GTP ≥ 90%, lyophilized	Carl Roth, Karlsruhe, Germany
Guanosine	Sigma-Aldrich, Darmstadt, Germany
HEPES ≥ 99.5%	Carl Roth, Karlsruhe, Germany
HiScribe T7 High Yield RNA Synthesis Kit	New England Biolabs, Frankfurt am Main, Germany
Hypochlorous acid (HOCl)	Thermo Fisher Scientific, Dreieich, Germany
Invitrogen Tris (1 M) pH 8.0	Thermo Fisher Scientific, Germany
Magnesium chloride hexahydrate	Merck KGaA, Darmstadt, Germany
<i>N,N</i> -Diethyl- <i>p</i> -phenylenediamine sulfate salt	Sigma-Aldrich, Darmstadt, Germany
NEBNext™ Small RNA Library Prep Set for Illumina™	New England Biolabs, Frankfurt am Main, Germany
Nuclease P1 from <i>P. citrinum</i>	Sigma-Aldrich, Darmstadt, Germany
Oligo Clean & Concentrator kit	Zymo Research Europe GmbH, Freiburg, Germany
Pentostatin ≥ 95%	Sigma-Aldrich, Darmstadt, Germany
Potassium dihydrogen phosphate ≥ 99%	Carl Roth, Karlsruhe, Germany
Potassium iodate	Carl Roth, Karlsruhe, Germany
Potassium iodide	Sigma-Aldrich, Darmstadt, Germany
RNA Clean & Concentrator-5 kit	Zymo Research Europe GmbH, Freiburg, Germany
ROTIPHORESE™ DNA sequencing system	Carl Roth, Karlsruhe, Germany
ROTIPHORESE™ 10X TBE Buffer	Carl Roth, Karlsruhe, Germany
ROTI™ Aqua-Phenol for RNA extraction	Carl Roth, Karlsruhe, Germany
Snake venom phosphodiesterase from <i>C. adamanteus</i>	Worthington Biochemical Corporation, USA
Sodium bicarbonate	Carl Roth, Karlsruhe, Germany
Sodium carbonate (anhydrous)	Carl Roth, Karlsruhe, Germany

Sodium chloride \geq 99%	Carl Roth, Karlsruhe, Germany
Sodium hydroxide pellets	VWR international GmbH, Darmstadt, Germany
Sodium hypochlorite	Thermo Fisher Scientific, Dreieich, Germany
Spermidine	Sigma-Aldrich, Darmstadt, Germany
Spermidine, trihydrochloride BioXtra, \geq 99.5%	Sigma-Aldrich, Darmstadt, Germany
Sulfuric acid, 96%	Carl Roth, Karlsruhe, Germany
T4 Polynucleotide Kinase, 500 units (10 U/ μ L)	Thermo Fisher Scientific, Dreieich, Germany
T7 RNA polymerase (20 U/ μ L)	Thermo Fisher Scientific, Dreieich, Germany
Taq DNA polymerase	New England Biolabs, Frankfurt am Main, Germany
TBE buffer, 10X	Carl Roth, Karlsruhe, Germany
TEMED	Carl Roth, Karlsruhe, Germany
Tetrahydrouridine	InSolution Merck, Darmstadt, Germany
Toluidine blue	Thermo Fisher Scientific, Dreieich, Germany
Tris*HCl	Carl Roth, Karlsruhe, Germany
Triton X-100, laboratory grade	Sigma-Aldrich, Darmstadt, Germany
Tween 20	Carl Roth, Karlsruhe, Germany
UMP	Sigma-Aldrich, Darmstadt, Germany
Uridine	Sigma-Aldrich, Darmstadt, Germany
UTP \geq 90%, lyophilized	Carl Roth, Karlsruhe, Germany
Zeba™ Spin Desalting Plates, 7K MWCO	Thermo Fisher Scientific, Dreieich, Germany

10.1.2 Consumables

Table 2. Consumables used for conducting experiments described in this PhD thesis.

Eppendorf tubes, 1.5 mL	Carl Roth, Karlsruhe, Germany
Falcon tubes, 15 mL, 50 mL	Sarstedt, Nümbrecht, Germany
Filter top vacuum bottles, PES, 0.2 μ m pore (250, 500 mL)	Sarstedt, Nümbrecht, Germany
Filtropur BT50, V25 and V50, 500 mL, 0.2 μ m	Sarstedt, Nümbrecht, Germany
Greiner UV-Star® 96 well plates	Merck KGaA, Darmstadt, Germany
Inserts, conical, clear glass, 0.1 mL	neoLab Migge GmbH, Heidelberg, Germany
Multiflex Round Tips	Sorenson Bioscience Inc., Murray, USA
Nanosep™ MF Centrifugal Devices 0.2 μ m	Pall Corporation, Port Washington, USA
Nanosep™ MF Centrifugal Devices 0.45 μ m	Pall Corporation, Port Washington, USA
Needles, Sterican	Braun, Melsungen, Germany
Parafilm™	VWR international GmbH, Darmstadt, Germany
PCR Softtubes	Biozym, Hessisch Oldendorf, Germany
Pipette tips, with filter, sterile, RNase/DNase-free	Greiner Bio-One, Frickenhausen, Germany
Polypropylene centrifugation tubes, 50 mL	Sarstedt, Nümbrecht, Germany

Reaction tubes with screw cap, 1.5 mL	Carl Roth, Karlsruhe, Germany
Scalpels B Braun™ Cutfix™	Thermo Fisher Scientific, Dreieich, Germany
Screw-cap ND9, blue, septum red rubber/PTFE beige	neoLab Migge GmbH, Heidelberg, Germany
Semi-micro cuvette, PS, transparent, 3 mL	Sarstedt, Nümbrecht, Germany
Serological Pipettes	Sarstedt, Nümbrecht, Germany
Short thread vials ND9, 1.5 mL	neoLab Migge GmbH, Heidelberg, Germany
Zeba™ Spin Desalting Plates	Thermo Fisher Scientific, Dreieich, Germany

10.1.3 Oligonucleotides

Table 3. Oligonucleotides used during this PhD thesis.

Oligonucleotide	Sequence (5' – 3')	Supplier
T7 forward primer	CGCGCGAAGCTTAATACGACTCACTATA	Biomers, Ulm, Germany
human tRNA ^{Asp} template	TGGCGGGCCGTCGGGGAATCGAACCCCGGTCTCCCGCGTGACAGG CGGGGATACTCACCACCTATACTAACGACCCCTATAGTGAGTCGTATT	IBA Lifesciences, Goettingen, Germany
T7 reverse primer tRNA ^{Asp}	TGGCGGGCCGTCG	IBA Lifesciences, Goettingen, Germany
GU binary oligomer	GGUUGUGGUGUUUGUUGGU	Biomers, Ulm, Germany
CU binary oligomer	UUCUUUCUUUCCCUUCCUUU	Biomers, Ulm, Germany
AU binary oligomer	UUUAUUUUUAAAAUUUUAAA	Biomers, Ulm, Germany
AG binary oligomer	AAAGGAAGGAAAGAAAGAA	Biomers, Ulm, Germany
AC binary oligomer	ACCAACAAACCACCACAACC	Biomers, Ulm, Germany
CG binary oligomer	CCGGCCCCCGGCCGGCGCG	Biomers, Ulm, Germany
oxo ⁸ G 38mer	UCUGAGGGUCCAGGG- oxo⁸G -UCAAGUCCUGUUCGGGCGCCA	Bio-Synthesis Inc, Lewisville, USA
unmodified 38mer	UCUGAGGGUCCAGGG- G -UCAAGUCCUGUUCGGGCGCCA	Biomers, Ulm, Germany
AP-modified 38mer	UCUGAGGGUCCAGGG- x -UCAAGUCCUGUUCGGGCGCCA x = AP site	Synthesized by [REDACTED]

10.1.4 Instruments

Table 4. Instruments used for conducting experiments described in this PhD thesis.

6470B Triple Quadrupole	Agilent Technologies, Waldbronn, Germany
Agilent 1260 Infinity (II) LC	Agilent Technologies, Waldbronn, Germany
Analytical balance	Mettler Toledo PM460 Mettler Toledo, Gießen, Germany
Beckman Avanti J25	Beckman Coulter, Krefeld, Germany
Bioanalyzer 2100	Agilent Technologies, Waldbronn, Germany
Electrophoresis Power Supply – EPS 3500XL	GE Healthcare, Buckinghamshire, UK
Electrophoresis Power Supply EPS 3501 XL	GE Healthcare, Buckinghamshire, UK
Eppendorf Centrifuge 5430R	Eppendorf, Hamburg, Germany

Eppendorf Centrifuge 5810R	Eppendorf, Hamburg, Germany
Epson Perfection V600 Photo	Epson Deutschland GmbH, Düsseldorf, Germany
Illumina NextSeq 2000	Illumina, Inc., San Diego, USA
Invitrogen™ Qubit™ 3.0	Thermo Fisher Scientific Inc., Schwerte, Germany
Jasco UV spectrophotometer V-650	Jasco Inc, Easton, USA
LSG-400-20 NA vertical chamber	C.B.S. Scientific, San Diego, USA
Model 250/2.5 power supply	BioRad, Munich, Germany
Nanodrop™ 2000 spectrophotometer	PeqLab, Erlangen, Germany
NanoDrop™ One	PeqLab, Erlangen, Germany
PAGE system, Biometra Eco-Maxi	Analytik Jena GmbH+Co. KG, Jena, Germany
pH-meter FiveEasy™ FE20	Mettler Toledo, Gießen, Germany
Pipette boy Integra	VWR, Darmstadt, Germany
Power Supply EV-Serie EV3150	Carl Roth, Karlsruhe, Germany
Qubit 3.0 fluorometer	Thermo Fisher Scientific Inc., Schwerte, Germany
Shaker (DOS-10L)	neoLab Migge GmbH, Heidelberg, Germany
Synergy Fusion RP C18 column (4 µm particle size, 80 Å pore size, 250 mm length, 2 mm inner diameter)	Phenomenex, Aschaffenburg, Germany
TapeStation 4200	Agilent Technologies, Waldbronn, Germany
Tecan Spark 10M	Tecan Group, Männedorf, Switzerland
Thermocycler peqSTAR	PeqLab, Erlangen, Germany
TriCarb™ Liquid Scintillation Analyzer 4810TR	PerkinElmer, Waltham, Germany
Typhoon TRIO+ variable mode imager	GE Healthcare, Chicago, USA
Ultrapure water purification system Milli-Q™	Millipore, Schwalbach, Germany
Vortex Mixer 7-2020	neoLab Migge GmbH (Heidelberg, Germany)
VWR Digital Heatblock	VWR International GmbH, Darmstadt, Germany

10.1.5 Software

Table 5. Software used during this PhD thesis.

Adobe Illustrator 2024 V5 (Version: 28.3)	Adobe Inc., San José, USA
Agilent MassHunter Qualitative Analysis 10.0	Agilent Technologies, Waldbronn, Germany
BioRender.com (2024)	
Bowtie2 V2.4.2, R (version 4.3.2) using the prcomb() builtin and rawVars() function as part of the matrixStats package	
ChemBioDraw Ultra 14.0	CambridgeSoft/PerkinElmer, Waltham, USA
Citavi 6	Swiss Academic Software, Wädenswil, Switzerland
FastQC	Babraham Bioinformatics (Cambridge, UK)
ggPlot2 Version 3.3.5 (RStudio Package)	Hadley Wickham, Winston Chang, <i>et al.</i> 2016 ¹⁵⁶
GraphPad Prism 8.0.1	GraphPad Software, Boston, Massachusetts USA

Materials and Methods

ImageJ V5 (Version 1.52q)

IrfanView

Microsoft Office 365

Trimmomatic V0.39

Typhoon scanner software

Wayne Rasband (Bethesda, Maryland, USA)

created by Irfan Skiljan

Microsoft, Redmond, USA

Usadel Lab, Aachen, Germany

GE Healthcare (Chicago, USA)

10.2 Methods

10.2.1 Polymerase Chain Reaction (PCR)

PCR amplification for the synthesis of tRNA^{Asp} starting from a DNA template (MH1101) was conducted in a total volume of 200 μ L. The reaction mixture included 16 mM (NH₄)₂SO₄, 67 mM Tris-HCl pH 8.8, 0.01% Tween 20, 3 mM MgCl₂, 400 μ M dNTP mix, 2 μ M of each primer and 10 nM tRNA^{Asp} PCR template. The reaction was initiated by adding 2.5 U Taq DNA polymerase and the following steps were performed using a PCR cycler: denaturation at 90°C for 2 minutes, followed by 35 cycles of annealing (30 s at 59°C), elongation (45 s at 72°C) and denaturing (30 s at 90°C). The final elongation step was prolonged to 5 minutes, followed by termination through cooling at 4°C.

10.2.2 *In vitro* transcription (IVT) of tRNA^{Asp}

IVT reactions were conducted in 1 mL containing 400 μ L crude PCR product mix, 5X T7 transcription buffer (final concentration 1X), 30 mM MgCl₂, 5 mM DTT, 5 mM ATP/CTP/GTP/UTP, and 2.5 U/ μ L BSA. The reaction was started by adding 120 U T7 polymerase and incubated at 37°C for 4 h. Finally, the DNA template was digested using 1 U DNase I, RNase-free in a final concentration of 1X DNase I buffer. Digestion was performed for 1 h at 37°C and followed by ethanol precipitation (10.2.3).

10.2.3 Ethanol precipitation

RNA precipitation was performed upon the addition of ammonium acetate (NH₄OAc) to a final concentration of 500 mM and 1 μ L glycogen (RNA grade) followed by the addition of 2.5x volume of ice-cold ethanol \geq 96%. The mixture was vortexed, spun down, and stored overnight at -20°C or at least 1 h at -80°C. Precipitated RNA was washed with 70% ethanol after centrifugation at 13000 $\times g$ at 4°C for at least 45 minutes followed by another round of centrifuging the RNA. Finally, the supernatant was removed, the pellet was air-dried and RNA was dissolved in ultrapure water. The concentration was determined on a Nanodrop One™ spectrophotometer.

10.2.4 Phenol/chloroform extraction

Samples were adjusted to a volume of 200 μ L. 100 μ L of phenol for RNA extraction and 100 μ L chloroform was added, the mixture was vortexed for 20 s and centrifuged at 10000 $\times g$ at 20°C for 10 min. The upper phase including RNA was transferred into a new tube, 200 μ L chloroform was added, the samples were vortexed and centrifuged as before. This step was repeated. Finally, the upper phase was transferred into a new tube and RNA was ethanol precipitated as described in 10.2.3.

10.2.5 Denaturing polyacrylamide gel electrophoresis (PAGE)

To follow up RNA integrity, oligonucleotides and tRNA were analyzed on an analytical denaturing PAGE. A 10% urea gel (40% gel concentrate, 50% gel diluent, 10% gel buffer concentrate) was used to analyze tRNA and a 15% urea gel (60% gel concentrate, 30% gel diluent and 10% gel buffer concentrate) was used for oligonucleotide analysis. After adding 25 μ L TEMED and 200 μ L ammonium peroxydisulfate, the gel was poured into a Biometra Eco-Maxi PAGE system and let it polymerize for 1 h. 100 ng of tRNA and oligonucleotides were diluted in 5 μ L and mixed with 5 μ L 2X denaturing loading buffer (10% 10X TBE, 90% formamide) and run for 3 h at 18 W. GelRed was used for staining and incubated for 15 minutes. 250 ng binary oligonucleotides were used in 5 μ L and 5 μ L of 2X denaturing loading buffer was added. Staining was performed using Toluidine blue by incubating the gel in a 0.03% aqueous solution for 1 h followed by destaining in desalted water overnight. GelRed stained gels were scanned on a Typhoon TRIO+ imager using $E_{Ex} = 532$ nm, $E_{Em} = 610$ nm. Destained Toluidine blue gels were scanned on a photo scanner (Epson Perfection V600). ImageJ was used to edit and merge images.

10.2.6 Preparative denaturing PAGE

In vitro transcribed tRNA was purified via denaturing PAGE. The gel was prepared as described above and run for 3 h at 18 W. Visualization of tRNA bands was performed using UV shadowing and bands were excised. Gel pieces (~1 cm²) were mashed with a scalpel and transferred into a 1.5 mL tube. 0.5 M NH₄OAc was added and RNA was eluted overnight by shaking at 750 rpm. To separate the solution from gel pieces, the mixture was transferred into Nanosep™ filtering columns (0.45 μ m) and centrifuged at 750 $\times g$ for 5 min. The flowthrough was collected and RNA was precipitated as described in 10.2.3.

10.2.7 Quantification of free chlorine in hypochlorous acid (HOCl)

Quantification of free chlorine in HOCl adhered to the ISO standard protocol Part 2 entitled “Colorimetric method using *N,N*-Diethyl-1,4-phenylenediamine (DPD), for routine control purposes” (ISO 7393-2:2017). DPD, initially colorless in its reduced state, turns pink upon oxidation. The pink-colored oxidation product facilitates quantification through UV absorbance measurement at 515 nm. Chlorine quantities were determined based on an external calibration utilizing potassium iodate (KIO₃) and potassium iodide (KI) spanning concentrations from 0.5 mg/L to 5.0 mg/L KIO₃. Calibration procedures involved the preparation of a standard solution (10 mL) comprising 10.06 μ g/mL KIO₃ and 1 mg/mL KI, subsequently utilized to prepare six calibration solutions containing 0, 0.6, 1, 2, 5, and 10 μ g/mL KIO₃ in 0.5 mL volumes. 10 μ L of 1 M sulfuric acid (H₂SO₄) was added to each calibration solution, followed by vortexing, spinning down, and incubation for precisely 1 min. Termination of the reaction was achieved by adding 10 μ L 1 M sodium hydroxide (NaOH) solution, vortexing, spinning the samples and finally adjusting the volume to 1 mL with ultrapure water. Subsequently, 50 μ L of a DPD buffer at pH 6.5 (46 g/L KH₂PO₄, 60.5 g/L Na₂HPO₄*12 H₂O, 0.8 g/L EDTA*2 H₂O) was

added to each calibration solution, followed by the addition of 50 μL of a freshly prepared DPD solution (1.1 g/L DPD, 0.2 g/L EDTA*2 H₂O, 3.6 mM H₂SO₄) before immediate absorbance measurement at 515 nm using a UV spectrophotometer in a 1.5 mL cuvette. For determination of free chlorine in HOCl, 1 mL of a 1/5000 dilution in ultrapure water was prepared, followed by the addition of the DPD buffer and DPD solution. The slope of the calibration curve was utilized for quantification purposes, with KIO₃ equivalents transformed into Cl₂ amounts according to 10.06 μg KIO₃ = 0.141 μmol Cl₂. Quantification of Cl₂ was conducted every two weeks.

10.2.8 Oxidation of ribonucleosides

Oxidation of nucleosides (adenosine, cytidine, guanosine, and uridine) was performed in 50 mM potassium phosphate buffer at pH 7.4. A 2X stock solution (200 μM nucleoside, 10 mM MgCl₂) was prepared and 60 μL was transferred into black 1.5 mL tubes. HOCl stock solutions (50 mM phosphate buffered pH 7.4) ranging from 0 to 1000 mM Cl₂ were prepared immediately before adding 60 μL to the buffered 2X nucleoside solution. Samples were vortexed, spun down, and precisely incubated for 10 min at 25°C in the darkness. DTT was added in a final concentration of 10 mM to terminate the reaction. Samples were stored at -20°C.

10.2.9 Oxidation of synthetic oligonucleotides and IVT-tRNA^{Asp}

Synthetic oligonucleotides and tRNA were processed using 25 ng/ μL RNA and Cl₂ concentrations up to 1.6 mM Cl₂ in 120 μL unless otherwise stated. RNA stock solutions including 50 ng/ μL RNA, 50 mM potassium phosphate buffer pH 7.4, and 10 mM MgCl₂ were prepared, 60 μL was transferred into black 1.5 mL tubes before adding 60 μL diluted phosphate buffered (50 mM, pH 7.4) HOCl solutions to final Cl₂ concentrations of 0 - 1.6 mM Cl₂. Samples were vortexed, spun down, and incubated for 10 min at 25°C in the dark before adding DTT (final concentration 10 mM). Aliquots for gel electrophoresis were taken before proceeding with RNA purification. 100 ng was used for GelRed stained gels, whereas 250 ng was used for Toluidine blue stained gels. Purification included ethanol precipitation, desalting using Zeba™ Spin Desalting columns, phenol/chloroform extraction (10.2.4), and final ethanol precipitation (10.2.3).

10.2.10 Kinetic UV analysis

UV kinetic analysis was performed using a Tecan Spark 10M spectrophotometer. 100 μM nucleoside solutions were analyzed under standard conditions (see 10.2.8) in a 96-well plate. The oxidation reaction was initiated by combining 60 μL of the buffered nucleoside mixture with 60 μL buffered chlorine solution followed by thorough mixing via pipetting. Kinetics were measured at 25°C for 10 minutes every 30 seconds. Upon completion of each experiment, full absorbance spectra were recorded from 200 to 400 nm with a wavelength step size of 2 nm. The provided absorbance spectra were adjusted by subtracting the corresponding values of HOCl-treated phosphate buffered

solution. Additionally, absorbance spectra of nucleoside standards (250 μM) were obtained in 50 mM phosphate buffer at pH 7.4.

10.2.11 Preparation of samples before LC-MS/MS analysis

Prior to subjecting RNA or oligoribonucleotides to LC-MS/MS analysis, samples underwent enzymatic digestion into nucleosides under following conditions: RNA was incubated for 2 h at 37°C in a solution containing 5 mM Tris*HCl pH 8 and 1 mM MgCl_2 using 0.6 U nuclease P1 from *P. citrinum*, 0.2 U snake venom phosphodiesterase from *C. adamanteus*, 0.2 U alkaline phosphatase from bovine intestinal mucosa, 10 U benzonase, 200 ng pentostatin and 500 ng tetrahydrouridine. For quantitative LC-MS/MS measurements, 37.5 pmol nucleoside, 25 ng binary oligoribonucleotide, and 50 ng of RNA or synthetic oligonucleotide were injected.

10.2.12 Neutral loss scan (NLS) of nucleosides

LC-MS/MS analysis of oxidized nucleosides was performed by conducting neutral loss scans. 37.5 pmol of each sample was injected and the MS was adjusted to detect mass transitions of the loss of 132 corresponding to the typical fragmentation pattern at the *N*-glycosidic bond. Signals in the range of m/z 229 to m/z 600 excluding proton adducts of the parent nucleosides for ^{12}C and ^{13}C isotopes were detected. Following precursor ions were excluded: $m/z = 244$ and 245 (minutes 4 to 5.5), $m/z = 245$ and 246 (minutes 5.5 to 7), $m/z = 284$ and 285 (minutes 14 to 17), $m/z = 268$ and 269 (minutes 23 to 25). The fragmentor voltage was set to 80 V, collision energy was set to 12 V and the cell accelerator voltage was set to 4 V. The crude reaction mixture was injected after diluting the samples in ultrapure water by 1/1000. HPLC and ion source settings were set as described in 10.2.15.

10.2.13 Synthesis of ARP-ribose control

100 pmol/ μL of the aldehyde-reactive probe (ARP) was mixed with 10 nmol/ μL ribose or the corresponding volume of ultrapure water in 20 mM HEPES pH 7.2, 2 mM EDTA and incubated for 2 h at 37°C in the dark. The reaction was terminated by diluting the mixture to a final concentration of 25 μM ARP. Subsequently, 20% denaturing PAGE was performed for 3 h at 20 W. An aliquot corresponding to 100 pmol ARP was loaded. Scans were performed on a Typhoon TRIO+ imager using $E_{\text{Ex}} = 488$ nm and $E_{\text{Em}} = 518$ nm.

10.2.14 LC-MS/MS analysis of ARP-ribose adduct

The MS2 scan of the ARP-ribose control was conducted to identify the precursor ion of the ARP-ribose adduct. 50 pmol ARP was injected. The following settings were used for HPLC using a Synergy Fusion RP column from Phenomenex (4 μm particle size, 80 Å pore

size, 2 mm inner diameter, 250 mm length): a flow rate was set at 0.35 mL/min at a column temperature of 35°C. Gradient elution was carried out over 30 min using mobile phases A (10 mM NH₄OAc pH 5.7, prepared with acetic acid) and B (pure acetonitrile). The gradient included the following steps: 0%-8% B (0-10 min), 8%-40% B (10-20 min), 40%-0% B (20-23 min) followed by a final step of 0% B (23-30 min). The DAD was set to detect wavelengths at 254 nm and 488 nm. After HPLC separation, samples were transferred to the triple quadrupole mass spectrometer, equipped with an electrospray ion source (Agilent Jet Stream). The ion source operated at a gas temperature of 300°C, gas flow of 7 L/min, nebulizer pressure of 60 psi, sheath gas temperature of 400°C, sheath gas flow of 12 L/min, and a capillary voltage of 3000 V. The positive ion mode was applied for measurements using the Agilent MassHunter software. The mass spectrometer was run at a fragmentor voltage of 80 V to avoid source fragmentation, a cell accelerator voltage of 5 V, a scan time of 500 ms, and detecting mass signals between m/z 100 and 1000.

In a next step, a product ion scan was performed to analyze fragmentation patterns of the ARP-ribose adduct and the ARP-MQ control. 50 pmol was injected and HPLC and ion source settings were applied as used in the MS₂ scan. The MS was run in the product ion scan mode with the following settings: fragmentor voltage of 80 V, collision energy of 20 V, and cell accelerator voltage of 5 V. Precursor ions were set to $m/z = 824$ for the ARP-ribose adduct and $m/z = 677$ corresponding to the ARP-MQ control.

Finally, the gradient described in 10.2.15 was applied and retention times for the ARP-ribose adduct and the ARP-MQ control were identified by performing an MRM scan. 25 pmol was injected and mass transitions of m/z 824 → 692 and m/z 692 → 612 were detected. The ion source and MS were run as described in the MS₂ scan.

10.2.15 Quantitative LC-MS/MS analysis

Digested samples were analyzed using an Agilent 1260 Infinity (II) LC system coupled with a diode array detector (DAD) and a Triple Quadrupole mass spectrometer (Agilent 6470). Following settings were used for HPLC using a Synergy Fusion RP column from Phenomenex (4 μm particle size, 80 Å pore size, 2 mm inner diameter, 250 mm length): a flow rate was set at 0.35 mL/min at a column temperature of 35°C. Gradient elution was carried out over 54 min using mobile phases A (10 mM NH₄OAc pH 5.8, prepared with acetic acid) and B (pure acetonitrile). Following steps were set during the gradient: 0% B (0-10 min), 0%-10% B (10-30 min), 10%-40% B (30-40 min), 40%-0% B (40-43 min) followed by a final step of 0% B (43-54 min). Separation of nucleosides was monitored photometrically at 254 nm and 488 nm for ARP-labeling experiments before being transferred to the triple quadrupole mass spectrometer, equipped with an electrospray ion source (Agilent Jet Stream). The ion source operated at a gas temperature of 300°C, gas flow of 7 L/min, nebulizer pressure of 60 psi, sheath gas temperature of 400°C, sheath gas flow of 12 L/min, and a capillary voltage of 3000 V. The positive ion mode was applied for measurements using the Agilent MassHunter software and detection was performed employing the dynamic multiple reaction monitoring (dMRM) mode with following parameters (Table 6):

Table 6. LC-MS/MS parameters for modified nucleosides measured in dMRM mode.

Compound	Precursor ion [m/z]	Product ion [m/z]	Fragmentor voltage	Collision energy	Cell accelerator voltage	Retention time	Δ Retention time
ho ⁵ C	260	128	80 V	9 V	4 V	4.4 min	4 min
ho ⁵ U	261	129	80 V	9 V	4 V	5.2 min	4 min
Cl ⁵ C	278	146	75 V	13 V	4 V	15.5 min	4 min
Cl ⁵ U	279	147	75 V	13 V	4 V	17.2 min	4 min
oxo ⁸ A	284	152	90 V	21 V	4 V	24.4 min	4 min
oxo ⁸ G	300	168	100 V	13 V	4 V	18.0 min	4 min
Cl ⁸ A	302	170	95 V	17 V	4 V	33.3 min	4 min
Cl ⁸ G	318	186	85 V	17 V	4 V	27.0 min	4 min
ARP only	692	612	80 V	20 V	4 V	23.9 min	4 min
ARP+Rib	824	692	80 V	20 V	4 V	24.5 min	4 min

Data analysis was performed by peak integration using the Agilent MassHunter Qualitative Analysis Software (Version 10.0). The area under the curve was used to determine absolute amounts according to the calculated slope of the corresponding calibration curve. Main nucleosides were monitored and quantified via UV detection at 254 nm and modified nucleosides were detected mass spectrometrically.

10.2.16 LC-MS/MS analysis of alternative guanosine oxidation products

Alternative guanosine products were measured via LC-MS/MS as described in 10.2.15. Measurements were performed in an MRM mode according to the following mass transitions of the ¹²C, ¹³C, and ¹⁵N isotopes listed in Table 7.

Table 7. Mass transitions of ¹²C, ¹³C, and ¹⁵N isotopes for alternative guanosine oxidation products.

Nucleo- side	¹² C		¹³ C		¹⁵ N		Frag- mentor voltage	Collision energy	Cell accelerat or voltage
	Precursor ion [m/z]	Product ion [m/z]	Precursor ion [m/z]	Product ion [m/z]	Precursor ion [m/z]	Product ion [m/z]			
r2lh	318	186	328	191	323	191	75 V	13 V	4 V
rDiz	244	112	252	115	249	117	90 V	21 V	4 V
rGh	290	158	299	162	295	163	80 V	9 V	4 V
rlz	245	113	253	116	249	117	75 V	13 V	4 V
rSp	316	184	326	189	321	189	95 V	17 V	4 V
rZ	263	131	271	134	267	135	100 V	13 V	4 V

10.2.17 ARP-labeling

Abasic site labeling was achieved employing an aldehyde-reactive probe (ARP) reagent: Alexa Fluor™ 488 hydroxylamine known for its specific reaction with the open-ring aldehyde form of the ribose moiety at abasic sites. The reaction mixture, comprising 20 mM HEPES at pH 7.2, 2 mM EDTA, 800 ng of oxidized RNA, 100 μM ARP reagent was incubated for 2 h at 37°C in darkness. Following incubation, the reaction was terminated by the addition of 40 μL ultrapure water. Labeled oligonucleotides were isolated from excess ARP reagent using the Oligo Clean & Concentrator kit. Absorbance spectra were

recorded over a range of 220 nm to 850 nm using a Nanodrop™ One device. Analysis of labeling reactions was conducted through both analytical 15% denaturing PAGE and LC-MS in dynamic MRM mode as described in 10.2.15. Scans were performed using a Typhoon TRIO+ imager with specific settings for GelRed (E_{Ex} = 532 nm, E_{Em} = 610 nm) and AlexaFluor™ 488 (E_{Ex} = 488 nm, E_{Em} = 526 nm). ImageJ was used to edit and merge images.

10.2.18 ^{32}P -labeling of RNA

Synthetic oligonucleotides were labeled with ^{32}P using T4 Polynucleotide Kinase (PNK) 10 U/ μL following manufacturer's protocol. In summary, the reaction was conducted in a total volume of 100 μL comprising 1X commercial PNK buffer with final concentrations of 2.5 μM oligonucleotide, 2.5 μM cold ATP, 1 μM ^{32}P -labeled ATP and 0.5 U/ μL PNK. The reaction was incubated for 30 minutes at 37°C. To isolate ^{32}P -labeled oligonucleotide from excess ATP, 15% denaturing PAGE was performed and radiolabeled bands were excised after visualizing using a storage phosphor screen. Following exposition, the phosphor screen was scanned on a Typhoon TRIO+ imager using the phosphor mode at normal sensitivity using the emission filter with a 390 bandpass and an excitation wavelength E_{Ex} = 532 nm.

10.2.19 Next-generation sequencing on an Illumina NextSeq 2000

Experiments on oxidized IVT-tRNA^{Asp} were performed by myself during several stays in Nancy. ██████████ ██████████ performed experiments on synthetic oligonucleotides containing either a guanosine, oxo⁸G or an AP-site at position 16. ██████████ performed bioinformatic data analysis and detailed scripts can be requested from him. Mapping methods are based on the AlkAniline-Sequencing (AAS) protocol.¹²⁰

a. Chemical treatment:

50 – 200 ng of RNA was subjected to alkaline or Mg^{2+} treatment. Alkaline treatment was performed in a 50 mM bicarbonate buffer at pH 9.2 for 5 minutes at 96°C. Mg^{2+} treatment was conducted in 2 mM MgCl_2 in 100 mM Tris*HCl buffer pH 8.0 for 3 minutes at 96°C. Both reactions were terminated by ethanol precipitation and subsequently frozen in liquid nitrogen. Following centrifugation (7.2.3) and a washing step, the pellet was dissolved in ultrapure water. The alkaline- or Mg^{2+} -fragmented RNA was subjected to dephosphorylation for 1h at 37°C by adding 5 U antarctic phosphatase and 10X reaction buffer. After terminating the reaction, RNA fragments were extracted by phenol/chloroform extraction as described in 10.2.4 and ethanol precipitated (10.2.3) without dissolving the RNA pellet. Instead, the pellet was dissolved in 1 M aniline pH 4.5 and incubated at 60°C for 15 minutes in the dark. The reaction was terminated by adding ethanol and subsequent precipitation (10.2.3).

b. Library preparation

The NEBNext™ Small RNA Library Prep Set for Illumina was used for library preparation of RNA samples according to the manufacturer's protocol. Final library qualities were analyzed on a Bioanalyzer 2100 using a high-sensitivity DNA chip and quantification was performed on a Qubit™ 3.0 fluorometer following manufacturer's instructions.

c. Illumina sequencing

Libraries were multiplexed and loaded on a flow cell at a final concentration between 650 and 750 pM. Sequencing was performed on an Illumina NextSeq 2000 platform conducting 50 bp single-read sequencing.

d. Data analysis

Trimmomatic V0.39 was used for trimming raw sequencing reads and bowtie2 V2.4.2¹⁵⁷ was used to align resulting reads to the corresponding RNA reference sequence (synthetic oligonucleotides and *H. sapiens* tRNA^{Asp}) in end-to-end mode while excluding multiple mapped reads. A custom awk script was used to count 5'-reads' extremities. Normalized G Counts (NormGcount) were calculated as the number of reads starting at a position X divided by the local background, which was defined as the median of signals for all non-G residues in an 11-nucleotide window relative to the position X ($X \pm 5$ nucleotides). The threshold was evaluated according to a limit of quantification for a signal-to-noise ratio >10. It was set to 10 times the median of NormGcount. Signals were considered if the coverage was higher >1000 if the signal surpassed the threshold and if the random error of the NormGcount was <10%.

Reverse transcription (RT) signatures were calculated using full-length reads bypassing the modified site. Mpileup utility of samtools was used to treat aligned reads and to calculate deletion and mismatch proportions at the corresponding modified site. Mismatch rates were defined as the proportion of "apparent" mutations relative to the correctly called residue.

10.2.20 Synthesis of an AP-site containing oligonucleotide

██████████ from the group of ██████████, Innsbruck performed the synthesis based on the procedure described by Küpfer *et al.* 2007.¹⁴³

10.2.21 Use of artificial intelligence

Artificial intelligence was used to improve English language, grammar and style, for translation purposes and rephrasing text sections using the following tools:

OpenAI. (2024). ChatGPT (GPT-4) [Large language model]. Retrieved from 21.06.2024.

DeepL GmbH. (2024). DeepL Translator. Retrieved from <https://www.deepl.com/translator>

DeepL GmbH. (2024). DeepL Write. Retrieved from <https://www.deepl.com/write>

10.2.22 Images and Figures

Images and Figures were created and edited with BioRender.com, Adobe Illustrator 2024 V5, ImageJ V5 (Version 1.52q) and IrfanView.

11 APPENDIX

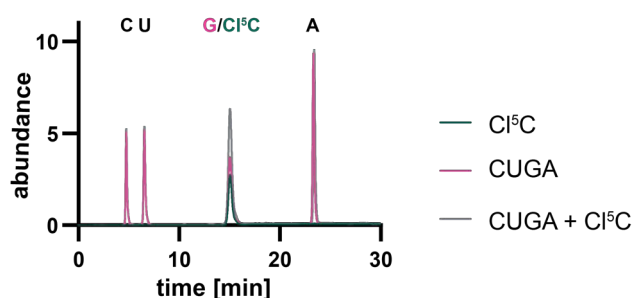


Figure S1. UV traces of main nucleosides cytidine, uridine, guanosine, and adenosine superimposed with Cl⁵C.

Guanosine and Cl⁵C were coeluting at 14 minutes. 50 pmol of each nucleoside wd for each sample: Cl⁵C only (dark green), main nucleosides only (pink), main nucleosides additionally including Cl⁵C (gray).

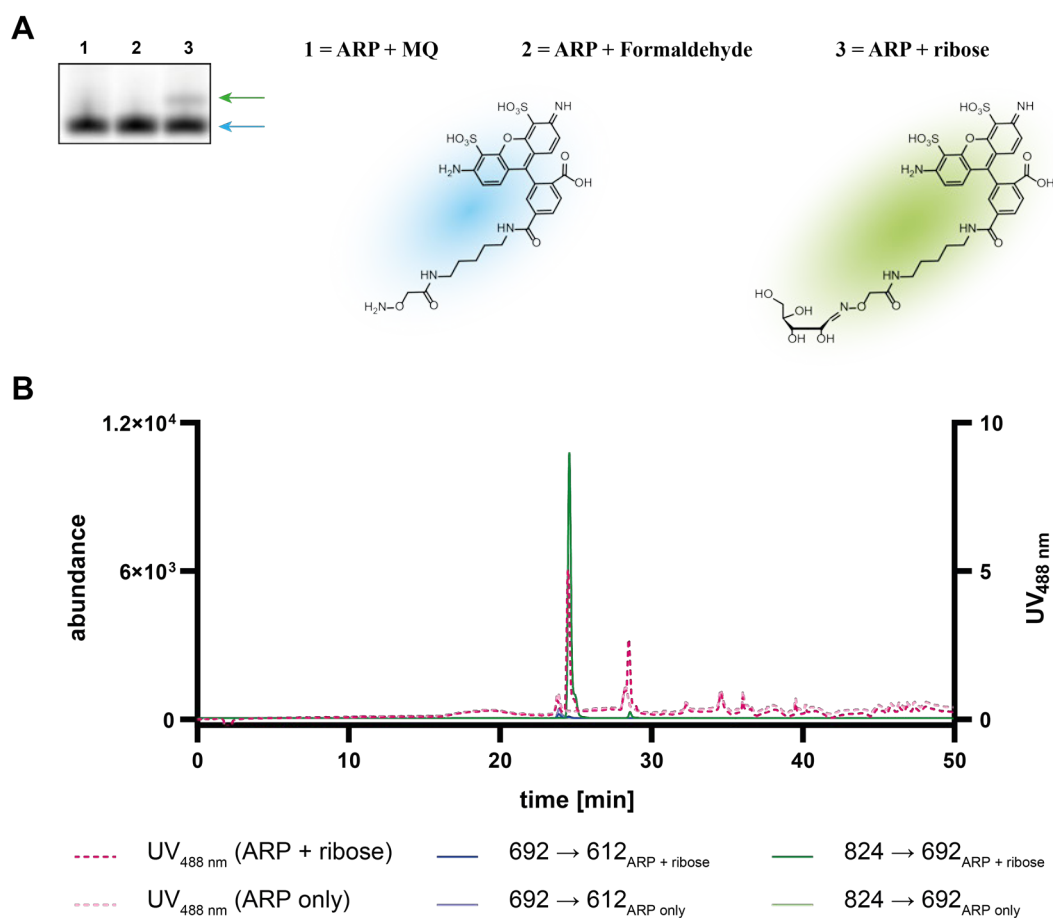


Figure S2. Investigation of the LC-MS/MS method to detect the ARP-labeled ribose adduct.

A 20%-denaturing PAGE gel after 3 h at 20 W. Lane 1: ARP + water, lane 2: ARP + formaldehyde, lane 3: ARP + ribose. Samples 1 and 2 are negative controls and do not react with the ARP reagent. The product is shown in blue. The covalently linked adduct of the ARP reagent and a ribose molecule is depicted in green and corresponds to the higher migrating

band indicated with a green arrow. Imaging was performed by applying Alexa Fluor™ 488 settings on a Typhoon TRIO+ imager. 100 pmol of each sample was loaded. **B** Merged chromatograms of the ARP only and the ARP + ribose controls of the LC-MS/MS measurement using an MRM mode. 25 pmol was injected. Created with BioRender.com (2024).

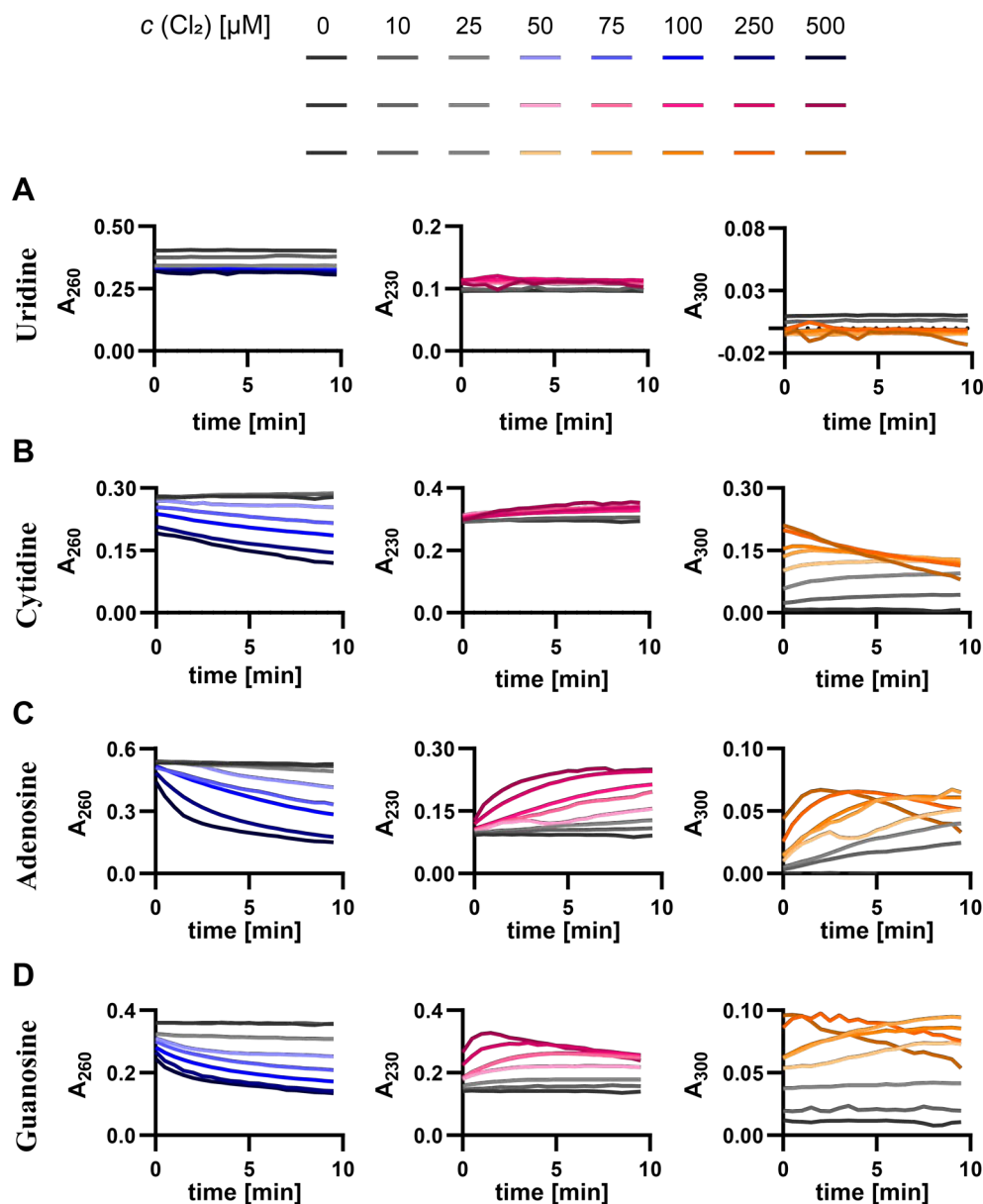


Figure S3. Kinetic UV chromatograms of nucleoside oxidation reactions.

100 μM nucleosides were oxidized with HOCl within a range of 0 to 500 μM Cl₂ in potassium phosphate buffer (50 mM, pH 5.8) at 25°C for 10 minutes in a 96-well plate. Absorbances were recorded every 40 seconds during the complete incubation period at 260 nm (blue), 230 nm (magenta) and 300 nm (orange) using a Tecan™ reader. Chromatograms were corrected by subtracting the corresponding HOCl-treated phosphate buffer solution. **A** UV analysis of uridine revealed no significant changes in absorbances over time at the measured wavelengths. **B** Cytidine exhibited hypochromic changes at 260 nm with increasing oxidant concentrations whereas absorbances increased at 230 and 300 nm followed by declining absorbances at 300 nm for highest Cl₂ concentrations. **C** Adenosine demonstrated similar results to cytidine albeit more intensely showing hypochromic changes at 260 nm and hyperchromic absorbances at 230 nm. Absorbances at 300 nm increased constantly within 10 minutes for concentrations up to 100 μM Cl₂ and decreased thereafter for higher Cl₂ concentrations. **D** Guanosine was the most affected showing changes in UV absorbances even at the lowest applied Cl₂

concentration of 10 μM . Recorded absorbances at 230 nm behaved similarly to those at 300 nm increasing constantly for Cl_2 concentrations up to 100 μM and decreasing thereafter for 250 μM and 500 μM applied Cl_2 .

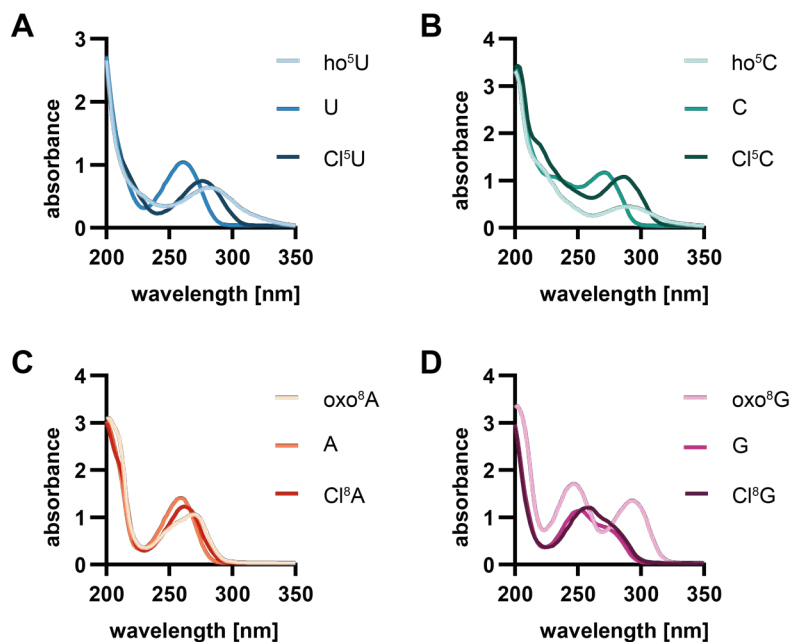


Figure S4. Spectra of nucleoside reference substances.

Pyrimidines, purines, and their corresponding oxidation products were analyzed via UV spectroscopy. 1 mM solutions were recorded in a range between 200 to 350 nm. **A** Shown are spectra of uridine (U), 5-hydroxyuridine (ho⁵U) and 5-chlorouridine (Cl⁵U). **B** Shown are spectra of cytidine (C), 5-hydroxycytidine (ho⁵C), and 5-chlorocytidine (Cl⁵C). **C** Shown are spectra of adenosine (A), 8-oxoadenosine (oxo⁸A) and 8-chloroadenosine (Cl⁸A). **D** Shown are spectra of guanosine (G), 8-oxoguanosine (oxo⁸G) and 8-chloroguanosine (Cl⁸G).

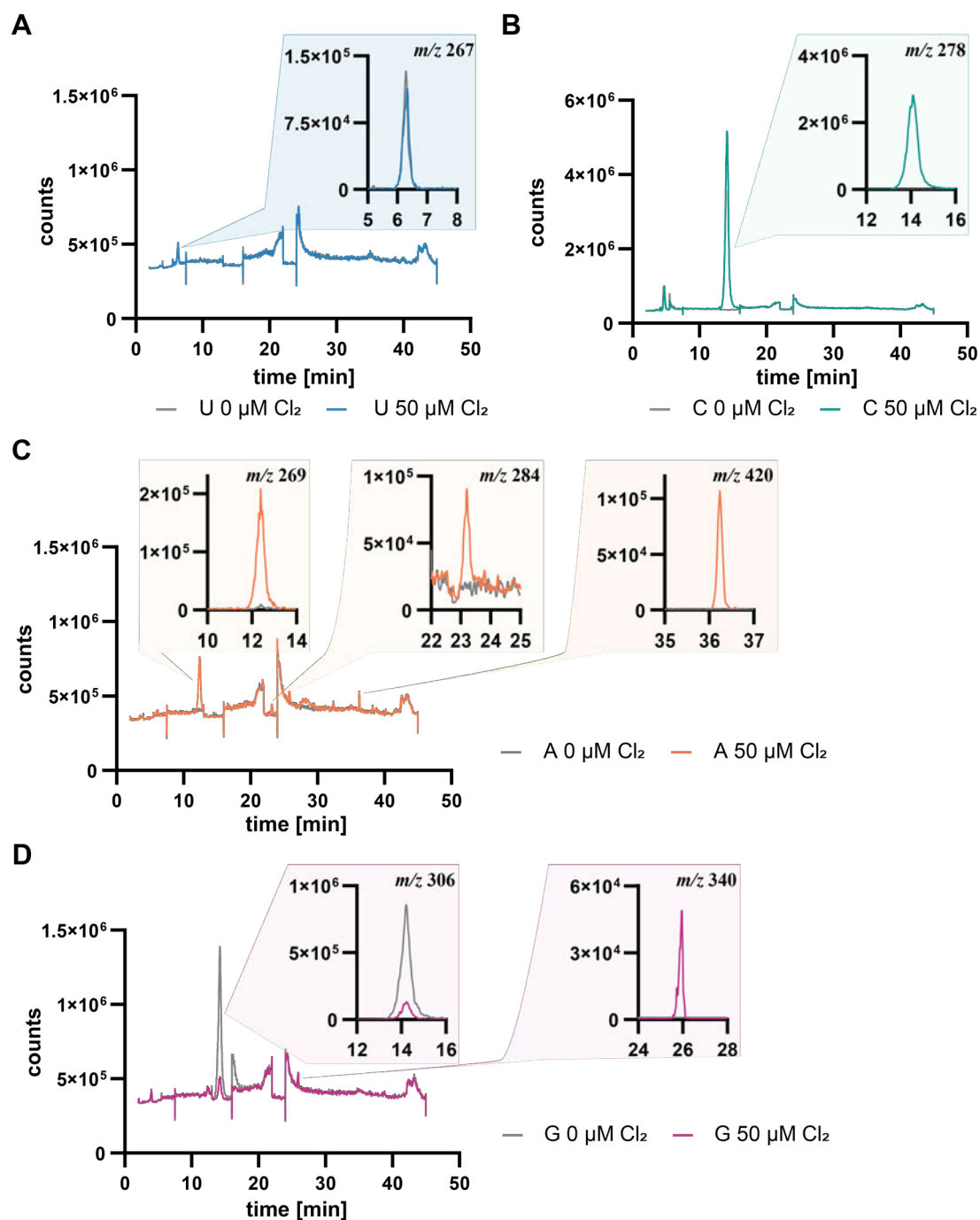


Figure S5. Total ion chromatograms of oxidized nucleosides quenched with DTT.

100 μM nucleoside solution was oxidized with 100 $\mu\text{M Cl}_2$ for 10 min and quenched with DTT. 37.5 pmol was injected for untreated controls (shown in gray) and for oxidized uridine (**A**, blue), cytidine (**B**, green), adenosine (**C**, orange) and guanosine (**D**, pink). Shown are total ion chromatograms of neutral loss scans detecting mass transitions losing m/z 132 corresponding to the ribose moiety. Absolute counts are indicated on the y-axis in correlation to the retention time [min]. As observed in UV analysis, reactivity differs within parent nucleosides. **A** Uridine did not significantly change upon oxidation (blue), whereas cytidine (**B**, green) oxidation resulted in one major signal at 14.1 min with m/z 278 corresponding to Cl^5C confirmed by comparison with an external standard. **C** Comparing untreated (gray) and oxidized adenosine (orange) revealed signals at 12.1 min with m/z 269 identified as inosine, oxo⁸A eluting at 23.12 min (m/z 284), Cl^8A eluting at 32.6 min (m/z 302) and two signals with $m/z > 400$: at 25.8 min (m/z 425) and at 36.2 min (m/z 420). **D** Changes upon oxidation on guanosine were majorly visible due to the loss of the parent nucleoside at 14.0 min detected as $[\text{G} + \text{Na}^+]$ with m/z 306.

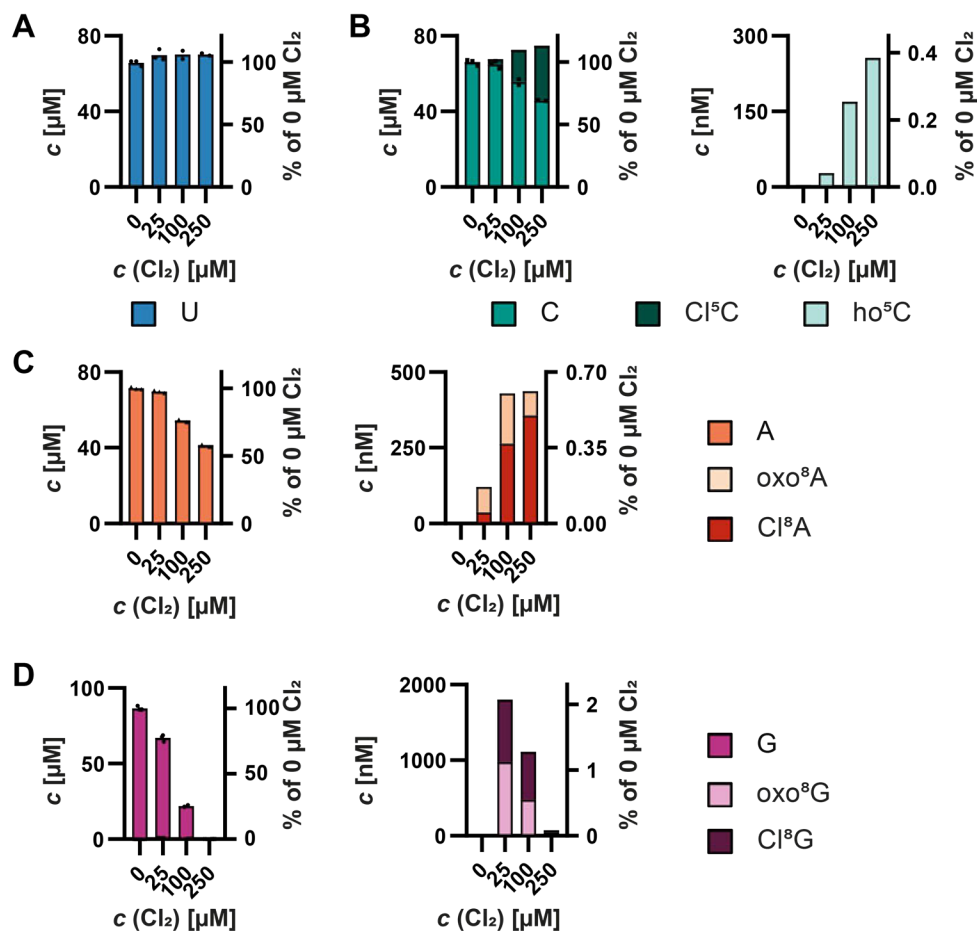


Figure S6. LC-MS/MS quantification of oxidized nucleoside monophosphates (NMPs) analyzed after digestion to nucleoside level.

Oxidation reactions were performed according to defined standard conditions and in an identical manner as for nucleosides. NMPs were digested down to nucleosides and 10 pmol were analyzed via LC-MS using external calibrations. Absolute quantities presented for **A: UMP** **B: CMP** **C: AMP** **D: GMP**. Shown are the mean values of $n = 2$.

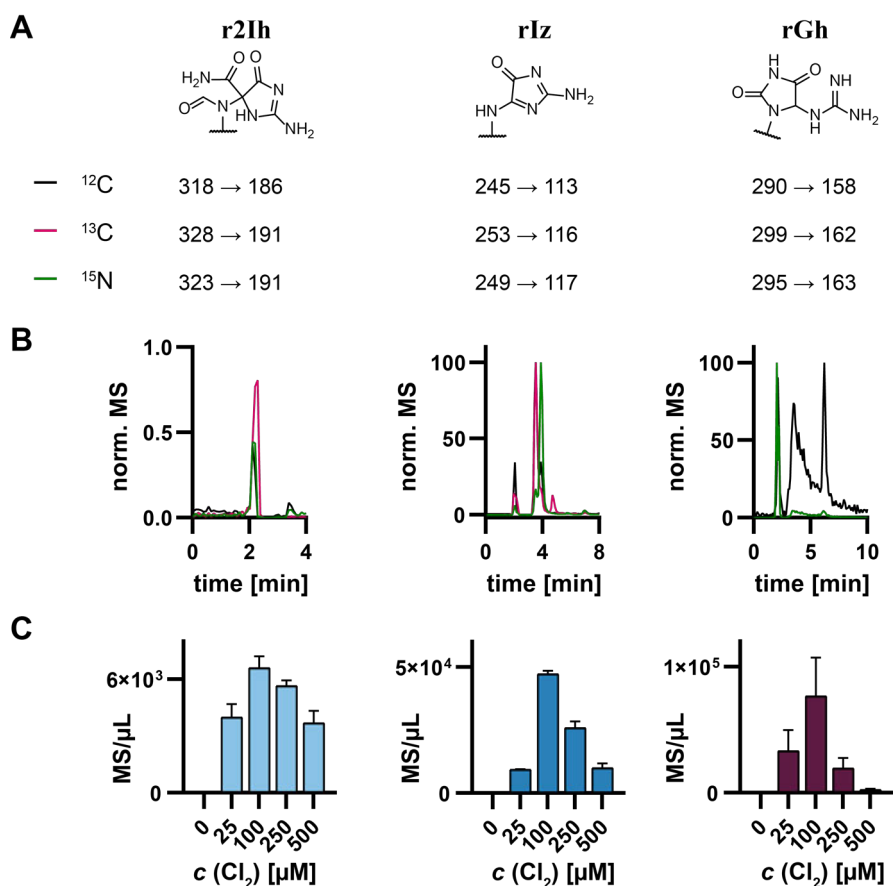


Figure S7. Identification of r2lh, rlz and rGh utilizing isotope-labeled guanosine.

A Mass transitions of 5-carboxamido-5-formamido-2-iminohydantoin (r2lh), imidazolone (rlz) and guanidinohydantoin (rGh) for ^{12}C -, ^{13}C -, and ^{15}N -isotopes. **B** Conversely, the chromatogram of rlz exhibited not only a single signal at 2.1 min, but also included the native ^{13}C isotope signal of rDiz at 3.8 minutes. Mass transitions of r2lh mirrored those of Cl⁶G explaining the low relative signals. Only the signal at 2.2 minutes was consistent across all isotopes and pinpointed the signal to r2lh. MS signals for rGh from the ^{12}C isotope exhibited considerable noise throughout the gradient as did the ^{13}C signal, with two signals appearing during the first 5 minutes at 2.2 min and 4.8 min. Yet only the signal at 2.2 minutes aligned for all isotopes. Furthermore, a closer examination of this signal revealed two closely spaced peaks, consistent with findings in other studies attributed to its isomer iminoallantoin (displayed in Figure 20) differing slightly in their chromatographic behavior.¹⁵⁸ **C** Presentation of the results obtained from oxidized ^{12}C -guanosine across a range of 0 μM to 500 μM Cl₂ displayed as MS signals normalized to the initial reaction volume.

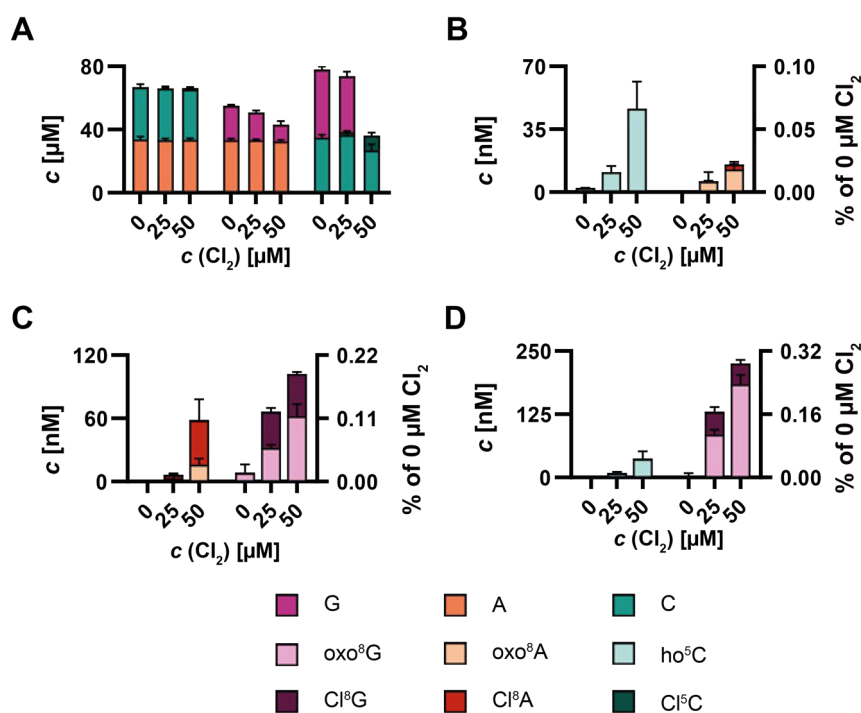


Figure S8. Absolute quantities of AC, AG, and CG binary oligonucleotides analyzed via LC-MS/MS.

A Abundance of main nucleosides and Cl^5C (dark green) in picomole per μL of oxidized binary oligonucleotides. Adenosine (orange) was unchanged in both binary combinations (AC and AG), whereas guanosine (pink) was consumed in the AG and CG combination. Cytidine (green) was mostly unchanged in the AC combination and slightly reduced at $50 \mu\text{M}$ Cl_2 in the CG combination. Cl^5C was the only oxidation product detected in micromolar quantities (AC: $0.81 \mu\text{M}$ and CG: $18.8 \mu\text{M}$). **B**, **C**, and **D** show quantities of oxidation products in nanomolar concentrations for the AC combination (**B**), the AG combination (**C**) and the CG combination (**D**). Shown are mean values ($n = 3$) \pm SD.

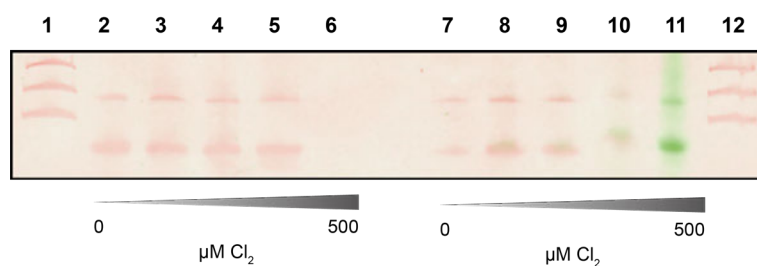


Figure S9. Merged image of ³²P-labeled 38mer upon oxidation and ARP labeling.

Lane 1 and 12 include ladders with 200, 100, and 50 base pairs. Lanes 2 to 6 are loaded with 100 ng samples after oxidation with 0, 10, 50, 100 and $500 \mu\text{M}$ Cl_2 . Lanes 7 to 12 include samples of the same oxidation experiment after ARP labeling. The image shown is an overlay of a GelRed scan (red) and a fluorescent scan (green).

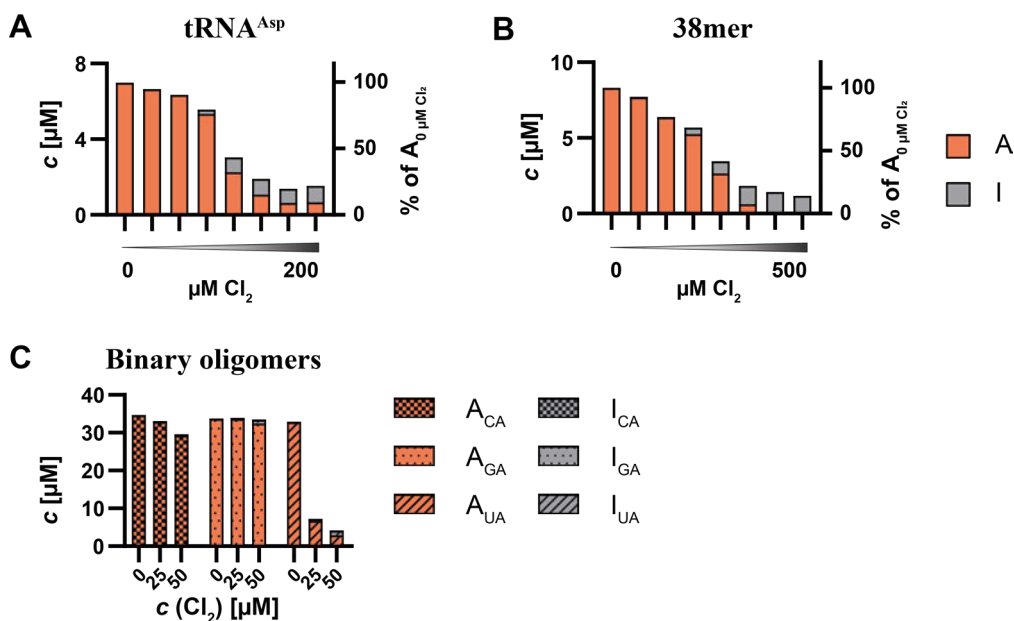


Figure S10. Inosine abundances obtained from data generated by a neutral loss scan.

500 ng was injected and a neutral loss scan (NLS) was performed as described in the method section. Inosine quantities were calculated based on extracted ion chromatograms and external calibration curves. As NLS data is not supposed to be used for quantification purposes, shown quantities only serve as estimations. Exact abundances have to be determined by conducting a dMRM scan. Quantities of A and I are indicated as micromolar concentrations on the left y-axis and as relative proportions related to A present in 0 $\mu\text{M Cl}_2$ treated control. **A** IVT-tRNA^{Asp} oxidized in a range from 0 to 200 $\mu\text{M Cl}_2$ (0, 10, 25, 50, 75, 100, 150, 200 μM). Inosine was detected in micromolar quantities at 50 $\mu\text{M Cl}_2$ treatment and increased constantly until reaching 15% adenosine present in the 0 $\mu\text{M Cl}_2$ treated sample. **B** Absolute quantities of A and I of a synthetic oligonucleotide (38mer) oxidized at 0, 10, 25, 50, 75, 100, 250 and 500 $\mu\text{M Cl}_2$. **C** Absolute quantities for A and I in oxidized binary oligonucleotides composed of C and A (grid pattern), G and A (dotted pattern) and U and A (lined pattern).

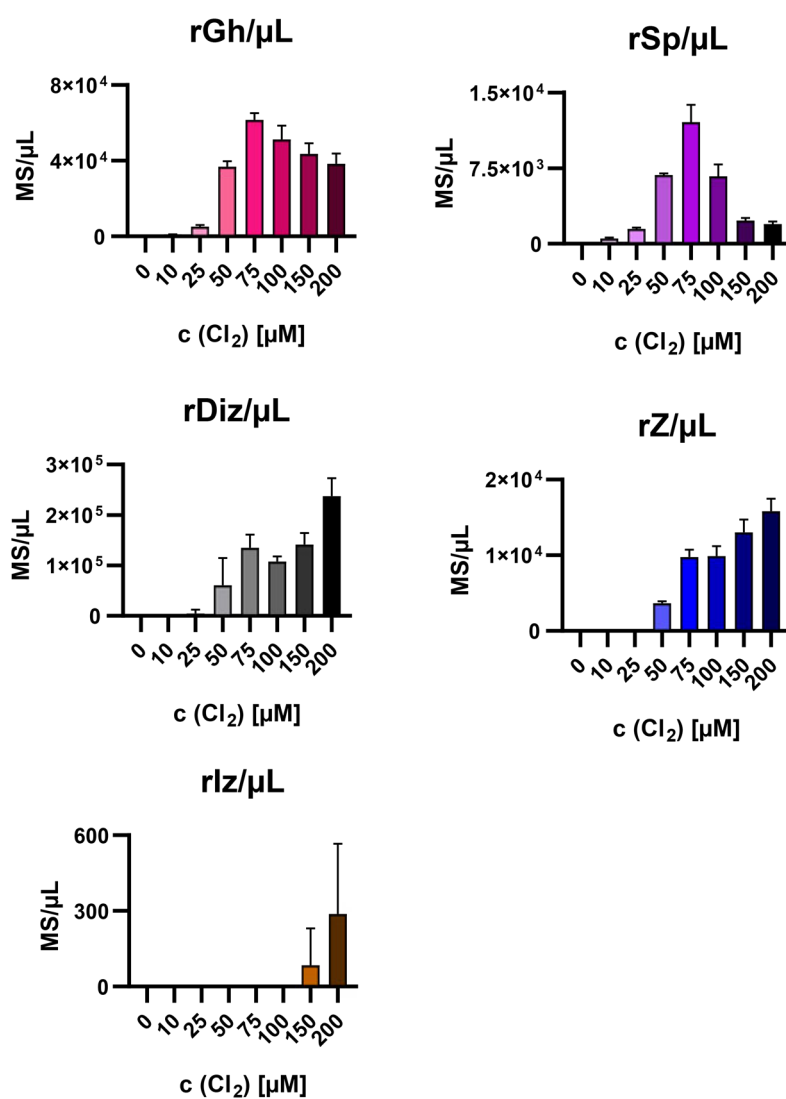


Figure S11. Relative LC-MS/MS quantification of alternative guanosine oxidation products of oxidized IVT-tRNA^{Asp}.

Data shown corresponds to the abundances shown in Figure 26C. MS signals are normalized to the initial reaction volume. The experiment covered a range of 0 μM to 200 μM Cl_2 (dark gray). Shown are mean values ($n = 3$) \pm SD.

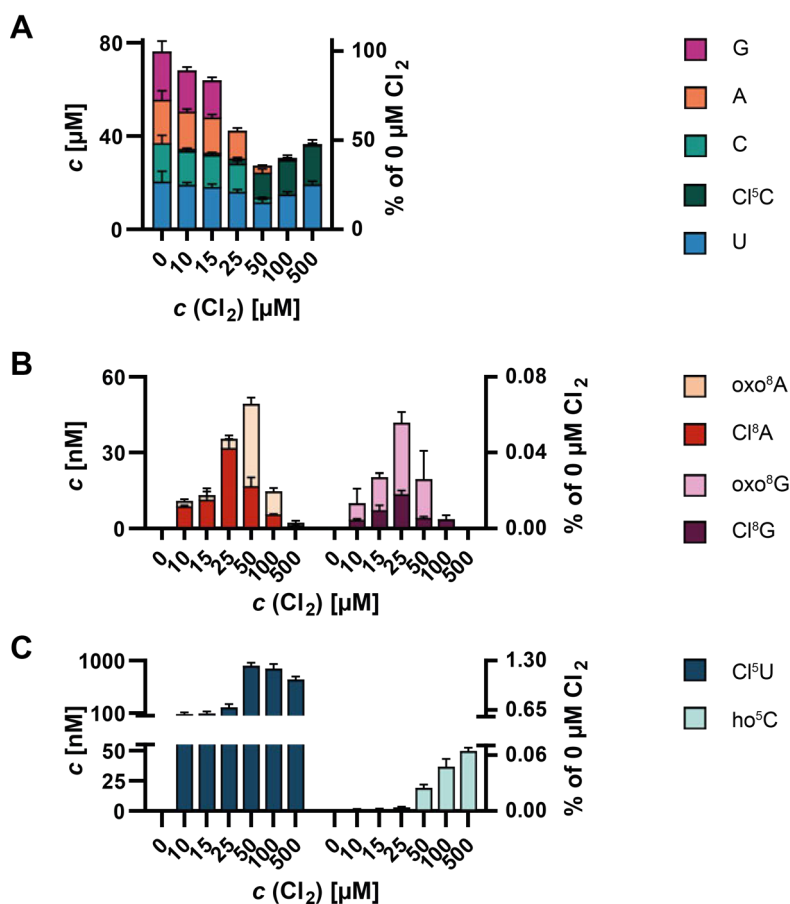
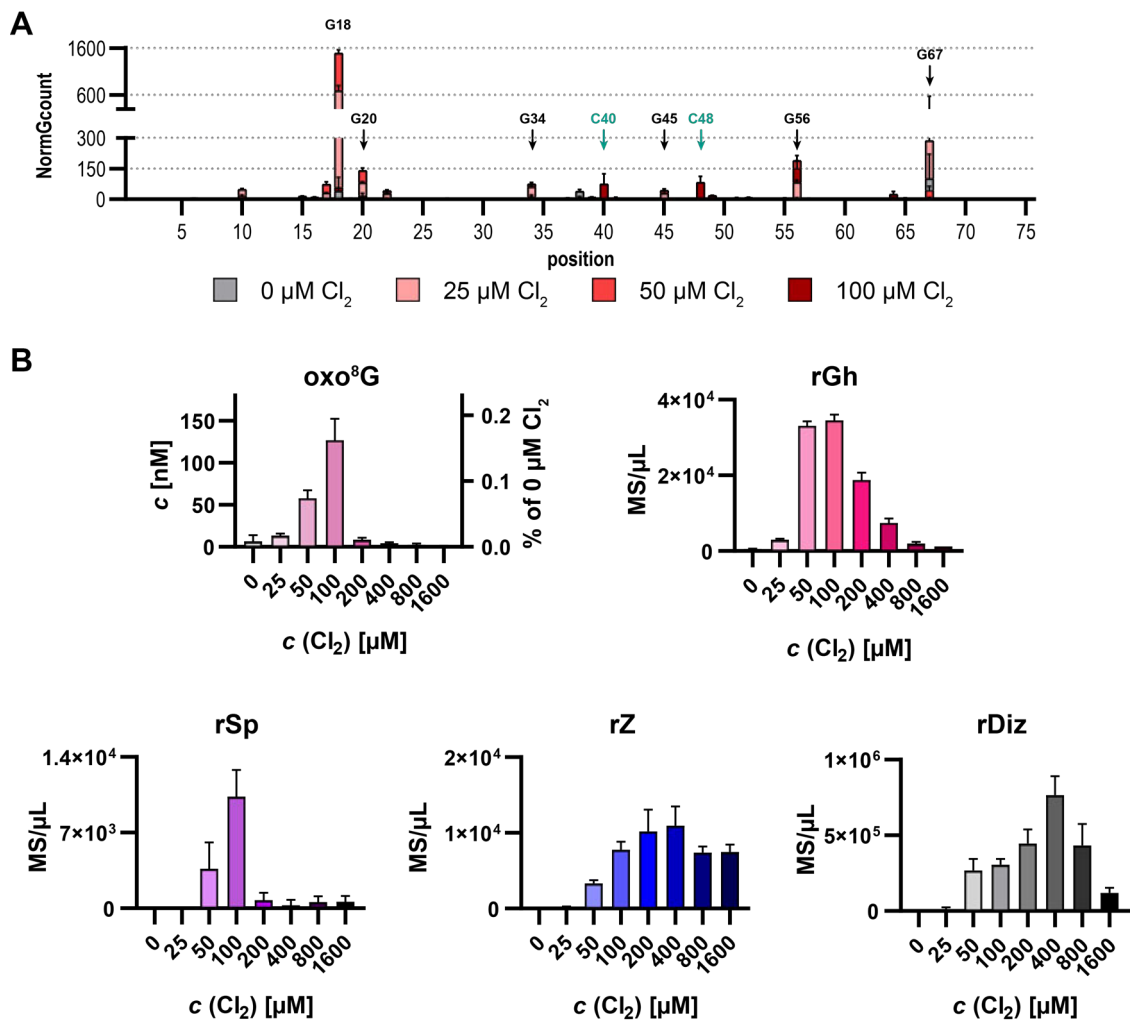


Figure S12. Absolute quantities of total RNA extracted from *S. c.* analyzed via LC-MS/MS.

A Absolute quantities of nucleosides are depicted in micromolar concentration as initially present in oxidation reactions correlated to increasing oxidant concentrations. The right y-axis indicates relative quantities related to total nucleosides present in 0 μM Cl_2 control. **B** Displayed are purine oxidation products and **C** pyrimidine oxidation products in nanomolar concentrations. 50 ng sample was injected following enzymatic digestion down to nucleosides. Absolute quantification utilized calibration curves of external standards. Mean values ($n = 3$) \pm SD are indicated.



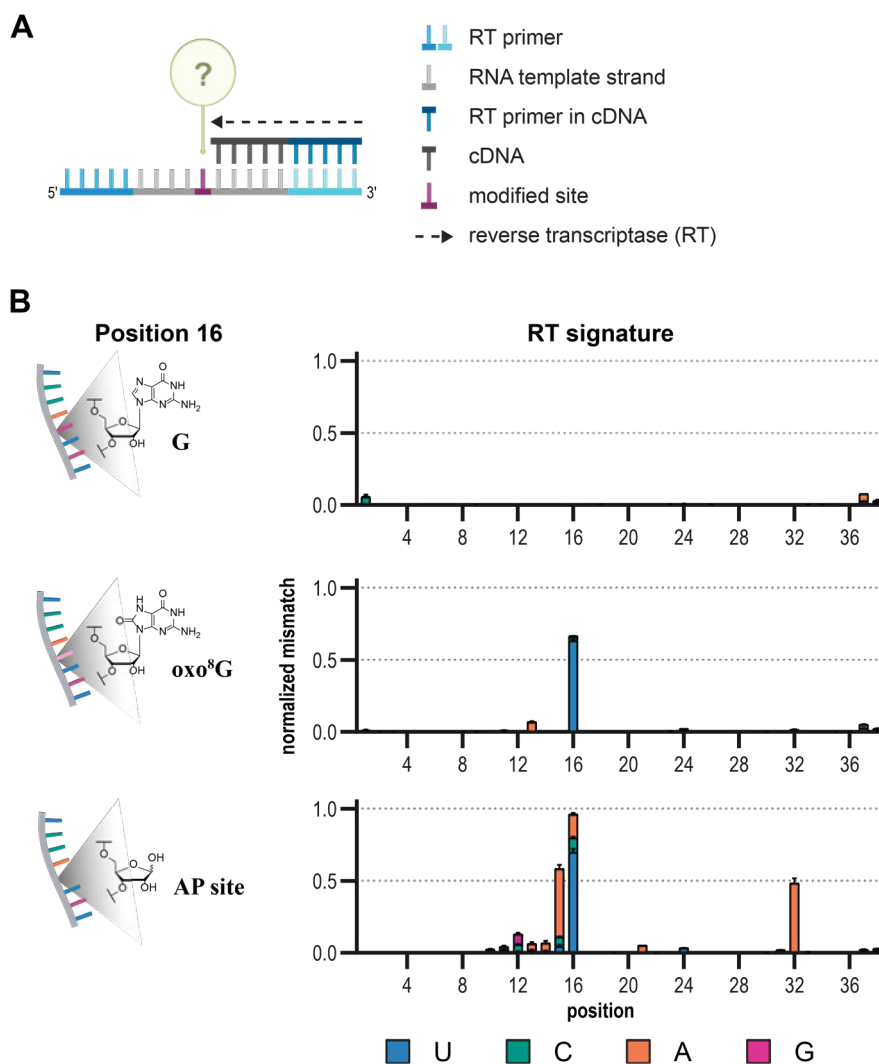


Figure S14. Reverse transcription (RT) signatures shown for the synthetic oligonucleotides containing either G (top), oxo⁸G (middle) or an AP site (bottom) at position 16.

A Illustration of the oligonucleotide constructs after library preparation during RT. The question green mark indicates position 16 in the resulting cDNA (dark gray), which shows a modification-specific RT signature. **B** Comparison of RT signatures for the G- (top), oxo⁸G- (middle) and AP- modified (bottom) oligonucleotides at position 16. Shown are mean values ($n = 3$) \pm SD of normalized mismatches. Created with BioRender.com (2024).

12 REFERENCES

1. Crick, F. Central dogma of molecular biology. *Nature* **227**, 561–563; 10.1038/227561a0 (1970).
2. CRICK, F. H. On protein synthesis. *Symposia of the Society for Experimental Biology* **12**, 138–163 (1958).
3. CRICK, F. H. On the genetic code. *Science (New York, N.Y.)* **139**, 461–464; 10.1126/science.139.3554.461 (1963).
4. McCown, P. J. *et al.* Naturally occurring modified ribonucleosides. *Wiley interdisciplinary reviews. RNA* **11**, e1595; 10.1002/wrna.1595 (2020).
5. WATSON, J. D. & CRICK, F. H. Molecular structure of nucleic acids; a structure for deoxyribose nucleic acid. *Nature* **171**, 737–738; 10.1038/171737a0 (1953).
6. Clancy, S. Chemical structure of RNA. Available at <https://www.nature.com/scitable/topicpage/chemical-structure-of-rna-348/> (2008).
7. Zhou, H. *et al.* Characterizing Watson-Crick versus Hoogsteen Base Pairing in a DNA-Protein Complex Using Nuclear Magnetic Resonance and Site-Specifically ¹³C- and ¹⁵N-Labeled DNA. *Biochemistry* **58**, 1963–1974; 10.1021/acs.biochem.9b00027 (2019).
8. Halder, S. & Bhattacharyya, D. RNA structure and dynamics: a base pairing perspective. *Progress in biophysics and molecular biology* **113**, 264–283; 10.1016/j.pbiomolbio.2013.07.003 (2013).
9. Grosjean, H. & Westhof, E. An integrated, structure- and energy-based view of the genetic code. *Nucl Acids Res* **44**, 8020–8040; 10.1093/nar/gkw608 (2016).
10. Dörner, K., Ruggeri, C., Zemp, I. & Kutay, U. Ribosome biogenesis factors—from names to functions. *The EMBO journal* **42**, e112699; 10.15252/embj.2022112699 (2023).
11. Schimmel, P. The emerging complexity of the tRNA world: mammalian tRNAs beyond protein synthesis. *Nature reviews. Molecular cell biology* **19**, 45–58; 10.1038/nrm.2017.77 (2018).
12. Quinn, J. J. & Chang, H. Y. Unique features of long non-coding RNA biogenesis and function. *Nature reviews. Genetics* **17**, 47–62; 10.1038/nrg.2015.10 (2016).
13. Butcher, S. E. & Pyle, A. M. The molecular interactions that stabilize RNA tertiary structure: RNA motifs, patterns, and networks. *Accounts of chemical research* **44**, 1302–1311; 10.1021/ar200098t (2011).
14. Sloan, K. E. *et al.* Tuning the ribosome: The influence of rRNA modification on eukaryotic ribosome biogenesis and function. *RNA Biology* **14**, 1138–1152; 10.1080/15476286.2016.1259781 (2017).

15. Suzuki, T. The expanding world of tRNA modifications and their disease relevance. *Nature reviews. Molecular cell biology*; 10.1038/s41580-021-00342-0 (2021).
16. Zhao, B. S., Roundtree, I. A. & He, C. Post-transcriptional gene regulation by mRNA modifications. *Nature reviews. Molecular cell biology* **18**, 31–42; 10.1038/nrm.2016.132 (2017).
17. Wang, D. & Farhana, A. *StatPearls. Biochemistry, RNA Structure* (Treasure Island (FL), 2024).
18. Helm, M. & Motorin, Y. Detecting RNA modifications in the epitranscriptome: predict and validate. *Nature reviews. Genetics* **18**, 275–291; 10.1038/nrg.2016.169 (2017).
19. Schuller, A. P. & Green, R. Roadblocks and resolutions in eukaryotic translation. *Nature reviews. Molecular cell biology* **19**, 526–541; 10.1038/s41580-018-0011-4 (2018).
20. Sun, H., Li, K., Liu, C. & Yi, C. Regulation and functions of non-m6A mRNA modifications. *Nature reviews. Molecular cell biology* **24**, 714–731; 10.1038/s41580-023-00622-x (2023).
21. Gilbert, W. V. & Nachtergaele, S. mRNA Regulation by RNA Modifications. *Annual review of biochemistry* **92**, 175–198; 10.1146/annurev-biochem-052521-035949 (2023).
22. Bentley, D. L. Rules of engagement: co-transcriptional recruitment of pre-mRNA processing factors. *Current opinion in cell biology* **17**, 251–256; 10.1016/j.ceb.2005.04.006 (2005).
23. Zhou, K. I., Pecot, C. V. & Holley, C. L. 2'-O-methylation (Nm) in RNA: progress, challenges, and future directions. *RNA* **30**, 570–582; 10.1261/rna.079970.124 (2024).
24. Cappannini, A. *et al.* MODOMICS: a database of RNA modifications and related information. 2023 update. *Nucl Acids Res* **52**, D239–D244; 10.1093/nar/gkad1083 (2024).
25. Liu, J. *et al.* A METTL3-METTL14 complex mediates mammalian nuclear RNA N6-adenosine methylation. *Nat Chem Biol* **10**, 93–95; 10.1038/nchembio.1432 (2014).
26. He, P. C. & He, C. m6A RNA methylation: from mechanisms to therapeutic potential. *The EMBO journal* **40**, e105977; 10.15252/embj.2020105977 (2021).
27. Livneh, I., Moshitch-Moshkovitz, S., Amariglio, N., Rechavi, G. & Dominissini, D. The m6A epitranscriptome: transcriptome plasticity in brain development and function. *Nature reviews. Neuroscience* **21**, 36–51; 10.1038/s41583-019-0244-z (2020).
28. Lin, S., Choe, J., Du, P., Triboulet, R. & Gregory, R. I. The m(6)A Methyltransferase METTL3 Promotes Translation in Human Cancer Cells. *Molecular cell* **62**, 335–345; 10.1016/j.molcel.2016.03.021 (2016).
29. Spenkuch, F., Motorin, Y. & Helm, M. Pseudouridine: still mysterious, but never a fake (uridine)! *RNA Biology* **11**, 1540–1554; 10.4161/15476286.2014.992278 (2014).

30. Karikó, K. & Weissman, D. Naturally occurring nucleoside modifications suppress the immunostimulatory activity of RNA: implication for therapeutic RNA development. *Current opinion in drug discovery & development* **10**, 523–532 (2007).
31. Lin, S. *et al.* Mettl1/Wdr4-Mediated m7G tRNA Methylome Is Required for Normal mRNA Translation and Embryonic Stem Cell Self-Renewal and Differentiation. *Molecular cell* **71**, 244–255.e5; 10.1016/j.molcel.2018.06.001 (2018).
32. Ruiz-Arroyo, V. M. *et al.* Structures and mechanisms of tRNA methylation by METTL1-WDR4. *Nature* **613**, 383–390; 10.1038/s41586-022-05565-5 (2023).
33. Penzo, M. & Montanaro, L. Turning Uridines around: Role of rRNA Pseudouridylation in Ribosome Biogenesis and Ribosomal Function. *Biomolecules* **8**; 10.3390/biom8020038 (2018).
34. Forman, H. J. & Zhang, H. Targeting oxidative stress in disease: promise and limitations of antioxidant therapy. *Nature reviews. Drug discovery* **20**, 689–709; 10.1038/s41573-021-00233-1 (2021).
35. Juan, C. A., La Pérez de Lastra, J. M., Plou, F. J. & Pérez-Lebeña, E. The Chemistry of Reactive Oxygen Species (ROS) Revisited: Outlining Their Role in Biological Macromolecules (DNA, Lipids and Proteins) and Induced Pathologies. *International journal of molecular sciences* **22**; 10.3390/ijms22094642 (2021).
36. Finkel, T. & Holbrook, N. J. Oxidants, oxidative stress and the biology of ageing. *Nature* **408**, 239–247; 10.1038/35041687 (2000).
37. Yan, L. L. & Zaher, H. S. How do cells cope with RNA damage and its consequences? *The Journal of biological chemistry* **294**, 15158–15171; 10.1074/jbc.REV119.006513 (2019).
38. Wurtmann, E. J. & Wolin, S. L. RNA under attack: cellular handling of RNA damage. *Critical reviews in biochemistry and molecular biology* **44**, 34–49; 10.1080/10409230802594043. (2009).
39. Mailloux, R. J. Teaching the fundamentals of electron transfer reactions in mitochondria and the production and detection of reactive oxygen species. *Redox biology* **4**, 381–398; 10.1016/j.redox.2015.02.001 (2015).
40. Simms, C. L. & Zaher, H. S. Quality control of chemically damaged RNA. *Cellular and molecular life sciences : CMLS* **73**, 3639–3653; 10.1007/s00018-016-2261-7 (2016).
41. Seixas, A. F. *et al.* Bacterial Response to Oxidative Stress and RNA Oxidation. *Frontiers in genetics* **12**, 821535; 10.3389/fgene.2021.821535 (2021).
42. Tanaka, M. & Chock, P. B. Oxidative Modifications of RNA and Its Potential Roles in Biosystem. *Frontiers in molecular biosciences* **8**, 685331; 10.3389/fmolb.2021.685331 (2021).
43. Willi, J. *et al.* Oxidative stress damages rRNA inside the ribosome and differentially affects the catalytic center. *Nucleic acids research* **46**, 1945–1957; 10.1093/nar/gkx1308 (2018).
44. Kong, Q. & Lin, C.-L. G. Oxidative damage to RNA: mechanisms, consequences, and diseases. *Cellular and molecular life sciences : CMLS* **67**, 1817–1829; 10.1007/s00018-010-0277-y (2010).

45. Hahm, J. Y., Park, J., Jang, E.-S. & Chi, S. W. 8-Oxoguanine: from oxidative damage to epigenetic and epitranscriptional modification. *Experimental & molecular medicine* **54**, 1626–1642; 10.1038/s12276-022-00822-z (2022).
46. Snell, J. A., Jandova, J. & Wondrak, G. T. Hypochlorous Acid: From Innate Immune Factor and Environmental Toxicant to Chemopreventive Agent Targeting Solar UV-Induced Skin Cancer. *Frontiers in oncology* **12**, 887220; 10.3389/fonc.2022.887220 (2022).
47. Poulsen, H. E. *et al.* RNA modifications by oxidation: a novel disease mechanism? *Free radical biology & medicine* **52**, 1353–1361; 10.1016/j.freeradbiomed.2012.01.009 (2012).
48. Li, Z. *et al.* Recent Advances: Molecular Mechanism of RNA Oxidation and Its Role in Various Diseases. *Frontiers in molecular biosciences* **7**, 184; 10.3389/fmolb.2020.00184 (2020).
49. Ebrahimi, S. O., Reisi, S. & Shareef, S. miRNAs, oxidative stress, and cancer: A comprehensive and updated review. *Journal of cellular physiology* **235**, 8812–8825; 10.1002/jcp.29724 (2020).
50. Liu, Z. *et al.* Role of RNA Oxidation in Neurodegenerative Diseases. *International journal of molecular sciences* **21**; 10.3390/ijms21145022 (2020).
51. Li, Y. & Wang, X. The role of DNA and RNA guanosine oxidation in cardiovascular diseases. *Pharmacological research*, 107187; 10.1016/j.phrs.2024.107187 (2024).
52. Andrés, C. M. C., La Pérez de Lastra, J. M., Juan, C. A., Plou, F. J. & Pérez-Lebeña, E. Hypochlorous Acid Chemistry in Mammalian Cells-Influence on Infection and Role in Various Pathologies. *International journal of molecular sciences* **23**; 10.3390/ijms231810735 (2022).
53. Cadet, J., Wagner, J. R., Shafirovich, V. & Geacintov, N. E. One-electron oxidation reactions of purine and pyrimidine bases in cellular DNA. *International journal of radiation biology* **90**, 423–432; 10.3109/09553002.2013.877176 (2014).
54. Pattison, D. I., Davies, M. J. & Hawkins, C. L. Reactions and reactivity of myeloperoxidase-derived oxidants: differential biological effects of hypochlorous and hypothiocyanous acids. *Free radical research* **46**, 975–995; 10.3109/10715762.2012.667566 (2012).
55. Hawkins, C. L. & Davies, M. J. Hypochlorite-induced damage to DNA, RNA, and polynucleotides: formation of chloramines and nitrogen-centered radicals. *Chemical research in toxicology* **15**, 83–92; 10.1021/tx015548d (2002).
56. Masuda, M. *et al.* Chlorination of guanosine and other nucleosides by hypochlorous acid and myeloperoxidase of activated human neutrophils. Catalysis by nicotine and trimethylamine. *The Journal of biological chemistry* **276**, 40486–40496; 10.1074/jbc.M102700200 (2001).
57. Stanley, N. R., Pattison, D. I. & Hawkins, C. L. Ability of hypochlorous acid and N-chloramines to chlorinate DNA and its constituents. *Chemical research in toxicology* **23**, 1293–1302; 10.1021/tx100188b (2010).
58. Noyon, C. *et al.* Validation of a sensitive LC/MSMS method for chloronucleoside analysis in biological matrixes and its applications. *Talanta* **154**, 322–328; 10.1016/j.talanta.2016.03.087 (2016).

59. Noyon, C. *et al.* The presence of modified nucleosides in extracellular fluids leads to the specific incorporation of 5-chlorocytidine into RNA and modulates the transcription and translation. *Molecular and cellular biochemistry* **429**, 59–71; 10.1007/s11010-016-2936-2 (2017).
60. Tang, V., Fu, S., Rayner, B. S. & Hawkins, C. L. 8-Chloroadenosine induces apoptosis in human coronary artery endothelial cells through the activation of the unfolded protein response. *Redox biology* **26**, 101274; 10.1016/j.redox.2019.101274 (2019).
61. Suzuki, T., Friesen, M. D. & Ohshima, H. Identification of products formed by reaction of 3',5'-di-O-acetyl-2'-deoxyguanosine with hypochlorous acid or a myeloperoxidase-H₂O₂-Cl⁻ system. *Chemical research in toxicology* **16**, 382–389; 10.1021/tx025638y (2003).
62. Nilov, D. I. *et al.* Oxidation of adenosine and inosine: the chemistry of 8-oxo-7,8-dihydropurines, purine iminoquinones, and purine quinones as observed by ultrafast spectroscopy. *Journal of the American Chemical Society* **135**, 3423–3438; 10.1021/ja3068148 (2013).
63. Cadet, J., Davies, K. J. A., Medeiros, M. H., Di Mascio, P. & Wagner, J. R. Formation and repair of oxidatively generated damage in cellular DNA. *Free radical biology & medicine* **107**, 13–34; 10.1016/j.freeradbiomed.2016.12.049 (2017).
64. Whiteman, M., Jenner, A. & Halliwell, B. Hypochlorous acid-induced base modifications in isolated calf thymus DNA. *Chemical research in toxicology* **10**, 1240–1246; 10.1021/tx970086i (1997).
65. Yanagawa, H., Ogawa, Y. & Ueno, M. Redox ribonucleosides. Isolation and characterization of 5-hydroxyuridine, 8-hydroxyguanosine, and 8-hydroxyadenosine from *Torula* yeast RNA. *Journal of Biological Chemistry* **267**, 13320–13326 (1992).
66. Yan, L. L., Simms, C. L., McLoughlin, F., Vierstra, R. D. & Zaher, H. S. Oxidation and alkylation stresses activate ribosome-quality control. *Nat Commun* **10**, 5611; 10.1038/s41467-019-13579-3 (2019).
67. Macer-Wright, J. L. *et al.* A Role for Chlorinated Nucleosides in the Perturbation of Macrophage Function and Promotion of Inflammation. *Chemical research in toxicology* **32**, 1223–1234; 10.1021/acs.chemrestox.9b00044 (2019).
68. Nguyen, K. *et al.* The Potential Use of Hypochlorous Acid and a Smart Prefabricated Sanitising Chamber to Reduce Occupation-Related COVID-19 Exposure. *Risk management and healthcare policy* **14**, 247–252; 10.2147/RMHP.S284897 (2021).
69. Thapa, B. & Schlegel, H. B. Calculations of pK_a's and redox potentials of nucleobases with explicit waters and polarizable continuum solvation. *The journal of physical chemistry. A* **119**, 5134–5144; 10.1021/jp5088866 (2015).
70. Suzuki, T., Masuda, M., Friesen, M. D. & Ohshima, H. Formation of spiroiminodihydroantoin nucleoside by reaction of 8-oxo-7,8-dihydro-2'-deoxyguanosine with hypochlorous acid or a myeloperoxidase-H₂O₂-Cl⁻ system. *Chemical research in toxicology* **14**, 1163–1169; 10.1021/tx010024z (2001).

71. Luo, W., Muller, J. G., Rachlin, E. M. & Burrows, C. J. Characterization of spiroiminodihydantoin as a product of one-electron oxidation of 8-Oxo-7,8-dihydroguanosine. *Organic letters* **2**, 613–616; 10.1021/ol9913643 (2000).
72. Fleming, A. M. & Burrows, C. J. Chemistry of ROS-mediated oxidation to the guanine base in DNA and its biological consequences. *International journal of radiation biology* **98**, 452–460; 10.1080/09553002.2021.2003464 (2022).
73. Yanagawa, H., Ogawa, Y., Ueno, M., Sasaki, K. & Sato, T. A novel minimum ribozyme with oxidoreduction activity. *Biochemistry* **29**, 10585–10589; 10.1021/bi00499a002 (1990).
74. Luo, Y., Henle, E. S. & Linn, S. Oxidative damage to DNA constituents by iron-mediated fenton reactions. The deoxycytidine family. *Journal of Biological Chemistry* **271**, 21167–21176 (1996).
75. Dizdaroglu, M. & Jaruga, P. Mechanisms of free radical-induced damage to DNA. *Free radical research* **46**, 382–419; 10.3109/10715762.2011.653969 (2012).
76. Wagner, J. R. & Cadet, J. Oxidation reactions of cytosine DNA components by hydroxyl radical and one-electron oxidants in aerated aqueous solutions. *Accounts of chemical research* **43**, 564–571; 10.1021/ar9002637 (2010).
77. Barciszewski, J., Barciszewska, M. Z., Siboska, G., Rattan, S. I. & Clark, B. F. Some unusual nucleic acid bases are products of hydroxyl radical oxidation of DNA and RNA. *Molecular biology reports* **26**, 231–238; 10.1023/a:1007058602594 (1999).
78. Kreutzer, D. A. & Essigmann, J. M. Oxidized, deaminated cytosines are a source of C → T transitions in vivo. *Proceedings of the National Academy of Sciences of the United States of America* **95**, 3578–3582; 10.1073/pnas.95.7.3578 (1998).
79. Prashar, T., La Selle, F. de & Hudak, K. A. Abasic RNA: its formation and potential role in cellular stress response. *RNA Biology* **20**, 348–358; 10.1080/15476286.2023.2223466 (2023).
80. Tanaka, M. *et al.* RNA oxidation catalyzed by cytochrome c leads to its depurination and cross-linking, which may facilitate cytochrome c release from mitochondria. *Free radical biology & medicine* **53**, 854–862; 10.1016/j.freeradbiomed.2012.05.044 (2012).
81. Smith, W. E. *et al.* Shiga toxin 1 triggers a ribotoxic stress response leading to p38 and JNK activation and induction of apoptosis in intestinal epithelial cells. *Infection and immunity* **71**, 1497–1504; 10.1128/iai.71.3.1497-1504.2003 (2003).
82. Vind, A. C., Genzor, A. V. & Bekker-Jensen, S. Ribosomal stress-surveillance: three pathways is a magic number. *Nucl Acids Res* **48**, 10648–10661; 10.1093/nar/gkaa757 (2020).
83. Watts, J. A. *et al.* A common transcriptional mechanism involving R-loop and RNA abasic site regulates an enhancer RNA of APOE. *Nucl Acids Res* **50**, 12497–12514; 10.1093/nar/gkac1107 (2022).
84. Tanaka, M., Han, S., K pfer, P. A., Leumann, C. J. & Sonntag, W. E. Quantification of oxidized levels of specific RNA species using an aldehyde reactive probe. *Analytical Biochemistry* **417**, 142–148; 10.1016/j.ab.2011.05.038 (2011).

85. Tanaka, M. *et al.* An assay for RNA oxidation induced abasic sites using the Aldehyde Reactive Probe. *Free radical research* **45**, 237–247; 10.3109/10715762.2010.535529 (2011).
86. Peattie, D. A. Direct chemical method for sequencing RNA. *Proceedings of the National Academy of Sciences of the United States of America* **76**, 1760–1764; 10.1073/pnas.76.4.1760 (1979).
87. Peattie, D. A. & Gilbert, W. Chemical probes for higher-order structure in RNA. *Proceedings of the National Academy of Sciences of the United States of America* **77**, 4679–4682; 10.1073/pnas.77.8.4679 (1980).
88. Maxam, A. M. & Gilbert, W. A new method for sequencing DNA. *Proceedings of the National Academy of Sciences of the United States of America* **74**, 560–564; 10.1073/pnas.74.2.560 (1977).
89. Liu, Y. *et al.* RNA abasic sites in yeast and human cells. *Proceedings of the National Academy of Sciences of the United States of America* **117**, 20689–20695; 10.1073/pnas.2011511117 (2020).
90. Poetsch, A. R., Boulton, S. J. & Luscombe, N. M. Genomic landscape of oxidative DNA damage and repair reveals regioselective protection from mutagenesis. *Genome biology* **19**, 215; 10.1186/s13059-018-1582-2 (2018).
91. Liu, Z. J., Martínez Cuesta, S., van Delft, P. & Balasubramanian, S. Sequencing abasic sites in DNA at single-nucleotide resolution. *Nature chemistry* **11**, 629–637; 10.1038/s41557-019-0279-9 (2019).
92. Cai, Y., Cao, H., Wang, F., Zhang, Y. & Kapranov, P. Complex genomic patterns of abasic sites in mammalian DNA revealed by a high-resolution SSiNGLe-AP method. *Nat Commun* **13**, 5868; 10.1038/s41467-022-33594-1 (2022).
93. Cao, B. *et al.* Nick-seq for single-nucleotide resolution genomic maps of DNA modifications and damage. *Nucl Acids Res* **48**, 6715–6725; 10.1093/nar/gkaa473 (2020).
94. Liu, C. *et al.* Dual chemical labeling enables nucleotide-resolution mapping of DNA abasic sites and common alkylation damage in human mitochondrial DNA. *Nucl Acids Res* **51**, e73; 10.1093/nar/gkad502 (2023).
95. Yoluç, Y. *et al.* Instrumental analysis of RNA modifications. *Critical reviews in biochemistry and molecular biology*, 1–27; 10.1080/10409238.2021.1887807 (2021).
96. Kellner, S., Burhenne, J. & Helm, M. Detection of RNA modifications. *RNA Biology* **7**, 237–247; 10.4161/rna.7.2.11468 (2010).
97. Schwartz, S. & Motorin, Y. Next-generation sequencing technologies for detection of modified nucleotides in RNAs. *RNA Biology* **14**, 1124–1137; 10.1080/15476286.2016.1251543 (2017).
98. Cavaluzzi, M. J. & Borer, P. N. Revised UV extinction coefficients for nucleoside-5'-monophosphates and unpaired DNA and RNA. *Nucl Acids Res* **32**, e13; 10.1093/nar/gnh015 (2004).
99. Prütz, W. A. Hypochlorous acid interactions with thiols, nucleotides, DNA, and other biological substrates. *Archives of biochemistry and biophysics* **332**, 110–120; 10.1006/abbi.1996.0322 (1996).

100. Prütz, W. A. Interactions of hypochlorous acid with pyrimidine nucleotides, and secondary reactions of chlorinated pyrimidines with GSH, NADH, and other substrates. *Archives of biochemistry and biophysics* **349**, 183–191; 10.1006/abbi.1997.0440 (1998).
101. Summer, H., Grämer, R. & Dröge, P. Denaturing Urea Polyacrylamide Gel Electrophoresis (Urea PAGE). *JoVE*; 10.3791/1485 (2009).
102. Crisafuli, F. A. P., Ramos, E. B. & Rocha, M. S. Characterizing the interaction between DNA and GelRed fluorescent stain. *European biophysics journal : EBJ* **44**, 1–7; 10.1007/s00249-014-0995-4 (2015).
103. Thüring, K., Schmid, K., Keller, P. & Helm, M. Analysis of RNA modifications by liquid chromatography-tandem mass spectrometry. *Methods (San Diego, Calif.)* **107**, 48–56; 10.1016/j.ymeth.2016.03.019 (2016).
104. Kellner, S. *et al.* Absolute and relative quantification of RNA modifications via biosynthetic isotopomers. *Nucl Acids Res* **42**, e142; 10.1093/nar/gku733 (2014).
105. Crain, P. F. Preparation and enzymatic hydrolysis of DNA and RNA for mass spectrometry. *Methods in enzymology* **193**, 782–790; 10.1016/0076-6879(90)93450-y (1990).
106. Konermann, L. Addressing a Common Misconception: Ammonium Acetate as Neutral pH "Buffer" for Native Electrospray Mass Spectrometry. *The official journal of The American Society for Mass Spectrometry* **28**, 1827–1835; 10.1007/s13361-017-1739-3 (2017).
107. Pomerantz, S. C. & McCloskey, J. A. Analysis of RNA hydrolyzates by liquid chromatography-mass spectrometry. *Methods in enzymology* **193**, 796–824; 10.1016/0076-6879(90)93452-Q (1990).
108. Jora, M., Lobue, P. A., Ross, R. L., Williams, B. & Addepalli, B. Detection of ribonucleoside modifications by liquid chromatography coupled with mass spectrometry. *Biochimica et biophysica acta. Gene regulatory mechanisms* **1862**, 280–290; 10.1016/j.bbagr.2018.10.012 (2019).
109. Sleno, L. & Volmer, D. A. Ion activation methods for tandem mass spectrometry. *Journal of mass spectrometry : JMS* **39**, 1091–1112; 10.1002/jms.703 (2004).
110. Hoffmann, E. de. Tandem mass spectrometry: A primer. *Journal of mass spectrometry : JMS* **31**, 129–137; 10.1002/(SICI)1096-9888(199602)31:2<129::AID-JMS305>3.0.CO;2-T (1996).
111. Kellner, S. *et al.* Profiling of RNA modifications by multiplexed stable isotope labelling. *Chem. Commun.* **50**, 3516–3518; 10.1039/c3cc49114e (2014).
112. Ammann, G., Berg, M., Dalwigk, J. F. & Kaiser, S. M. Pitfalls in RNA Modification Quantification Using Nucleoside Mass Spectrometry. *Accounts of chemical research* **56**, 3121–3131; 10.1021/acs.accounts.3c00402 (2023).
113. Sanger, F., Nicklen, S. & Coulson, A. R. DNA sequencing with chain-terminating inhibitors. *Proceedings of the National Academy of Sciences of the United States of America* **74**, 5463–5467; 10.1073/pnas.74.12.5463 (1977).
114. Rodriguez, R. & Krishnan, Y. The chemistry of next-generation sequencing. *Nat Biotechnol* **41**, 1709–1715; 10.1038/s41587-023-01986-3 (2023).

115. Zhang, Y., Lu, L. & Li, X. Detection technologies for RNA modifications. *Experimental & molecular medicine* **54**, 1601–1616; 10.1038/s12276-022-00821-0 (2022).
116. Motorin, Y. & Helm, M. Methods for RNA Modification Mapping Using Deep Sequencing: Established and New Emerging Technologies. *Genes* **10**; 10.3390/genes10010035 (2019).
117. Motorin, Y. & Marchand, V. Analysis of RNA Modifications by Second- and Third-Generation Deep Sequencing: 2020 Update. *Genes* **12**; 10.3390/genes12020278 (2021).
118. Sas-Chen, A. & Schwartz, S. Misincorporation signatures for detecting modifications in mRNA: Not as simple as it sounds. *Methods (San Diego, Calif.)* **156**, 53–59; 10.1016/j.ymeth.2018.10.011 (2019).
119. Zhao, L.-Y., Song, J., Liu, Y., Song, C.-X. & Yi, C. Mapping the epigenetic modifications of DNA and RNA. *Protein & cell* **11**, 792–808; 10.1007/s13238-020-00733-7 (2020).
120. Marchand, V. *et al.* AlkAniline-Seq: Profiling of m7 G and m3 C RNA Modifications at Single Nucleotide Resolution. *Angewandte Chemie (International ed. in English)* **57**, 16785–16790; 10.1002/anie.201810946 (2018).
121. Helm, M., Schmidt-Dengler, M. C., Weber, M. & Motorin, Y. General Principles for the Detection of Modified Nucleotides in RNA by Specific Reagents. *Advanced biology* **5**, e2100866; 10.1002/adbi.202100866 (2021).
122. Wintermeyer, W. & Zachau, H. G. A specific chemical chain scission of tRNA at 7-methylguanosine. *FEBS letters* **11**, 160–164; 10.1016/0014-5793(70)80518-x (1970).
123. Wintermeyer, W. & Zachau, H. G. Tertiary structure interactions of 7-methylguanosine in yeast tRNA Phe as studied by borohydride reduction. *FEBS letters* **58**, 306–309; 10.1016/0014-5793(75)80285-7 (1975).
124. Chetsanga, C. J. & Makaroff, C. Alkaline opening of imidazole ring of 7-methylguanosine. 2. Further studies on reaction mechanisms and products. *Chemico-biological interactions* **41**, 235–249; 10.1016/0009-2797(82)90092-8 (1982).
125. Chetsanga, C. J., Bearie, B. & Makaroff, C. Alkaline opening of imidazole ring of 7-methylguanosine. 1. Analysis of the resulting pyrimidine derivatives. *Chemico-biological interactions* **41**, 217–233; 10.1016/0009-2797(82)90091-6 (1982).
126. Palin, A. T. The Determination of Free and Combined Chlorine in Water by the Use of Diethyl-p-phenylene Diamine. *Journal - American Water Works Association* **49**, 873–880; 10.1002/j.1551-8833.1957.tb16870.x (1957).
127. Tantry, I. Q. *et al.* Hypochlorous acid induced structural and conformational modifications in human DNA: A multi-spectroscopic study. *International Journal of Biological Macromolecules* **106**, 551–558; 10.1016/j.ijbiomac.2017.08.051 (2018).
128. Świerczyńska, M., Słowiński, D., Michalski, R., Romański, J. & Podsiadły, R. A New and Fast-Response Fluorescent Probe for Monitoring Hypochlorous Acid Derived

- from Myeloperoxidase. *Molecules (Basel, Switzerland)* **28**; 10.3390/molecules28166055 (2023).
129. Jia, Z. *et al.* An Oxidative Cleavage-Based Cruciform DNA Nanostructure for In Vivo Hypochlorous Acid Visualization to Monitor Intestinal Inflammation. *Analytical chemistry*; 10.1021/acs.analchem.4c01272 (2024).
130. Budavari, S. *The Merck index. An encyclopedia of chemicals, drugs, and biologicals.* 11th ed. (Merck, Rahway, N.J., U.S.A., 1991, 1989).
131. Gould, J. P., Richards, J. T. & Miles, M. G. The kinetics and primary products of uracil chlorination. *Water Research* **18**, 205–212; 10.1016/0043-1354(84)90070-8 (1984).
132. Gould, J. The formation of stable organic chloramines during the aqueous chlorination of cytosine and 5-methylcytosine. *Water Research* **18**, 991–999; 10.1016/0043-1354(84)90250-1 (1984).
133. Rozelle, A. L., Cheun, Y., Vilas, C. K., Koag, M.-C. & Lee, S. DNA interstrand cross-links induced by the major oxidative adenine lesion 7,8-dihydro-8-oxoadenine. *Nat Commun* **12**, 1897; 10.1038/s41467-021-22273-2 (2021).
134. Choi, Y. J., Chang, S. J., Gibala, K. S. & Resendiz, M. J. E. 8-Oxo-7,8-dihydroadenine and 8-Oxo-7,8-dihydroadenosine-Chemistry, Structure, and Function in RNA and Their Presence in Natural Products and Potential Drug Derivatives. *Chemistry (Weinheim an der Bergstrasse, Germany)* **23**, 6706–6716; 10.1002/chem.201605163 (2017).
135. Greenberg, M. M. The formamidopyrimidines: purine lesions formed in competition with 8-oxopurines from oxidative stress. *Accounts of chemical research* **45**, 588–597; 10.1021/ar2002182 (2012).
136. Wang, X.-W., Liu, C.-X., Chen, L.-L. & Zhang, Q. C. RNA structure probing uncovers RNA structure-dependent biological functions. *Nat Chem Biol* **17**, 755–766; 10.1038/s41589-021-00805-7 (2021).
137. Ramanathan, M., Porter, D. F. & Khavari, P. A. Methods to study RNA-protein interactions. *Nat Methods* **16**, 225–234; 10.1038/s41592-019-0330-1 (2019).
138. Vidal, B. d. C. & Mello, M. L. S. Toluidine blue staining for cell and tissue biology applications. *Acta histochemica* **121**, 101–112; 10.1016/j.acthis.2018.11.005 (2019).
139. Olmsted, J. & Kearns, D. R. Mechanism of ethidium bromide fluorescence enhancement on binding to nucleic acids. *Biochemistry* **16**, 3647–3654; 10.1021/bi00635a022 (1977).
140. Berg, J. M., Tymoczko, J. L., Stryer, L. & Gatto, G. J. *Stryer Biochemie.* 7th ed. (Springer, Berlin, 2012).
141. Fedeles, B. I. *et al.* Intrinsic mutagenic properties of 5-chlorocytosine: A mechanistic connection between chronic inflammation and cancer. *Proceedings of the National Academy of Sciences of the United States of America* **112**, E4571–80; 10.1073/pnas.1507709112 (2015).
142. Kou, Y., Koag, M.-C. & Lee, S. Promutagenicity of 8-Chloroguanine, A Major Inflammation-Induced Halogenated DNA Lesion. *Molecules (Basel, Switzerland)* **24**; 10.3390/molecules24193507. (2019).

143. K pfer, P. A. & Leumann, C. J. The chemical stability of abasic RNA compared to abasic DNA. *Nucl Acids Res* **35**, 58–68; 10.1093/nar/gkl948 (2007).
144. Motorin, Y. & Helm, M. General Principles and Limitations for Detection of RNA Modifications by Sequencing. *Accounts of chemical research* **57**, 275–288; 10.1021/acs.accounts.3c00529 (2024).
145. Fedor, M. J. The role of metal ions in RNA catalysis. *Current Opinion in Structural Biology* **12**, 289–295; 10.1016/S0959-440X(02)00324-X (2002).
146. Fleming, A. M., Alshykhly, O., Zhu, J., Muller, J. G. & Burrows, C. J. Rates of chemical cleavage of DNA and RNA oligomers containing guanine oxidation products. *Chemical research in toxicology* **28**, 1292–1300; 10.1021/acs.chemrestox.5b00096 (2015).
147. Laverty, D. J., Averill, A. M., Doubl e, S. & Greenberg, M. M. The A-Rule and Deletion Formation During Abasic and Oxidized Abasic Site Bypass by DNA Polymerase θ . *ACS chemical biology* **12**, 1584–1592; 10.1021/acschembio.7b00211 (2017).
148. Glennon, M. M., Skinner, A., Krutsinger, M. & Resendiz, M. J. E. Translesion synthesis by AMV, HIV, and MMLV reverse transcriptases using RNA templates containing inosine, guanosine, and their 8-oxo-7,8-dihydropurine derivatives. *PLOS ONE* **15**, e0235102; 10.1371/journal.pone.0235102 (2020).
149. Alenko, A., Fleming, A. M. & Burrows, C. J. Reverse Transcription Past Products of Guanine Oxidation in RNA Leads to Insertion of A and C opposite 8-Oxo-7,8-dihydroguanine and A and G opposite 5-Guanidinohydantoin and Spiroiminodihydantoin Diastereomers. *Biochemistry* **56**, 5053–5064; 10.1021/acs.biochem.7b00730 (2017).
150. Furge, L. L. & Guengerich, F. P. Analysis of nucleotide insertion and extension at 8-oxo-7,8-dihydroguanine by replicative T7 polymerase exo- and human immunodeficiency virus-1 reverse transcriptase using steady-state and pre-steady-state kinetics. *Biochemistry* **36**, 6475–6487; 10.1021/bi9627267 (1997).
151. Zhan, Y. *et al.* Localized control of oxidized RNA. *Journal of cell science* **128**, 4210–4219; 10.1242/jcs.175232 (2015).
152. Simms, C. L., Hudson, B. H., Mosior, J. W., Rangwala, A. S. & Zaher, H. S. An active role for the ribosome in determining the fate of oxidized mRNA. *Cell reports* **9**, 1256–1264; 10.1016/j.celrep.2014.10.042 (2014).
153. Seok, H. *et al.* Position-specific oxidation of miR-1 encodes cardiac hypertrophy. *Nature* **584**, 279–285; 10.1038/s41586-020-2586-0 (2020).
154. Li, Z., Wu, J. & Deleo, C. J. RNA damage and surveillance under oxidative stress. *IUBMB life* **58**, 581–588; 10.1080/15216540600946456 (2006).
155. Heiss, M., Reichle, V. F. & Kellner, S. Observing the fate of tRNA and its modifications by nucleic acid isotope labeling mass spectrometry: NAIL-MS. *RNA Biology* **14**, 1260–1268; 10.1080/15476286.2017.1325063 (2017).
156. Wickham, H. & Sievert, C. *Ggplot2. Elegant graphics for data analysis*. 2nd ed. (Springer, Dordrecht, New York, op. 2016).
157. Langmead, B. & Salzberg, S. L. Fast gapped-read alignment with Bowtie 2. *Nat Methods* **9**, 357–359; 10.1038/nmeth.1923 (2012).

158. Luo, W., Muller, J. G., Rachlin, E. M. & Burrows, C. J. Characterization of hydantoin products from one-electron oxidation of 8-oxo-7,8-dihydroguanosine in a nucleoside model. *Chemical research in toxicology* **14**, 927-938; 10.1021/tx010072j (2001).

CURRICULUM VITAE

[REDACTED]

[REDACTED]

[REDACTED]

[REDACTED]

[REDACTED]

[REDACTED]

[REDACTED]

[REDACTED]

[REDACTED]

[REDACTED]

[REDACTED]

[REDACTED]

[REDACTED]

[REDACTED]

[REDACTED]

[REDACTED]

[REDACTED]

[REDACTED]

[REDACTED]

[REDACTED]

[REDACTED]

[REDACTED]

[REDACTED]

[REDACTED]

[REDACTED]

[REDACTED]

[REDACTED]

[REDACTED]

[REDACTED]

[REDACTED]

[REDACTED]

[REDACTED]

[REDACTED]